TECHNISCHE UNIVERSITÄT MÜNCHEN

Lehrstuhl E23 für Technische Physik

Walther-Meißner-Institut für Tieftemperaturforschung
der Bayerischen Akademie der Wissenschaften

Single Excitation Transfer in the Quantum Regime:
A Spin-Based Solid-State Approach

Christoph Wilhelm Zollitsch

Vollständiger Abdruck der von der Fakultät für Physik der Technischen
Universität München zur Erlangung des akademischen Grades eines

Doktors der Naturwissenschaften

genehmigten Dissertation.

DON'T PANIC
Douglas Adams, The Hitchhiker's Guide to the Galaxy

Abstract

In the field of quantum information spin ensembles are promising candidates for quantum information storage and processing. This requires an efficient interface between the spin ensemble and a suitable quantum circuit, providing a control interface and a bus system for quantum information. In solid-state based quantum information processing this can be realized e.g. by coupling natural paramagnetic spins contained in a host material to a superconducting microwave resonator. The resulting hybrid system harnesses the advantages of both constituents, combining fast processing elements and long term memory elements. To allow for a coherent and loss-free exchange of information between the two constituents, strong coupling is a mandatory requirement. For a hybrid system operating in the strong coupling regime, the rate information exchange is much larger than the individual loss rates of the subsystems. Promising candidates for possible quantum information applications are phosphorus donors in isotopically purified ^{28}Si, due to their exceptionally long electron and nuclear coherence times. Utilizing these remarkable properties in the field of quantum information, would impose a major step towards the realization of all silicon quantum computation.

This thesis focus is on the investigation of the interaction between a superconducting microwave resonator and an ensemble of phosphorus donors in a ^{28}Si host crystal. The interaction is studied for two different designs of microwave resonators, a coplanar waveguide resonator and a lumped element resonator, differing in geometrical size and the number of harmonic modes. At millikelvin temperatures, the hybrid system comprising the coplanar waveguide resonator is found to operated in a regime of high cooperativity, while using the lumped element resonator strong coupling could be achieved. This is the first demonstration of strong coupling between a phosphorus donor spin ensemble in silicon and a superconducting microwave resonator.

The hybrid system is studied under the influence of pulsed microwave excitation in the time domain. An additional third hybrid mode is discovered, when the hybrid system is driven in a steady state by a single high power, long microwave pulse. Also, the free induction decay of the third hybrid mode is found to be greatly enhanced, compared to the decay time of an uncoupled spin ensemble. The relaxation and coherence times of the coupled system are extracted by pulsed microwave spectroscopy techniques, like Hahn-echo and inversion recovery sequences. An exceptional enhancement in coherence time of more than two orders of magnitude is found for the lowest temperature with respect to the uncoupled spin system.

Zusammenfassung

Auf dem Gebiet der Quanteninformation repräsentieren Ensembles von Spins vielversprechende Kandidaten für die Quanteninformationsspeicherung und -verarbeitung. Dies erfordert eine effiziente Schnittstelle zwischen dem Spinensemble und einer geeigneten Quantenschaltung, welche als Kontrolle und als Bussystem für die Quanteninformationen dienen soll. In der festkörperbasierten Quanteninformationsverarbeitung kann dies beispielsweise durch die Kopplung paramagnetischer Spins, in einem Festkörper, an einen supraleitenden Mikrowellenresonator realisiert werden. Das sich ergebende Hybridsystem nutzt die Vorteile beider Komponenten und vereint schnelle Prozessierung mit langlebigen Speicherelementen. Um für einen kohärenten und verlustfreien Informationsaustausch zwischen den beiden Subsystemen zu garantieren, ist eine starke Kopplung zwingend Erforderlich. Ein Hybridsystem, das in dem Regime der starken Kopplung betrieben wird, tauscht mit einer Rate Information aus, die um ein vielfaches schneller ist als die Verlustraten der beiden Komponenten. Dabei sind Phosphordonatoren in isotopenreinen ^{28}Si besonders vielversprechende Kandidaten für mögliche Anwendungen im Gebiet der Quanteninformation, aufgrund der außergewöhnlich langen Kohärenzzeiten des Elektronspins und des Kernspins. Wenn diese bemerkenswerten Eigenschaften für das Gebiet der Quanteninformation nutzbar gemacht werden können, würde dies einem großen Schritt in Richtung der Realisierung eines siliziumbasierten Quantencomputers entsprechen.

Diese Arbeit konzentriert sich auf die Untersuchung der Wechselwirkung zwischen einem supraleitenden Mikrowellenresonator und einem Spinensemble bestehend aus Phosphordonatoren in einem ^{28}Si Kristall. Dabei wird die Interaktion für zwei verschiedene Ausführungen von Mikrowellenresonatoren studiert, einem koplanaren Wellenleiterresonator und einem koplanaren LC-Schwingkreis untersucht, welche sich in der geometrischen Größe und der Anzahl von harmonischen Moden unterscheiden. Bei millikelvin Temperaturen wird das Hybridsystem, welches den koplanaren Wellenleiterresonator umfasst, in einem Regime hoher Kooperativität gefunden, während für das Hybridsystem, welches auf den koplanaren LC-Schwingkreis basiert, starke Kopplung realisiert wurde. Dies repräsentiert die erste Demonstration von starker Kopplung zwischen einem Spinensemble aus Phosphordonatoren in Silizium und einem supraleitenden Mikrowellenresonator.

Des weiteren wird das Hybridsystem mittels Mikrowellenpulsen in der Zeitdomäne untersucht. Wenn das Hybridsystem mit einem intensiven, langen Mikrowellenimpuls in einen Gleichgewichtszustand getrieben wird, kann eine zusätzliche dritte Hybridmode beobachtet werden. Verglichen mit dem freien Induktionszerfalls eines ungekoppelten Spinensembles, weißt diese dritte Hybridmode auch eine stark verlängerte Zerfallszeit auf. Zusätzlich werden die Relaxationszeiten und Kohärenzzeiten des gekoppelten Systems mittels gepulsten Mikrowellenspektroskopietechniken extrahiert, wie der Hahn-Echo- und der Inversionserholungssequenz. Bei tiefsten Temperaturen, wird eine außergewöhnliche Verlängerung der Kohärenzzeit von mehr als zwei Größenordnungen festgestellt, bezogen auf die Kohärenzzeit eines ungekoppelten Spinsystems.

Realisierung von starker Kopplung zwischen einem supraleitenden Mikrowellenresonator und einem Spinensemble von Phosphordonatoren in isotopenreinen Silizium-28. Die

dynamischen Eigenschaften des Hybridsystems wurden bei mK Temperaturen und extrem niedrigen Mikrowellenleistungen untersucht. Mittels gepulster Mikrowellenspektroskopie wurde eine deutliche Verlängerung der Kohärenzzeit des Hybridsystems im Vergleich zu der eines ungekoppelten Spinsystems festgestellt.

Contents

Chapter 1

Introduction

"And to this end they built themselves a stupendous super-computer which was so amazingly intelligent that even before its data banks had been connected up it had started from I think therefore I am and got as far as deducing the existence of rice pudding and income tax before anyone managed to turn it off." [1] A computer capable of giving "the Answer to the Great Question of Life, the Universe and Everything" [1] must have an exceptional computational performance. It is unclear, weather a classical computer could ever be able to perform such a task. On the other hand, a computer utilizing the laws of quantum mechanics for computation, could be able to give an answer to this question. Nowadays, much effort is put into the realization of an actual working quantum computer [2]. This comprises the field of quantum information processing, in which classical bits are replaced by quantum bits, comprised of two level system. Due to the quantum mechanical nature, not only the two corresponding energy levels of the system are accessible, but also their superposition states. This increases the amount of information possibly processed by a single quantum bit, in reference to a classical bit. For specific problems, quantum computers are in principal able to compute much larger amounts of data, than classical computers on a same time scale. However, for the computation of "the Answer to the Great Question of Life, the Universe and Everything" [1], long term quantum information storage would be required.

In solid-state based quantum information processing, fast quantum processing elements are complemented by quantum memories [3]. Typically these two elements come with opposing requirements. Long storage times depend on systems well isolated from their environment [4,5], while fast operating elements rely heavily on strong interactions amongst themselves and to control circuits [2,6]. One approach to reconcile these contradictory requirements is to combine both memory and operating elements in a hybrid circuit, harnessing the advantages of both constituents. To maintain the quantum mechanical nature of the processed information, it is imperative to establish a strong coupling between these elements. For a strongly coupled system the rate on which information is exchanged between the two systems, is much larger than their individual loss rates, assuring a coherent and loss-free information transfer. On this basis, quantum networks of fast processing units and long storage elements could be realized by strongly coupling them to a common quantum bus system [7,8].

Promising candidates for storage elements are spin ensembles due to their long coher-

1

ence times [4, 5, 9–11], while for quantum processing elements superconducting quantum circuits are well established [2, 3, 6, 7, 12, 13]. The volatile nature of quantum information, demands an environment, where disturbing sources of noise are inhibited. Typically, this is resolved by operating these elements at millikelvin temperatures and GHz frequencies, a regime in which both elements can be combined naturally. A multitude of experiments demonstrated the preparation of quantum states using superconducting circuits [2, 6, 7, 12, 13]. Complementary, the implementation of (classical) information storage and retrieval protocols were realized for natural spin systems such as nitrogen vacancy (NV) centers in diamond [8, 14, 15] and phosphorus donors in silicon [16]. Additionally, strong coupling between microwave resonators and spin ensembles was demonstrated for NV centers [17–20] and P1 centers [21] in diamond, Cr impurities in sapphire [22], DPPH [23] and erbium centers in Y_2SiO_5 [24] as well as for exchange-coupled magnetic systems [25–29].

During the course of this thesis, high cooperativity between phosphorus donors in silicon and a superconducting microwave resonator has been demonstrated [3]. Phosphorus dopants in isotopically purified ^{28}Si are a benchmark system due to their exceptionally long electron and nuclear coherence times exceeding $0.5\,s$ and $39\,min$, respectively [4, 5, 11]. Harnessing these remarkable qualities for possible quantum information applications, could constitute to a major "quantum" leap in this field of research. Furthermore, to block external unwanted interactions with thermal photons, the constituents of a quantum circuit are required to be operated at millikelvin temperatures, a temperature regime rather unexplored for phosphorus donors in silicon [11, 30]. Especially, the limiting decoherence mechanisms in this regime are still unknown and of present interest [4, 5, 11]. As a long coherence time is essential for a quantum memory, an identification of the limiting mechanisms allows to effectively circumvent these processes, prolonging the storage capabilities. When considering the phosphorus donors as part of a strongly coupled hybrid system, little is known about the effect on the characteristic time constants of the spin system. So far, the investigations focused on spin ensembles weakly coupled to microwave resonators, concerning the implementation of read and write protocols [8, 14, 15] as well as the enhanced spontaneous emission of a spin ensemble into a resonator [31–34]. For the strong coupling regime, the so-called cavity protection effect is proposed [35, 36], which protects an spin ensemble from decoherence, and was recently demonstrated experimentally [20]. Furthermore, a preparation of long living collective dark states in a strongly coupled system, due to spectral hole burning or by a magnon gradient memory, the coherence of the collective states could even more prolonged [37–39]. The latter experiments demonstrated that strong coupling can have a significant influence on the decoherence mechanisms of the individual systems, when prepared accordingly. However, a systematic study of the coherence time T_2 or the energy relaxation time T_1 of a spin ensemble, strongly coupled to a microwave resonator still is missing.

Concerning this matter, two pioneering accomplishments are achieved during the course of this thesis. Firstly, by demonstrating strong coupling between an ensemble of phosphorus donor spins and a superconducting microwave resonator for the first time, and secondly, by studying the hybrid system's coherence time and relaxation time in the strong coupling regime as well as in the weak coupling regime.

The thesis begins with a presentation of the individual elements, comprising the hybrid system under investigation in chapter 2. The utilized designs of superconducting coplanar microwave resonators are presented and their characteristics are discussed. Next, the spin

ensemble of choice is introduced, consisting of phosphorus donors in isotopically purified ^{28}Si. The chapter closes by introducing the experimental setup, comprising the combined cryogen free pulse tube cooler - dilution refrigerator cryostat, the microwave delivery and detection equipment and the sample mounting.

Chapter 3 comprises the continuous wave spectroscopy on the coupled system. Beginning with a characterization of the microwave damping of the measurement setup's microwave circuit. In addition, the dependence of the microwave resonator's resonance frequency on the applied static magnetic field is studied and modeled. To introduce the concepts in coupled system dynamics, the underlying theoretical framework is briefly outlined. Next, the spectroscopic investigations on the interaction between a superconducting coplanar waveguide resonator with an ensemble of phosphorus donors in a ^{28}Si crystal are presented. The microwave transmission is analyzed, finding the coupled system in a regime of high cooperativity, where the determined collective coupling is in the same order of magnitude as the loss rate of the spin ensemble. The experimental result on the collective coupling is compared with a numerical calculation of the coupling strength. The loss rate of the spin ensemble is found to be significantly larger than expected for phosphorus donors in isotopically purified ^{28}Si, and the possible source of this difference is discussed. Lastly, the collective coupling is investigated for temperatures ranging from 50 mK to 3.5 K. The found dependence on temperature is described by a statistical function, comprising the thermal spin polarization of the phosphorus donor spin ensemble. Finally, the interaction between a superconducting coplanar lumped element resonator with an ensemble of phosphorus donors in a ^{28}Si crystal is studied. The spectroscopic characterization shows, that the hybrid system operates in the strong coupling regime, demonstrating for the first time strong coupling for phosphorus donors in silicon. The microwave transmission exhibited an asymmetric linewidth in the normal mode splitting of the microwave resonator, which is completely unexpected from the Tavis-Cummings model. The asymmetric linewidth is modeled by assuming a complex microwave drive in addition to an incoherent coupling process, via an incoherent bath of frequency modes.

Chapter 4 presents the results obtained from pulsed microwave spectroscopy on the hybrid system. First, the hybrid system is studied when stimulated by a high power, single long microwave pulse, which drives the system into a steady state. The response of the hybrid system during and after this pulse application is analyzed. Thereby, an additional third hybrid mode is found, which has, up to now, never been observed experimentally. The free induction decay of the hybrid system, following the microwave pulse, showed a remarkable enhancement of the decay time, in respect to the decay time of an uncoupled spin ensemble. The hybrid system is assumed to couple to subradiant energy states, which are protected against decoherence, prolonging the free induction decay. Next, the coherence time T_2 of the hybrid system is investigated, using Hahn echo spectroscopy. The coherence time is determined for temperatures ranging from 50 mK up to 4 K and compared to the results obtained from conventional pulsed electron spin resonance for temperatures from 6 K to 15 K. For the hybrid system, an exceptional enhancement in coherence time of more than two orders of magnitude is found for the lowest temperature, compared to the time extracted at 6 K. In the final part of this chapter the relaxation time T_1 of the hybrid system is studied. By means of inversion recovery spectroscopy, the relaxation time is determined for temperatures between 50 mK and 4 K and is also compared to results for temperatures ranging from 6 K to 13 K, determined by conventional pulsed electron spin

resonance. Down to a temperature of $230\,\mathrm{mK}$ the relaxation time exhibits a temperature dependence as expected from an uncoupled spin ensemble. Below this temperatures, the T_1 time is found to increase strongly with decreasing temperature, differing significantly from the expected temperature independent behavior.

The thesis closes with a summary and conclusion in chapter. 5.

Chapter 2

Methods

To study the interaction between photons and an ensemble of spins an appropriate environment has to be established. In the framework of this thesis a solid-state based approach is chosen. Here, the photon field is contained in a superconducting microwave resonator formed by coplanar microstructures made of a thin niobium film. Thereby, two different designs of thin film resonator structures are presented, the coplanar waveguide resonator and the lumped element resonator. These one dimensional resonators can be designed to have a very small mode volume, thus greatly enhancing the strength of the resonator photon field and consequently the interaction with a spin [40]. The spin ensemble is contained in an isotopically purified silicon-28 host crystal consisting of phosphorus donors. At the temperature of interest, the donor can be understood as a localized electron with an electron spin $S = 1/2$ and a nuclear spin $I = 1/2$. A donor concentration of $[\mathrm{P}] = 1 \times 10^{17}\,\mathrm{cm}^{-3}$ is used, for which the spins ensemble is paramagnetic and spin-spin interactions are weak, allowing to describe the spin ensemble to first order by its single donor spin features. Using magnetic fields the spin ensemble's electron spin transition frequency can be brought in resonance with a microwave resonator, where both systems will exchange excitation quanta. For an efficient exchange process a large spin polarization is desirable, which can be achieved by increasing the ratio between the Zeeman energy and the thermal energy. Since the interaction with a microwave resonator restricts the spin ensemble's transition frequency to the GHz range, the Zeeman energy cannot be chosen arbitrary. Alternatively, large spin polarizations can be achieved by cooling the two systems to millikelvin temperatures. To this end, a cryogen free dilution refrigerator is employed in combination with microwave generation and detection equipment to perform the experiments. Finally, the mounting of the resonator and spin ensemble in a sample box is presented, which allows their integration into the measurement setup.

2.1 Superconducting Coplanar Microwave Resonators

In the course of this thesis two different designs of coplanar microwave resonators were employed to study the interaction between photons and spins. Both designs are such, that their resonance frequencies are in the $5 - 6\,\mathrm{GHz}$ range, to allow for a direct comparison. In the following, their design parameters and fabrication process are presented, in addition to their integration in the microwave circuitry of the cryogenic measurement setup.

2.1.1 Superconducting Coplanar Waveguide Resonator

A coplanar waveguide resonator (CPWR) is a thin metallic film structure on top of a substrate. The structure consists of a center conductor of width w and two adjacent ground planes separated each by a gap of width s, as illustrated in Fig. 2.1 (a). Basically, a coplanar waveguide (CPW) can be seen as a two dimensional version of a coaxial line, with the center conductor carrying the microwave signal and the ground planes serving as the outer conductor. When introducing two cuts in the center conductor of such a microwave transmission line, boundary conditions for the microwave are modified in the sense, that these cuts represent impedance mismatch points or open boundaries. These two cuts are also termed coupling capacitances, which are engineered to allow microwave photons to couple in or out of the separated resonator structure. The length l of the separated resonator structure defines the boundary conditions of the electromagnetic wave, which forms a standing wave pattern. The corresponding eigenfrequencies of the microwave resonator are given by [41]

$$\frac{\omega_{r,n}}{2\pi} = \frac{c}{2l\sqrt{\epsilon_{\text{eff}}}}(n+1), \qquad n = 0, 1, 2, ..., \quad l = \frac{\lambda}{2}. \tag{2.1}$$

This type of resonator can theoretically support an infinite number of resonant modes n, with the fundamental mode having a wavelength of $\lambda/2$, hence they are also known as $\lambda/2$-transmission line resonators. Assuming a nonmagnetic dielectric the microwaves vacuum velocity of the speed of light c is reduced by an effective permittivity ϵ_{eff}. This effective permittivity is a combination of the two hemispheres of the stucture, the dielectric below (substrate) and above (vacuum) the CPW structure. For a CPW on a substrate of finite thickness h, the effective permittivity is given by [42]

$$\epsilon_{\text{eff}} = 1 + \frac{\epsilon - 1}{2} \frac{K(k_1)}{K(k_1')} \frac{K(k_0')}{K(k_0)}, \tag{2.2}$$

where ϵ represents the dielectric constant of the substrate and K denotes the complete elliptic integral of the first kind. The arguments of K are

$$k_0 = \frac{w}{w + 2s}, \tag{2.3}$$

$$k_1' = \frac{\sinh(\pi w/4h)}{\sinh(\pi(w + 2s)/4h)}, \tag{2.4}$$

$$k_i' = \sqrt{1 - k_i^2}, \qquad i = 1, 2. \tag{2.5}$$

The characteristic impedance Z_0 of the CPW is defined by [42]

$$Z_0 = \frac{30\pi}{\sqrt{\epsilon_{\text{eff}}}} \frac{K(k_0')}{K(k_0)}, \tag{2.6}$$

should be designed to match the characteristic impedance of the microwave circuitry to minimize microwave reflections at the intersection between CPW and cabling [43].

Figure 2.1 (b) shows an exemplary normalized transmission spectrum of one resonator mode. At the resonance frequency ω_r the transmission through the resonator is unity, while far away of the resonance frequency the transmission is zero. For a realistic resonator with losses the line shape is lorentzian with a half width at half maximum (HWHM) of κ_0.
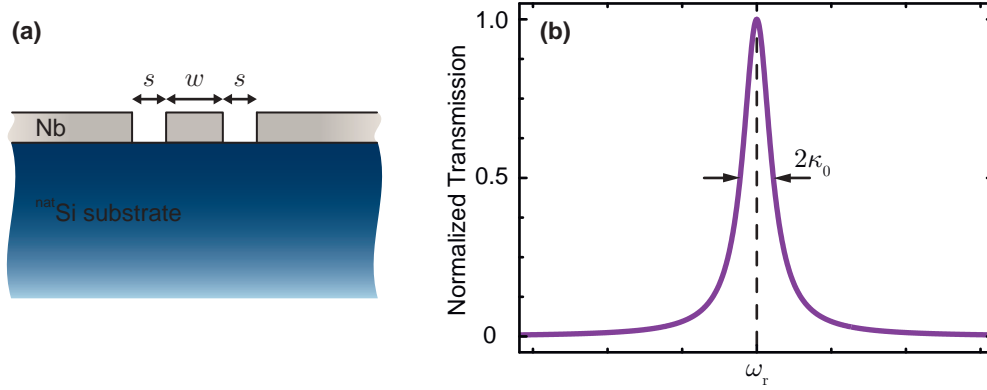
Figure 2.1: (a) Schematic of a CPW cross-section including the center conductor width w and the gap width s. (b) Exemplary normalized transmission spectrum of a CPWR resonant mode. The transmission peaks at the resonance frequency ω_r and exhibits a lorentzian lineshape with a half width at half maximum κ_0.

The losses are attributed to coupling of resonator modes to the continious mode spectrum of the input and output microwave lines via the coupling capacitances, resistive losses, radiation losses and losses in the dielectric [44]. All contribute to the total linewidth κ_0, which characterizes the average decay or loss rate of a resonator photon. A measure for the efficiency of energy or photon storage inside a resonator coupled to input and output lines, is the loaded quality-factor or Q-factor given by

$$Q_n = \frac{\omega_{r,n}}{2\kappa_0}. \tag{2.7}$$

The loaded Q-factor can be separated into an external Q_{ext} and an internal Q-factor Q_{int}

$$\frac{1}{Q_n} = \frac{1}{Q_{ext}} + \frac{1}{Q_{int}}. \tag{2.8}$$

Q_{ext} is governed by the geometry of the CPW and the coupling capacitances, both being independent on external parameters like temperature or magnetic fields. In contrast, Q_{int} depends on dielectric losses in the substrate, radiative losses and resistive losses, which are influenced by such external parameters, especially when using superconducting resonators. Here, the resistive losses depend on the Cooper pair density and kinetic inductance, which on their own depend on temperature and external magnetic fields [44, 45]. Therefore, when performing temperature and magnetic field dependent experiments it is advisable to use a resonator, dominated by its external quality factor. In this way, the performance of the resonator is less influenced by such external parameters. Resonators for which $Q_{ext} \ll Q_{int}$ are known to operate in the overcoupled regime [41].

For the fabrication of the superconducting coplanar waveguide resonators, a $6 \times 10 \, \text{mm}^2$ high resistivity ($> 3 \, \text{k}\Omega\text{cm}$) silicon substrate with a natural isotope composition and a thickness of $525 \, \mu\text{m}$ is used. Via sputtering, a $150 \, \text{nm}$ thick niobium layer is deposited on the substrate. The CPWR structure is defined by optical lithography and reactive ion etching. Finally, Fig. 2.2 depicts a micrograph of the resulting $\lambda/2$ transmission coplanar waveguide resonator structure. The impedance of the coplanar waveguide resonator is designed to match $Z_0 = 50 \, \Omega$, the standard line impedance of the microwave circuitry, which is achieved for a center conductor width of $w = 20 \, \mu\text{m}$ and a gap of $s = 12 \, \mu\text{m}$ (cf.
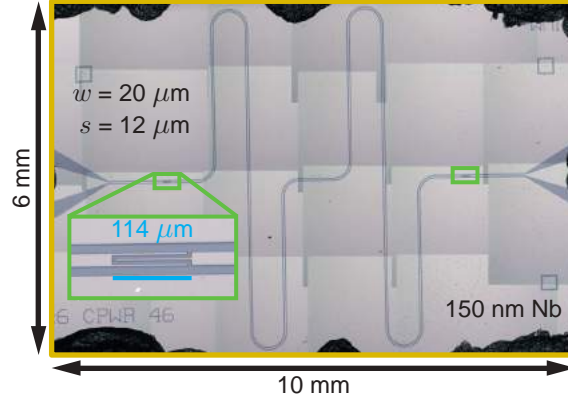
Figure 2.2: Micrograph of the niobium coplanar waveguide resonator. The inset shows a magnification of one of the two coupling capacitances.

Ref. [44]). The effective permittivity ϵ_{eff} is calculated to 6.45 and is in good agreement with the experimentally obtained value of 6.19 for this resonator geometry [44]. With a total length of $l = 23\,\mathrm{mm}$ the fundamental mode is expected to have a resonance frequency $\omega_{\mathrm{r},0} = 2.6\,\mathrm{GHz}$.

2.1.2 Superconducting Lumped Element Resonators

A lumped element resonator (LER) resembles very closely an electrical parallel LC-circuit. Unlike with CPWRs, where capacitance and inductance are linked distributed elements [41], capacitance and inductance are clearly separated in the lumped element design. Figure 2.3 (a) shows a micrograph image of a lumped element resonator made of niobium, used during this thesis. The meandering conductor on the right represents the inductance and is connected to an interdigital capacitance on the left. The whole structure is embedded in the ground plane of a CPW transmission line, while no direct electrical connection is present to the ground plane or the CPW center conductor. Figures 2.3 (b) and (c) show a schematic cross-section of the finger capacitance and the inductance with adjacent CPW, respectively. The location of the cross-sections are indicated by the blue and red arrows in Fig. 2.3 (a). Feeding microwave photons to the resonator structure can be done capacitively and / or inductively from the adjacent broadband CPW transmission line. Thereby, the design of the LER defines the dominant type of coupling [46]. For a mostly inductive coupling the center of the inductance should run alongside the CPW and for a capacitive coupling the finger capacitance structure should be oriented alongside the CPW. A more detailed analysis of the design parameters of a LER can be found in Ref. [46–49]. The resonance frequency of a lumped element resonator is approximately given by [49]

$$\omega_{\mathrm{r}} = \frac{1}{\sqrt{LC}}. \tag{2.9}$$

The resonant mode, determined by the lumped element resonators inductance L and capacitance C, exhibits an uniform current distribution across the inductor [49]. Since the resonance condition is not directly restricted to a certain size, like it is in the case of a CPWR, the lumped element resonator design allows for more compact resonator geometries. Therefore, it is possible to reduce the area of a LER, while leaving the resonance frequency unchanged by appropriately varying the design parameters, e.g. the width of
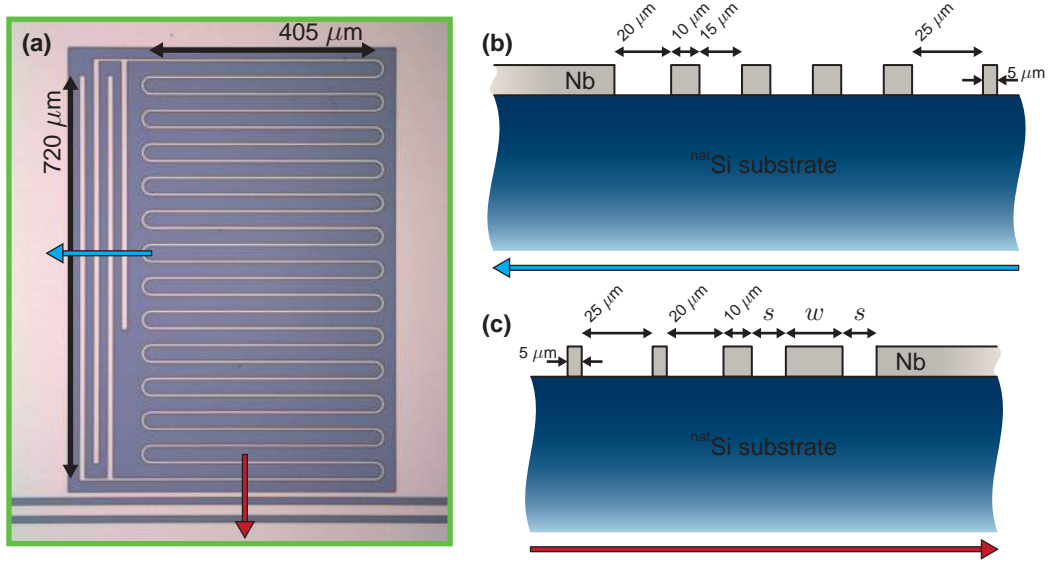
Figure 2.3: (a) Micrograph image of a niobium lumped element resonator. Additionally part of the adjacent CPW transmission line can be seen at the bottom of the image. (b) Schematic cross-section of the finger capacitor structure of the LER, where the blue arrow in (a) shows the location of the cross-section. (c) Schematic cross-section of the inductor and the alongside running CPW, where the position of the cross-section is indicated by the red arrow in (a).

the conductor lines or the number of fingers of the interdigital capacitor. As a drawback, a LER supports only one resonant mode, confining its application to a single frequency window. However, due to its small size it is easy to structure several lumped element resonators on a single chip, having the same dimension as for a coplanar waveguide resonator. Figure 2.4 (a) depicts a chip design with five LERs, all coupled to a common CPW transmission line. To avoid a degeneracy in the individual resonator resonance frequencies, the length of a single finger of the interdigital capacitance is varied for each resonator, resulting in different resonance frequencies.

While the expression (2.9) is of simple form, the values for the inductance L and capacitance C are not easily accesible. They are either obtained by estimations [50] or due to simulation of the whole structure [49]. Here, the lumped element resonator design was choosen in close analogy to the designs presented in Ref. [49, 51]. Using *CST microwave studio* to simulate the complete resonator chip of Fig. 2.4 (a) the final design was optimized to have the resonance frequencies in the desired frequency region around 5 GHz. For the simulation a model was constructed, consisting of a $6 \times 10\,\text{mm}^2$ and 200 nm thick layer of perfect electric conductor (PEC) on top of a $525\,\mu\text{m}$ thick silicon block, representing the niobium thin film and the silicon substrate, respectively. The PEC layer was structured in the same way as shown in Fig. 2.4. Applying a frequency domain solver with adaptive tetrahedral meshing the microwave transmission was simulated, as shown in Fig. 2.4 (b). The simulated transmission spectrum exibits five distinct resonance dips well separated by several MHz. In contrast to the transmission of a CPWR, where the microwave transmission gets maximal in resonance, the lumped element resonator reduces the transmission in resonance. The continuous microwave signal passing the broadband CPW transmission line is resonantly absorbed by a resonator, when the microwave frequency matches its resonance frequency. The resonator reemits the signal with a decay rate κ_0, which destructively interferes with the transmission line microwave signal. A lorentzian shaped
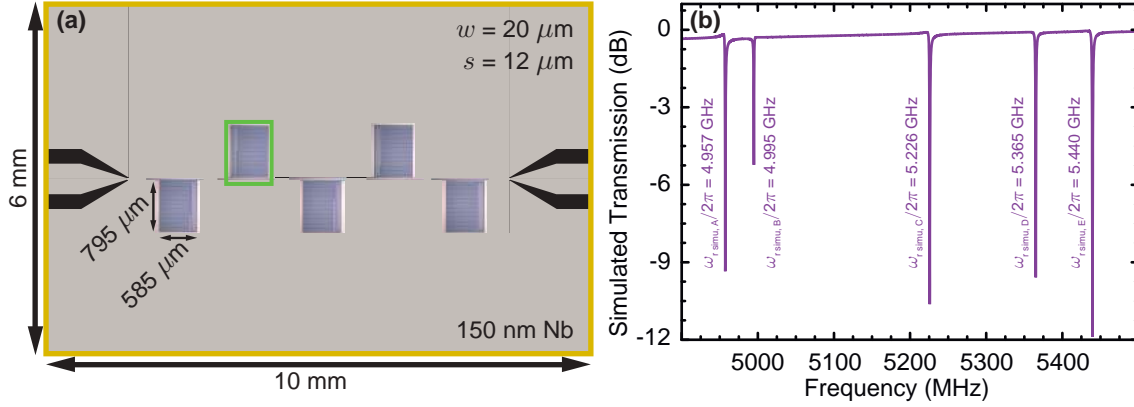
Figure 2.4: (a) Image of a niobium lumped element resonator chip with five resonators coupled to a common CPW transmission line. The LERs are micrograph images, while the rest of the chip is illustrated schematically. The resonator shown in Fig. 2.3 (a) is marked with a green box. (b) CST mircowave studio simulation of the microwave transmission of a similar resonator chip shown in (a).

absorption dip is observed with a half width at half maximum κ_0. However, the resonant dips in Fig. 2.4 (b) exhibit an asymmetric resonance lineshape. When the resonant absorption of the microwave signal is not complete and part of the signal passes the resonator the destructive interference with the remitted signal is also not complete. The absorption dip is phase shifted by the interfering signals and exhibits a Fano resonance lineshape [52]. A detailed analysis method of theses lineshapes is presented in Sec. 3.1.2.

The lumped element resonators utilized in this thesis are fabricated in a similar fashion to the coplanar waveguide resonator. On a $525\,\mu$m thick ^{nat}Si substrate a $150\,$nm thick layer of niobium is deposited, using the sputter technique. The Nb layer is patterned by optical lithography and subsequent reactive ion etching, resulting in the resonator structures shown in Fig. 2.3 (a). The transmission line is designed to be $50\,\Omega$ impedance matched with a center conductor width $w = 20\,\mu$m and a gap width of $s = 12\,\mu$m.

2.2 Phosphorus Doped Silicon

Silicon is a widely used material. It finds application in the construction industry, the metal industry, in synthetic polymers and it forms the basis of modern integrated circuits. This is not surprising, since silicon is the second most element on earth, after oxygen. In addition, it has been and still is a very popular material system in different disciplines of physics. Concerning the focus of this thesis, silicon is also an appealing candidate in the field of quantum information processing either directly or as a host material. In all silicon based quantum computation [53, 54] the nuclear spin carrying isotope ^{29}Si can be utilized as a quantum bit. On the other hand, considering silicon as a host material for paramagnetic impurities enables one to choose between different donors with different spin configurations, taking advantage of their individual properties for potential quantum computation applications [55, 56]. Much effort was put into the enrichment of silicon with its nuclear spin free isotope ^{28}Si during the *Avogadro project* to redefine the kilogram [57]. This isotopically purified ^{28}Si has typically a residual ^{29}Si concentration of less than $1\,\%$, making it nearly nuclear spin free. Paramagnetic donors residing in such a ^{28}Si
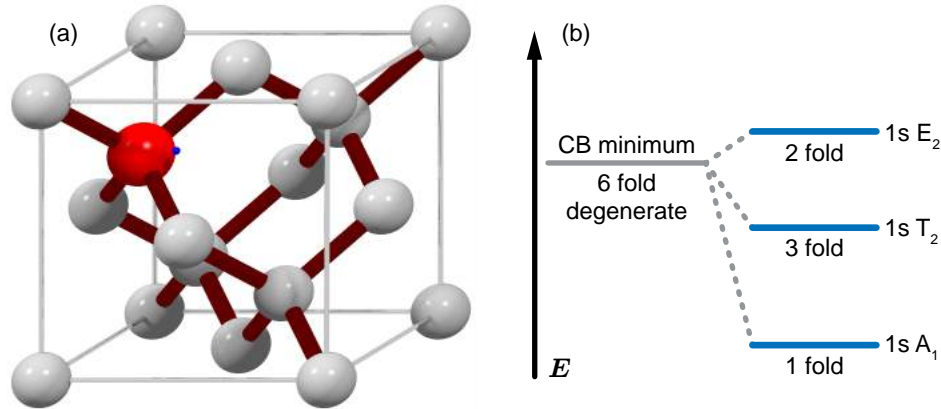
Figure 2.5: (a) Schematic of the diamond cubic crystal structure of silicon. The grey atoms represent silicon atoms and the red a phosphorus donor with its accompanying donor electron in blue. The dark red joints between the atoms illustrate their covalent binding, while the outer gray joints serve to define the cubic unit cell. (b) Schematic of the energy levels of phosphorus donors in silicon [59].

"semiconductor vacuum" [58] are less prone to interfering magnetic field fluctuations from residual nuclear spins, reducing the lifetime of a prepared donor spin state. To this end, doped ^{28}Si is particularly suitable for quantum information storage due to exceptional long coherence times. In particular, phosphorus donors are very attractive candidates, since they set the current benchmark of electron and nuclear spin coherence times, exceeding $0.5\,\mathrm{s}$ and $39\,\mathrm{min}$, respectively [4, 5, 11]. With these perspectives phosphorus donors in silicon are the central object of investigation in this thesis.

The silicon atoms of the host crystal are arranged in diamond structure, and have four covalently bonded next neighbors. Introducing a phosphorus atom into this lattice by interchanging it with a silicon atom, leaves one of the five valence electrons of ^{31}P unbound, schematically shown in Fig. 2.5 (a). The donor electron provides an uncompensated magnetic moment with S = 1/2 in addition to the nuclear magnetic moment with I = 1/2 of the ^{31}P nucleus, which are coupled via the hyperfine interaction A. The electronic structure or the wave function of such a shallow donor can be described by an effective-mass theory [60–63] or with a modern full numerical approach [64], solving the full donor Hamiltonian. The hydrogen like potential of the donor lifts the sixfold degenerate conduction band minimum of silicon into a triplet $1sT_2$ and doublet $1sE_2$ excited state and a singlet $1sA_1$ ground state for the donor electron [65, 66], schematically shown in Fig. 2.5 (b). For the typical temperature range used in this thesis, only the nondegenerate singlet state $1sA_1$ is occupied. Note, that crystal strain and external electric fields, as well as for the case of thin film silicon the electronic structure can be changed [65, 67]. In the ground state, the six band minimas are equally populated resulting in a symmetric state, resulting in an isotropic g-factor [65]. Additionally, the hyperfine interaction A results from the symmetric nature of the electronic ground state wavefunction. This gives rise to a finite probability of the donor electron being at the position of the nucleus, providing an isotropic interaction between the nucleus and the electron in the ground state, which is called the Fermi-contact hyperfine interaction [64–67]. Therefore, in magnetic resonance experiments on an unstrained material, the g-factor and the hyperfine interaction can be considered fully isotropic.

2.2.1 Spectroscopic Features

The focus of this thesis is on magnetic resonance experiments on phosphorus doped silicon (Si:P). The entire information about the spin properties of an individual phosphorus donor is contained in the spin Hamiltonian [68]

$$H = \frac{g_{\mathrm{eP}}\mu_{\mathrm{B}}}{\hbar}\mathbf{B}_0\hat{\mathbf{S}} + \frac{g_{\mathrm{NP}}\mu_{\mathrm{N}}}{\hbar}\mathbf{B}_0\hat{\mathbf{I}} + \frac{A}{\hbar^2}\hat{\mathbf{S}}\hat{\mathbf{I}}, \tag{2.10}$$

with the phosphorus donor electron (nuclear) g-factor g_{eP} (g_{NP}), the Bohr (nuclear) magneton μ_{B} (μ_{N}), the hyperfine interaction A and the reduced Planck constant $\hbar$. The first term describes the Zeeman interaction between the electron spin and the static magnetic field $\mathbf{B}_0$, the second, the nuclear Zeeman interaction of the nuclear spin with the magnetic field and the last term describes the hyperfine interaction between nuclear and electron spin. The individual electron and nuclear spin operators $\hat{\mathbf{S}}$ and $\hat{\mathbf{I}}$ are composed of the Pauli spin matrices

$$\hat{\mathbf{S}} = \frac{\hbar}{2}\begin{pmatrix}\hat{\sigma}_{\mathrm{x}}\\\hat{\sigma}_{\mathrm{y}}\\\hat{\sigma}_{\mathrm{z}}\end{pmatrix}, \qquad \hat{\mathbf{I}} = \frac{\hbar}{2}\begin{pmatrix}\hat{\sigma}_{\mathrm{x}}\\\hat{\sigma}_{\mathrm{y}}\\\hat{\sigma}_{\mathrm{z}}\end{pmatrix}, \tag{2.11}$$

$$\hat{\sigma}_{\mathrm{x}} = \begin{pmatrix}0 & 1\\1 & 0\end{pmatrix}, \hat{\sigma}_{\mathrm{y}} = \begin{pmatrix}0 & -i\\i & 0\end{pmatrix}, \hat{\sigma}_{\mathrm{z}} = \begin{pmatrix}1 & 0\\0 & -1\end{pmatrix}. \tag{2.12}$$

With zero applied magnetic field the solution in the eigenbasis of (2.10) is a symmetric spin triplett state and an antisymmetric spin singlet state separated in energy by the hyperfine interaction. By applying a magnetic field $\mathbf{B}_0 = B_0\hat{\mathbf{e}}_{\mathrm{z}}$ the degeneracy is lifted by the Zeeman interaction and, in the limit of high fields, four distinct energy levels are present in the spin system with electron spin eigenstates $|\uparrow\rangle$, $|\downarrow\rangle$ and nuclear spin eigenstates $|\Uparrow\rangle$, $|\Downarrow\rangle$. Figure 2.6 (a) shows the resulting Breit-Rabi diagram in frequency units for phosphorus in silicon, using $g_{\mathrm{eP}} = 1.9985$, $g_{\mathrm{NP}} = 2.2632$ and $A/h = 117.53\,\mathrm{MHz}$ [68,69]. The eigenenergies of the system, including the corresponding high field spin states, are

$$|\uparrow,\Uparrow\rangle: \quad E_1 \;=\; \frac{A}{4} + \frac{B_0}{2}\left(g_{\mathrm{eP}}\mu_{\mathrm{B}} + g_{\mathrm{NP}}\mu_{\mathrm{N}}\right), \tag{2.13}$$

$$|\uparrow,\Downarrow\rangle: \quad E_2 \;=\; -\frac{A}{4} + \frac{1}{2}\sqrt{A^2 + B_0^2\left(g_{\mathrm{eP}}\mu_{\mathrm{B}} - g_{\mathrm{NP}}\mu_{\mathrm{N}}\right)^2}, \tag{2.14}$$

$$|\downarrow,\Downarrow\rangle: \quad E_3 \;=\; \frac{A}{4} - \frac{B_0}{2}\left(g_{\mathrm{eP}}\mu_{\mathrm{B}} + g_{\mathrm{NP}}\mu_{\mathrm{N}}\right) \text{ and} \tag{2.15}$$

$$|\downarrow,\Uparrow\rangle: \quad E_4 \;=\; -\frac{A}{4} - \frac{1}{2}\sqrt{A^2 + B_0^2\left(g_{\mathrm{eP}}\mu_{\mathrm{B}} - g_{\mathrm{NP}}\mu_{\mathrm{N}}\right)^2}. \tag{2.16}$$

Figure 2.6 (b) displays part of the high field evolution of the four energy states in a magnetic field range, where the Zeeman splitting is in the order of 4.9 GHz the typical resonance frequency of the microwave resonators, used in this thesis. With the spin angular momentum of $\pm\hbar$ of the photon, exciting the transition between two different spin states is possible. Dependent on the frequency of the photon these transitions are either due to nuclear magnetic resonance (NMR) or electron spin resonance (ESR), which typically reside in the MHz or GHz regime, respectively. The resonance frequency of the applied
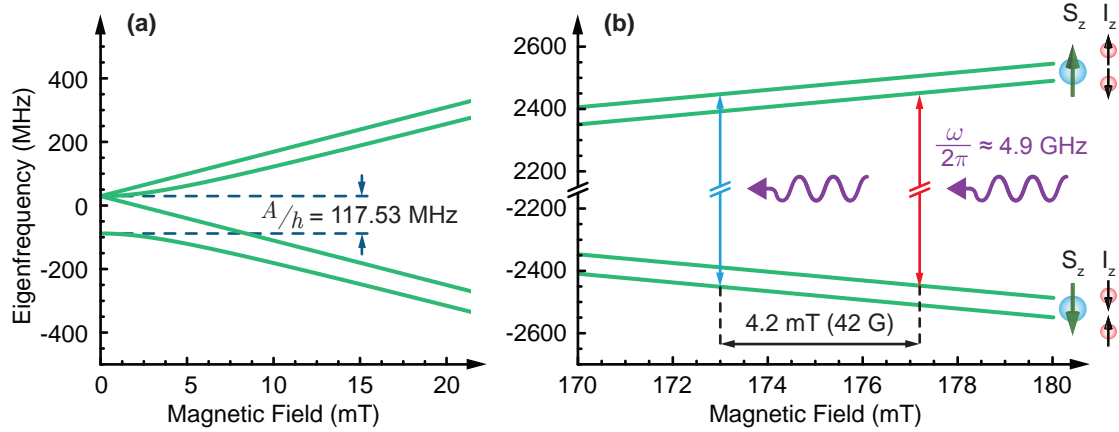
Figure 2.6: Breit-Rabi diagram of phosphorus in silicon under consideration of the electron and nuclear Zeeman interactions and the hyperfine interaction. (a) Low field part of the Breit-Rabi diagram showing the evolution of the threefold degenerate spin triplet state and the nondegenerate spin singlet state with increasing magnetic field. The Zeeman interactions lifts the degeneracy of the triplet state, resulting in four distinct energy states. (b) Breit-Rabi diagram in a magnetic field region where the Zeeman splitting is in the same frequency range as the typical resonance frequencies of the employed microwave resonators. The blue and red lines show two possible ESR transitions with same resonance frequency, but separated in field by 4.2 mT, a characteristic fingerprint of phosphorus donors in silicon. On the right of (b) the four electron and nuclear spin states are illustrated by green and black arrows, respectively.

resonators restricts the possible transitions to nuclear spin conserving electron spin-flips. This permits two electron spin transitions having the same transition frequency at two different magnetic fields, denoted as the low-field (LF) and the high-field electron spin transition. The two transitions are separated by $4.2\,\mathrm{mT}$, a characteristic fingerprint of the hyperfine interaction of phosphorus donors in silicon (see Fig. 2.5 (b)).

Many experiments in conventional cavity based electron spin resonance focus on a fixed microwave frequency spectroscopy, while sweeping the external magentic field B_0. Figure 2.7 depicts an exemplary electron spin resonance spectrum, assuming a magnetic field region as shown in Fig. 2.6 (b) and a frequency matching the two transitions indicated by the blue and red arrows. The spectrum exhibits two resonance absorption dips at magnetic fields where the resonance condition for the low field transition $\left|\downarrow,\Uparrow\right\rangle \rightarrow \left|\uparrow,\Uparrow\right\rangle$
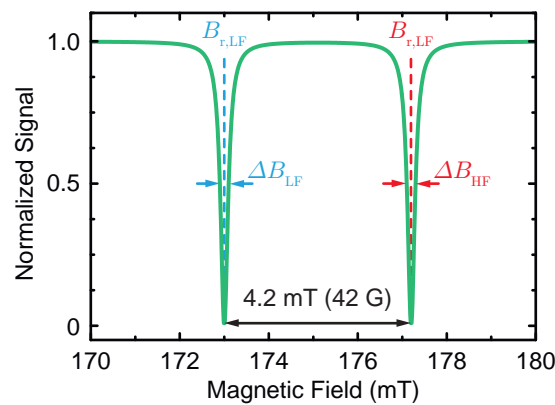

Figure 2.7: Exemplary electron spin resonance spectrum (resonance depths and linewidths are arbitrary).

at $B_{0,\mathrm{LF}}$ or the high field transition $|\downarrow,\Downarrow\rangle \rightarrow |\uparrow,\Downarrow\rangle$ at $B_{0,\mathrm{HF}}$ is fulfilled. Using isotopically purified ^{28}Si, the resonance lineshape is lorentzian [70] with a full width at half maximum (FWHM) of $\delta B_{\mathrm{LF/HF}}$. The magnetic field linewidth can be coined as an effective loss rate of the excited spin system via

$$\gamma = \frac{g_{\mathrm{eP}}\mu_{\mathrm{B}}}{\hbar}\frac{\Delta B}{2}. \tag{2.17}$$

Here, $\gamma/2\pi$ represents a frequency HWHM and is governed by the homogeneous or inhomogeneous spectral linewidth of the spin ensemble [71, 72].

2.2.2 Sample Preparation

In this thesis a $20\,\mu$m thin isotopically purified ^{28}Si crystal doped with phosphorus is investigated. The ^{28}Si features a residual ^{29}Si concentration of $0.1\,\%$ and has phosphorus donor concentration of $[\mathrm{P}] = 1 \times 10^{17}\,\mathrm{cm}^{-3}$. Originally the silicon host crystal was chemical vapor deposition grown on a boron doped silicon substrate with natural isotope composition ($^{\mathrm{nat}}$Si) with a boron concentration of $[\mathrm{B}] = 4.5 \times 10^{19}\,\mathrm{cm}^{-3}$. On top of the ^{28}Si a layer of $500\,$nm thick arsenic doped $^{\mathrm{nat}}$Si with $[\mathrm{As}] = 6 \times 10^{18}\,\mathrm{cm}^{-3}$ was located. Figure 2.8 schematically shows the different silicon layers, which formed a $\mathrm{pn}^-\mathrm{n}^+$ diode structure employed to study the influence of the Stark shift on the hyperfine interaction of the phosphorus donors [73]. The arsenic and boron doping concentration are both above the metal insulator transition, ensuring conductivity even at liquid helium temperatures. Due to the flip-chip mounting of the SiP sample on the superconducting coplanar resonator (cf. Sec. 2.3.3) these conductive layers would either short-circuit the coplanar resonator structure or induce considerable microwave losses due to eddy currents. Therefore, these layers were removed by physical reactive ion etching in the case of the arsenic doped layer and by mechanical polishing with consecutive physical reactive ion etching for the boron doped substrate. The resulting very fragile thin ^{28}Si crystals were placed with utmost carefulness onto the coplanar resonator structure and studied during the course of this thesis.
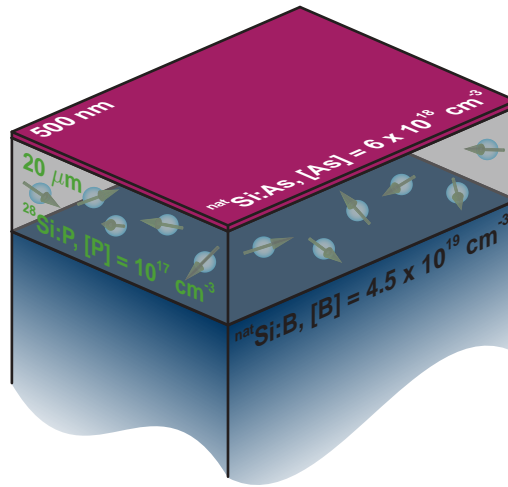

Figure 2.8: Schematic of the layer structure of the investigated phosphorus doped silicon. Originally the ^{28}Si crystal was chemical vapor deposition grown on a heavily boron doped $^{\mathrm{nat}}$Si substrate and cap by an arsenic doped $^{\mathrm{nat}}$Si layer. To avoid any unwanted influences on the used microwave resonator the arsenic and boron doped layers were removed.

2.3   Cryogenic Microwave Setup

To study the interaction between a superconducting microwave resonator and a phosphorus donor spin ensemble under the requirements of quantum information processing ($k_{\mathrm{B}}T < \hbar\omega_{\mathrm{r}}$) and for high spin polarizations ($k_{\mathrm{B}}T < g_{\mathrm{eP}}\mu_{\mathrm{B}}B_0$), the two systems have to be cooled to millikelvin temperatures. This requires a specific layout of the microwave circuitry, in order to prevent that room temperature thermal noise interacts with the experiment. In addition, to connect the microwave resonators with standard microwave cabling a sample box is utilized, forming the interface between the coplanar waveguide structures and the coaxial cabling. For the characterization of the superconducting resonators a liquid helium cryostat was used, which can be operated in a temperature range of $4.2\,\mathrm{K}$ to $2\,\mathrm{K}$. A detailed description of the liquid helium cryostat can be found in Ref. [74].

2.3.1   Dilution Refrigerator

All experiments of this thesis concerning the coupling of a microwave resonator to a spin ensemble are conducted in an *Oxford Industries Triton*$^{\mathrm{TM}}$ *400 Cryofree*® dilution refrigerator. It combines a cryogen free pulse tube cooler with a dilution refrigerator unit, where the pulse tube precools the dilution unit to $4\,\mathrm{K}$ a requirement for operation [75]. The cryostat is further equipped with a superconducting 3d vector magnet system. It consists of a superconducting solenoid in between two superconducting Helmholtz coil pairs oriented perpendicular to each other. In the lab frame, the Helmholtz coils can apply a magnetic field vector in the x-y-plane and the solenoid in the z-direction. The maximal fields along the x, y and z-direction are $1\,\mathrm{T}$, $1\,\mathrm{T}$ and $6\,\mathrm{T}$, respectively.

   Figure 2.9 shows a schematic overview of the dilution refrigerators temperature stages and the corresponding microwave circuitry, in addition to an image showing the open cryostat with the temperature stages highlighted. The different temperature stages are thermally well isolated from each other to minimize the thermal heat load on the low temperature stages. To guarantee the thermal ankering of the semi-rigid microwave signal lines, commercial attenuators of various strength at the temperature stages are used, indicated in Fig. 2.9. For the input line this is achieved by mounting attenuators at the different temperature stages not only attenuating any signal in total by $70\,\mathrm{dB}$ but also thermally anchoring inner and outer conductor of the coaxial cables. The installed attenuators reduce the average number of thermal photons at the input of the resonator, e.g. to ~ 0.05 for a frequency of $5\,\mathrm{GHz}$ [76], without taking cable attenuation into account. The small signals of the sample are intentionally not attenuated in the output line. However, to block thermal noise two cryogenic *Quin Star Technology Inc. CTH0408KCS* circulators are mounted at mixing chamber temperatures and an additional one on the still stage. These three-port devices are connected such, that signals from the sample can pass the circulators, while signals coming from higher temperatures are terminated with $50\,\Omega$. The isolation between the not transmitting ports is specified to $20\,\mathrm{dB}$, summing up to $40\,\mathrm{dB}$ for the in series connected circulators at the millikelvin temperature stage. To increase the output signal amplitude and signal to noise ratio a cryogenic *Low Noise Factory LNF-LNC4 8A* high-electron-mobility transistor (HEMT) amplifier is mounted at $4\,\mathrm{K}$. The gain of the amplifier is $+35\,\mathrm{dB}$ within a frequency range of 4-8 GHz. Prior to signal detection, the signals are further amplified with either of two room temperature
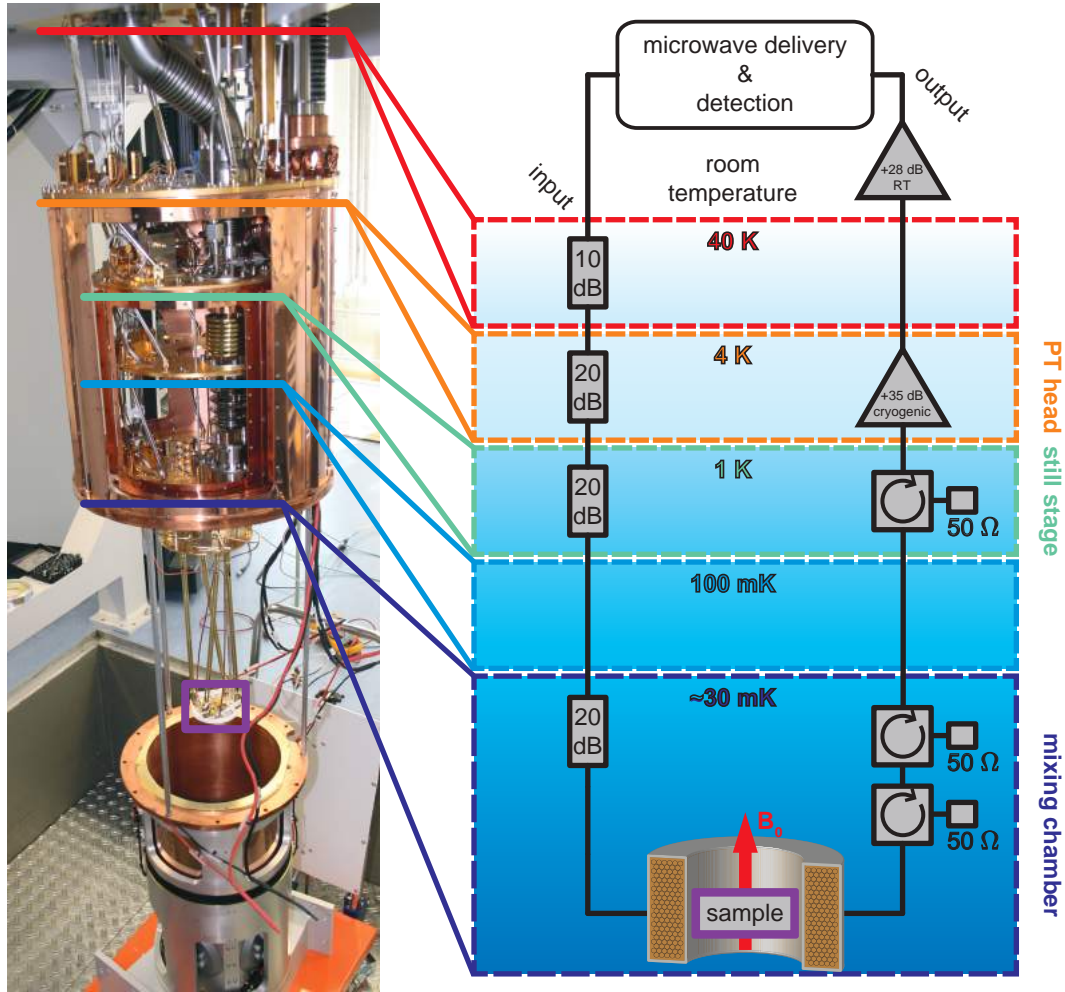
Figure 2.9: Image of the open cryogen free dilution refrigerator together with a schematic of its temperature stages, including the microwave circuit and the distribution of its components on the temperature stages. The temperature stages in the image are highlighted and assigned to their corresponding stage in the schematic.

amplifiers, a *Kuhne electronic LNA BB 202 A* amplifier with a gain of $+28$ dB or a *B&Z Technology BZP110UC1* amplifier with a gain of $+37$ dB.

2.3.2 Microwave Delivery & Detection

For the continuous wave (CW) spectroscopy (cf. Ch. 3) and the time domain spectroscopy (cf. Ch. 4) different microwave generation and detection schemes are employed. The two measurement techniques have opposing requirements. For the low power CW experiments a low measurement bandwidth (slow measurement time, high signal to noise) is essential. On the other hand, for the high power time domain experiments a high measurement bandwidth (fast measurement time, low signal to noise) is required.

In the case of the CW spectroscopy the steady state of the coupled resonator / spin ensemble is investigated. The microwave transmission is detected as a function of frequency and external magnetic field in the vicinity where resonator and spin ensemble are in resonance. To avoid saturation of the paramagnetic system, low microwave powers are necessary. This requires a high resolution detection with a low measurement band-

width, which is provided by a vector network analyzer (VNA). Additionally, the VNA is able to simultaneously generate and detect microwave signals, allowing for phase sensitive measurements by referencing the detected signal to the output signal. The ratio between detected and emitted signal is known as the scattering-parameter or S-parameter. A n-port network can be fully characterized by a set of S-parameters spanning a $n \times n$ scattering matrix, considering all port reflections S_{ii} and combinations of port to port transmissions S_{ij}, with $i, j = 1...n$ and $i \neq j$ [77]. Here, the investigated network consists of the two ports of the input and output lines of the cryogenic microwave setup including the sample. Therefore, all S-parameters can be summarized in a 2×2 scattering matrix

$$\hat{S} = \begin{pmatrix} S_{11} & S_{12} \\ S_{21} & S_{22} \end{pmatrix}, \tag{2.18}$$

where S_{11} (S_{22}) is the signal reflection at the input (output), while S_{21} (S_{12}) is the transmission from the input to the output (the output to the input). The detected and emitted signals are known as wave quantities and have units of $\sqrt{W}$ [77]. Under the knowledge of the exact impedance Z of the investigated network, the wave quantities can be translated into voltage signals by $V = \sqrt{PZ}$. For the squared magnitude of the S-parameter, the measured quantity is represented by a power ratio. For the interpretation of the experiments conducted in this thesis the squared magnitude of the microwave transmission $|S_{21}|$ is investigated. For the measurements a *Rhode&Schwarz ZVA8* is utilized and also a *Keysight PNA*, which supports frequency sweeps from low to high frequencies and vice versa.

For the time domain experiments the non-equilibrium dynamics of the coupled resonator / spin ensemble are studied. Here, for fixed microwave frequency and external magnetic field the response of the coupled system to a strong microwave pulse is detected. The time scales of the dynamic response is in the range of µs to ns, which requires for a fast detection mechanism or a high measurement bandwidth. The detection is performed by a *Rhode&Schwarz FSV* spectrum analyzer, able to detect fast signals in the time domain with a bandwidth of up to 28 MHz. In contrast to the VNA, the employed spectrum analyzer is phase insensitive and measures the magnitude of the microwave power. The microwave pulses are generated by a *Rhode&Schwarz SMF100* microwave source, which is triggered by a *LeCroy ArbStudio* arbitrary waveform generator (AWG), providing the pulse sequence. To ensure that the measurement devices are operated at identical frequencies, all devices are synchronized to an external 10 MHz reference oscillator, provided by a *Stanford Research Systems Model FS25 Rubidium Frequency Standard.*

2.3.3   Sample Mounting

To establish the connection between the microwave circuitry of the cryostat and the coplanar resonator the resonator chip is mounted in a gold plated oxygen-free high thermal conductivity copper box, as depicted in Fig. 2.10. The box is designed such, that it can hold 6×10 mm^2 chips having a thickness of 525 µm. To improve the thermal connection between the resonator chip and the box a small amount of silver glue is applied in the chip socket of the box. For the connection of the center and outer conductor of the niobium thin film structures two types of connectors are applied, to allow for a different sample box mounting for the CPWR and the LERs. The two resonator designs require different
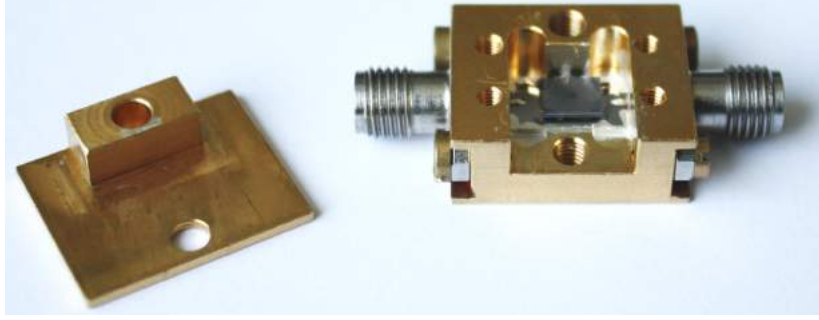
Figure 2.10: Photograph of an open gold plated oxygen-free high thermal conductivity copper sample box together with its corresponding lid. The two SMA connectors allow for an easy integration into the cryogenic microwave setup. Mounted into the box is a thin film niobium resonator covered with pieces of phosphorus doped ^{28}Si crystal. The crystal pieces are held in position by an additional piece of ^{nat}Si substrate.

B_0-field orientations, to fulfill the ESR conditions best (see Fig. 2.11). Flange mounted *Rosenberger* panel jack SMA to stripline connectors are used to connect the CPWR chip and flange mounted *Amphenol Connex* right angle panel jack SMA to round pin connectors for the LER chip. The round pin of the right angle SMA connectors is worked to have a flat surface parallel to the CPW plane, to enable a similar connection to the CPW center conductor as with the SMA to stripline connectors. To establish a good electrical connection between the CPW center conductor and the stripline / flattened round pin, as well as between the CPW ground planes and the box, silver glue is used.

Pieces of the prepared thin ^{28}Si crystal (cf. Sec. 2.2) are carefully placed on top of the niobium resonator structure. The appropriate placement of the crystal on the CPWR and the LER can be seen in Fig. 2.11 (a) and (b), respectively. To fix the small crystal pieces in position, they are covered by an additional piece of ^{nat}Si substrate. For the CPWR the substrate is cemented on the niobium film by *Fixogum* rubber cement and in the case for the LER the substrate is held and additionally pressed onto the resonator structure by a nylon screw mounted into the box lid (not shown in Fig. 2.10). The loaded box is installed in the cryogen free dilution refrigerator such, that it is located in the sweet-spot of the superconducting solenoid, a region of best field homogeneity. To maximize the ESR signal the microwave oscillatory magnetic field B_1 needs to be perpendicular to the static magnetic field B_0. With the B_1 field running nearly circularly around the cross-section
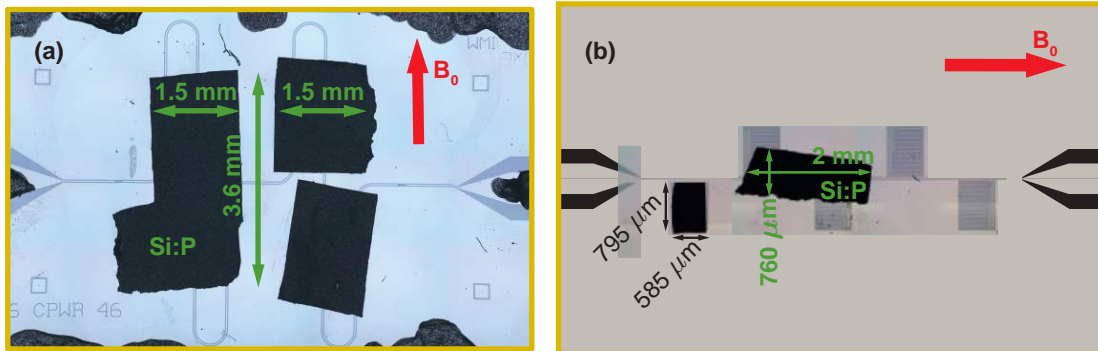
Figure 2.11: Micrograph of the (a) CPWR and (b) LER loaded with pieces of phosphorus doped ^{28}Si crystal. The red arrows indicate the orientation of the external static magnetic field B_0.

of the coplanar conductor [78] the B_0 field is required to be oriented in parallel to the conductor. For the experiments concerning the CPWR the resonator is operated at its first harmonic, with the B_1 field anti-nodes located at 1/4 and 3/4 of the resonator length (cf. Fig. 2.2 (a)). Therefore, the B_0 field is oriented parallel to the CPW lines running vertically, indicated by the red arrow in Fig. 2.11 (a). In the case of the LER the static magnetic field B_0 is oriented in parallel to the CPW transmission line, which is also in parallel to the major part of the resonators inductor lines (red arrow in Fig. 2.11 (b)). The two resonator designs are appropriately mounted to fulfill the B_0 field orientation requirements.

Chapter 3

Continuous Wave Spectroscopy

A characterization of the interaction between a superconducting microwave resonator and an ensemble of phosphorus donor spins is performed, by studying the dynamical response of the hybrid system, to a continuous weak microwave drive. With the system driven into a steady state, the resonator transmission spectrum is analyzed, allowing to determine the relevant parameters of the coupled system, like the microwave resonator's loss rate κ_0, the loss rate of the spin ensemble γ and the collective coupling strength g_{eff}. The regime where g_{eff} exceeds the individual loss rates of the subsystems κ_0 and γ, is denoted as the strong coupling regime. Here, the two subsystems can coherently exchange energy or information, without its loss during the interaction process. Reaching the strong coupling regime is a mandatory requirement for the realization of a quantum memory, combining the fast processing capabilities of the microwave resonator and the long storage times of the spin ensemble.

The chapter begins with the characterization of the superconducting microwave resonators in Sec. 3.1. For the characterization, the resonator and the spin ensemble are far detuned, not interacting with each other. The parameters of the resonators are determined initially at liquid helium temperatures in a calibrated microwave spectroscopy setup and are compared to the parameters found at $50\,\text{mK}$, using the uncalibrated millikelvin setup. Comparing the spectroscopic data from both setups, allowed the calibration of the millikelvin setup, and hereby the absolute microwave power incident on the resonator can be determined. Section 3.1.3 discusses the dispersion of the resonance frequency of the resonator as a function of the applied static magnetic field. The resonator dispersion measured at a temperature of $50\,\text{mK}$ is modeled and an estimate of the sample misalignment is given. Next, an introduction to the theoretical model, describing the interaction between resonator and spin system, is provided in Sec. 3.2. Based on the Jaynes-Cummings model, the interaction between a single photon and a single spin is illustrated. In the following, the transition to the Tavis-Cummings model is performed, allowing to describe the interaction of a single photon with an ensemble of spins. The steady state solutions to this model are discussed, defining three different regimes of coupling. Section 3.3 presents the results of the microwave spectroscopy on the CPWR / phosphorus donor spin ensemble hybrid system, in a regime of high cooperation. The coupling is characterized and is compared to a numerical simulation. The limitations for reaching the strong coupling regime are discussed and possible solutions are presented. Finally, the temperature dependence of the collective

coupling g_{eff} is analyzed, for temperatures ranging from $50\,\mathrm{mK}$ up to $3.5\,\mathrm{K}$. A statistical model is developed to describe the observed temperature dependence, which is found to scale with the square root of the number of thermally polarized spins. The chapter closes with the first-time demonstration of strong coupling between a superconducting LER and an ensemble of phosphorus donors in Sec. 3.4. The found collective coupling exceeds the individual loss rates of the resonator and the spin ensemble by more than a factor of two. However, the transmission spectrum exhibits an asymmetric linewidth of the microwave resonator's normal mode splitting, which is not expected from the Tavis-Cummings model. The spectrum is modeled, by assuming an additional incoherent coupling between the microwave resonator and the spin ensemble, which is mediated indirectly via an incoherent bath of frequency modes.

3.1 Superconducting Resonator Transmission Calibration

The calibration measurements of the superconducting microwave resonators are performed at liquid helium temperatures using the cryostat described in Ref. [74] and a HP8722D VNA. Connected to the microwave circuitry of the cryostat is a sample box either loaded, with a CPWR or a LER chip. As the microwave attenuation of this setup's cabling is known, the microwave transmission spectra of the two resonators can be calibrated for this attenuation. This allows to determine the microwave transmission of only the resonators, which allows to determine the external and internal quality factors. Additionally, using the calibrated microwave transmission of the resonators, the microwave attenuation of the millikelvin setup is determined.

3.1.1 CPWR Calibration

For the spin resonance experiments, the superconducting CPWR is brought in physical contact with the thin pieces of phosphorus doped ^{28}Si crystals, as disscused in Sec. 2.3.3. Figure 3.1 shows the power transmission $|S_{21}|^2$, in logarithmic scale, as a function of the VNA frequency for the first three harmonics of the CPWR. The spectra show both the calibrated and uncalibrated transmission spectra, where the difference in transmission is given by the attenuation of the setup's microwave circuitry. For the calibrated measurements the peak transmission of the resonator can be identified. For an ideal case, the full signal is transmitted in resonance, corresponding to a peak transmission of 1. However, due to finite losses the transmission is reduced and quantified as the insertion loss IL. The insertion loss depends on the coupling coefficient q as [41, 43]

$$IL = -20\log\left(\frac{q}{q+1}\right)\ \mathrm{dB}, \qquad \text{where } q = \frac{Q_{\mathrm{int}}}{Q_{\mathrm{ext}}}. \qquad (3.1)$$

The coupling coefficient gives a measure for the effectiveness of coupling microwave photons in or out of the resonator. Basically, two regimes of couplings can be distinguished [41]. (i) For weakly coupled or undercoupled resonators ($q < 1$), the external quality factor Q_{ext} is large, due to small coupling capacitances. This corresponds to a small coupling rate of microwave photons in and out of the resonator, increasing both the reflectivity of microwave photons at the input of the resonator and their storage time in the resonator. Due to the smaller internal quality factor Q_{int} the loss rate of a resonator photon is determined by the
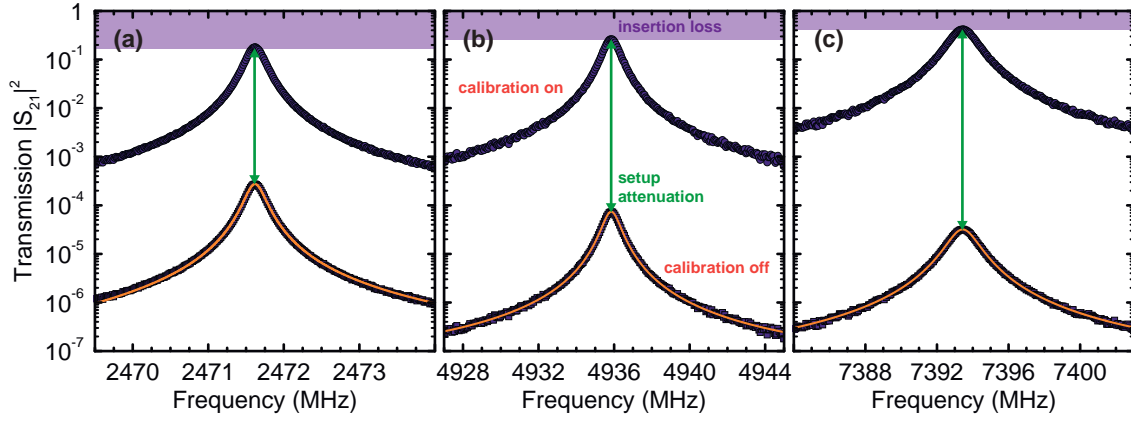
Figure 3.1: Power transmission of the CPWR at liquid helium temperatures as a function of the VNA frequency, for the fundamental (a), first (b) and second (c) harmonic resonator mode. The squared symbols show the transmission of the cryostats microwave cabling and the CPWR, fitted using a lorentzian function (solid orange line). The round symbols show only the transmission through the CPWR, with the microwave cabling attenuation calibrated out.

internal loss channels (cf. Sec. 2.1.1). The loaded quality factor (2.7) is dominated by the internal quality factor, thus is also dependent on external parameters like temperature or external magnetic fields (cf. Sec. 2.1.1).

(ii) Resonators which are strongly coupled to the input and output microwave lines ($q > 1$) exhibit a high peak transmission. The coupling capacitances are large and the external quality factor Q_{ext} is low. Therefore, resonant photons have an increased rate to couple in and out of the resonator, corresponding to a short storage time. The internal quality factor Q_{int} is large, which translates in a small coupling rate to internal loss channels (cf. Sec. 2.1.1). With $Q_{\text{int}} > Q_{\text{ext}}$ the loaded quality factor is governed by the external quality factor, making the resonator less dependent on external parameters. Resonators operating in a regime where $q > 1$ are called overcoupled [41].

By fitting the calibrated resonator transmission $|S_{21}|^2$ using a lorentzian function

$$|S_{21}|^2 = A_0^2 \frac{\kappa_0^2}{(\omega - \omega_{\text{r}})^2 - \kappa_0^2}, \tag{3.2}$$

the insertion loss is determined by the amplitude A_0, via $IL = -20 \log(A_0)$. The loaded Q-factor is determined by Eq. (2.7), using the found resonance frequency ω_{r} and resonator loss rate κ_0. Solving Eq. (3.1) for the internal Q-factor by using Eq. (2.8) yields

$$Q_{\text{int},n} = \frac{Q_n}{1 - 10^{-\frac{IL_n}{20}}}, \tag{3.3}$$

where the index n represents the harmonic mode number. Finally, with the loaded and internal Q-factors determined, Q_{ext} can be obtained using Eq. (2.8). The extracted parameters for the first three harmonics of the CPWR shown in Fig. 3.1 at liquid helium temperatures are summarized in Tab. 3.1.

Figure 3.2 shows the quality factors as a function of the mode number. All Q-factors decrease with increasing harmonic mode number n, due to increased radiative losses [45]. The dependence of the mode number n on the loaded quality factor is described by [41]

$$Q_n = Q_{\text{off}} + \frac{C}{2Z_0 C_{\text{k}}^2 \omega_{\text{r},n}}, \tag{3.4}$$
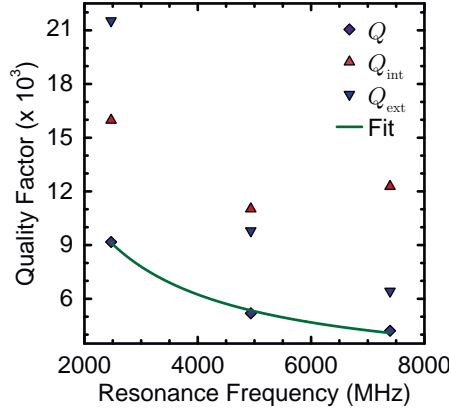
Figure 3.2: Loaded, internal and external quality factors of the CPWR at liquid helium temperatures as a function of the harmonic mode number. The resonance frequency dependence of the loaded Q-factor is described by Eq. 3.4 (solid green line).

assuming a mode number independent offset Q_{off}. The characteristic impedance Z_0 of the microwave circuitry is $50\,\Omega$ and the line capacitance per length C of the resonator is given by

$$C = 4\epsilon_0\,\epsilon_{eff}\,\frac{lK(k_0)}{2K(k_0')},\tag{3.5}$$

with the arguments of the complete elliptic integral of the first kind K defined in Eq. (2.5). ϵ_0 and ϵ_{eff} are the vacuum permittivity and the effective permittivity, respectively and l represents the length of the resonator center conductor. Fitting Eq. (3.4) to the loaded quality factor (solid line in Fig. 3.2), allows to determine experimentally the coupling capacitance C_k of the resonator. By assuming $Z_0 = 50\,\Omega$ and $C = 1.81\,\mathrm{pF}$ the fit yields $Q_{off} = 1562$ and a coupling capacitance of $12.4\,\mathrm{fF}$, which is in good agreement with the coupling capacitances of similar designs, reported in Ref. [41].

The uncalibrated transmission spectrum of the CPWR's first harmonic mode, mounted in the cryogen free dilution refrigerator setup (cf. Sec. 2.3.1), at a base temperature of $50\,\mathrm{mK}$ and at zero magnetic field is shown in Fig. 3.3 (a). In the following, the focus will be only on the first harmonic mode, since most of the experiments are conducted with this mode. To calibrate the spectra obtained in this setup, the external quality factor Q_{ext} is assumed to be temperature independent and to be equal to the value determined at $4\,\mathrm{K}$. A lorentzian fit to the uncalibrated spectra of Fig. 3.3 (a), allows to evaluate the resonance frequency $\omega_{r,1}$ to $4939.25\,\mathrm{MHz}$ and the loss rate $\kappa_{0,1}$ to $0.344\,\mathrm{MHz}$. Using Eq. (2.7) a loaded Q-factor $Q_1 = 7171.9$ is found. Together with $Q_{ext} = 9604.6$ the internal Q-factor is calculated by Eq. (2.8) to $Q_{int,1} = 28316$. Finally, applying Eq. (3.1) provides $IL_1 = 2.54\,\mathrm{dB}$. With IL known, the transmission spectrum can be calibrated for the attenuation by the whole microwave circuitry, which is determined to $19.4\,\mathrm{dB}$. To determine the

mode n	$\omega_r/2\pi$ (MHz)	$2\kappa_0/2\pi$ (MHz)	Q	Q_{int}	Q_{ext}	IL in dB
0	2471.62	0.270	9171.8	15977.8	21531.8	7.4
1	4935.85	0.952	5186.8	11026.4	9793.7	5.5
2	7393.44	1.754	4215.8	12278.5	6420.1	3.7

Table 3.1: Summary of the determined parameters of the CPWR at liquid helium temperatures.
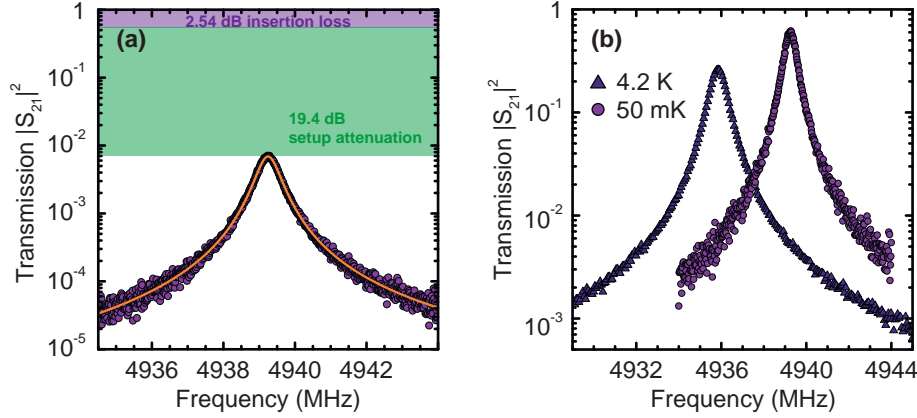
Figure 3.3: (a) Uncalibrated power transmission $|S_{21}|^2$ (symbols) as a function of frequency of the CPWR's first harmonic mode at a temperature of 50 mK. The orange solid line is a lorentzian fit to the spectrum. The insertion loss of the resonator and the attenuation of the cryogen free dilution refrigerator microwave circuitry are accentuated by colored boxes. (b) Comparison of the calibrated transmission spectra measured at 4 K and 50 mK.

attenuation of the microwave lines, the total attenuation of the measurement setup of 19.4dB is compared to the nominal attenuation and amplification values of the attenuators (70dB) and amplifiers (+35dB for the 4K HEMT and +28dB for the room temperature amplifier), respectively (cf. Sec. 2.3.1)). Hereby, we obtain for the attenuation of the microwave lines a total of 12.4 dB.

Figure 3.3 (b) compares the calibrated transmission spectrum at 4 K with the spectrum obtained at 50 mK. The resonance frequency slightly increased for 50 mK additionally with a decrease of the loss rate. The former is due to a decrease of the kinetic inductance of the superconductor [45] and the latter is attributed to the increase of the internal quality factor by about a factor of three. Therefore, at millikelvin temperatures the CPWR is far in the overcoupled regime, increasing its robustness against externally applied static magnetic fields, as desired for the envisaged experiments.

3.1.2 LER Calibration

The mounted sample box is loaded with a LER chip, with three resonators covered by pieces of phosphorus doped ^{28}Si (cf. Sec. 2.3.3). The pieces are hold in position by an additional piece of ^{nat}Si substrate, covering four resonators. At liquid helium temperatures the microwave transmission of the resonators is detected as a function of frequency, as shown in Fig. 3.4. The five resonators are labeled with A to E, beginning with A for the lowest resonance frequency resonator and ending with E for the resonator with the highest resonance frequency. Using this notation, the resonators A, B and C are covered by ^{28}Si and the additional piece of ^{nat}Si substrate covers resonators A to D. The microwave transmission of all resonances show an asymmetric lorentzian line shape, resulting from an interference between the transmission line microwave signal and the resonator signal coupling back into the transmission line. The asymmetry can be described in the framework of the diameter correction method (DCM), modeling the asymmetry by an impedance mismatched between the resonators input and output impedance [79]. The model assumes a complex valued external quality factor, describing the impedance mismatch as a complex contribution. The magnitude of the microwave transmission $|S_{21}|$ can be described within
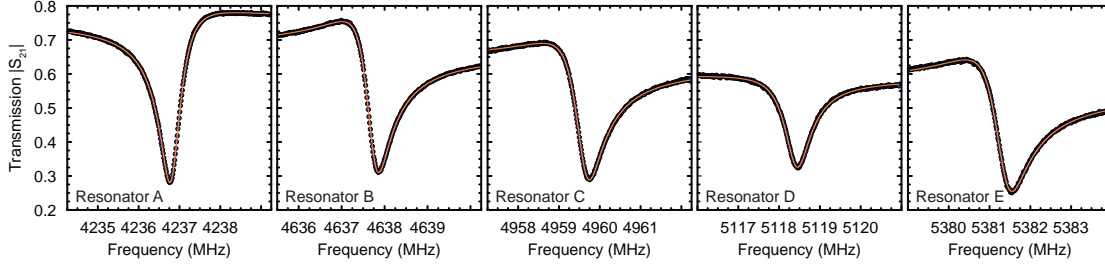
Figure 3.4: Calibrated microwave transmission $|S_{21}|$ (symbols) as a function of the VNA frequency and at liquid helium temperatures, for the LERs A to E. The asymmetric lorentzian lineshapes are fitted using Eq. (3.6) (solid orange lines).

the DCM by

$$|S_{21}| = S_0 \left(1 - \frac{Q \left| Q_{\text{ext}}^{-1} \right| e^{i\phi}}{1 + 2iQ \frac{\omega - \omega_{\text{r}}}{\omega_{\text{r}}}} \right). \tag{3.6}$$

The prefactor S_0 refers to the microwave transmission away from resonance, defining the baseline of the resonance dip. $|Q_{\text{ext}}|$ is the magnitude of the complex external Q-factor and ϕ represents the phase angle of the $|Q_{\text{ext}}|$ vector in the complex plane. Fitting Eq. (3.6) to the transmission spectra $|S_{21}|$ of the five LER (orange solid line in Fig. 3.4) yields their loaded and external Q-factors. Since the loaded Q-factor is a real valued quantity, the real part of the complex external Q-factor Q_{ext}^{real} is required to determine Q, which modifies Eq. (2.8) to

$$\frac{1}{Q} = \text{Re} \left\{ \frac{e^{i\phi}}{|Q_{\text{ext}}|} \right\} + \frac{1}{Q_{\text{int}}} = \frac{\cos(\phi)}{|Q_{\text{ext}}|} + \frac{1}{Q_{\text{int}}}, \tag{3.7}$$

and allows to determine the internal Q-factor from the parameters obtained by the fit. The determined parameters from the five calibrated transmission spectra of the lumped element resonators are summarized in Tab. 3.2. For an absorption resonator, like the LER, a calibration of the microwave circuitry is not necessary to evaluate the resonators Q-factors. The relevant parameters are defined by the relative depth of the resonance dip, the resonance position and the linewidth. However, to determine the energy stored in the resonator, the quantitative knowledge of the power in the nearby transmission line is required. For a calibrated microwave transmission spectroscopy, the amplitude factor S_0 corresponds to the power in the CPW feedline. Therefore, the calibrated transmission of the CPW feedline at $4.2\,\text{K}$ can be used to cross-calibrate the cryogen free dilution refrigerator setup. Note, that the microwave attenuation of a superconducting transmission line exhibits a finite temperature dependence, which has to be considered for such a calibration. However, the leading order of the temperature dependence of the microwave attenuation is inversely proportional to $1 - \left(\frac{T}{T_{\text{c}}} \right)^4$ [80], where T_{c} represents the critical temperature of the superconductor. A change in S_0 of less than $5\,\%$ is expected for a change of temperature from $4.2\,\text{K}$ to $50\,\text{mK}$ ($T_{\text{c}} = 9.2\,\text{K}$ [81]). Due to the small change, the calibrated transmission data at $4.2\,\text{K}$ is used directly for a cross-calibration the cryogen free dilution refrigerator setup.

Figure 3.5 (a) shows the raw, uncalibrated transmission $|S_{21}|$ of the LER chip at $50\,\text{mK}$, with and without an applied static magnetic field B_0. In the measured frequency range, S_0 exhibits an oscillation, with an amplitude change by approximately a factor of two. The oscillation is a result of impedance mismatches in the microwave circuitry, inducing
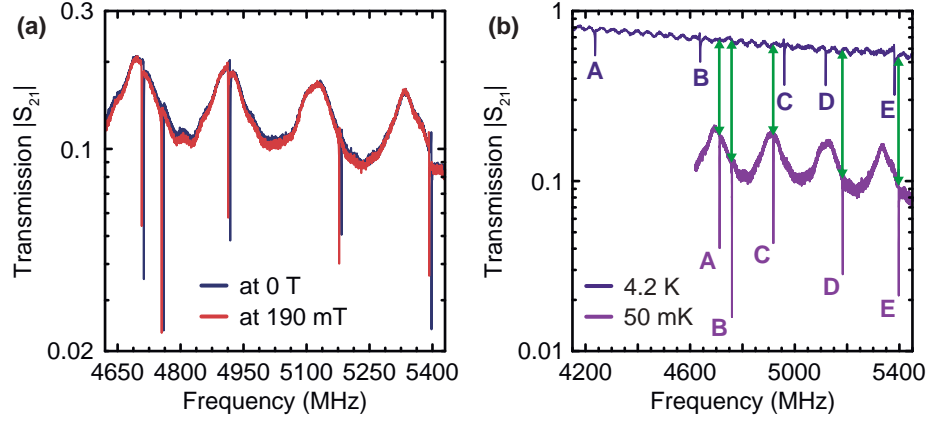
Figure 3.5: Broadband transmission $|S_{21}|$ of the LERs, as a function of the VNA frequency. (a) Comparison of the transmission spectra measured at zero static magnetic field and 190 mT, for $T = 50$ mK. (b) Calibrated transmission at 4.2 K compared to the uncalibrated transmission at 50 mK, both with no magnetic field applied. The resonant modes for the two temperatures are labeled from A to E. The green arrows indicate the attenuation due to the microwave circuitry of the dilution refrigerator setup, for each resonant mode at $T = 50$ mK.

microwave reflections [43]. For the case of multiple reflection planes in the circuit, parasitic resonant modes can form, analog to the desired resonant mode of a CPWR. The resonance frequency corresponds to a characteristic length scale via Eq. (2.1), under consideration of the effective dielectric of the circuits coaxial cables. The measured transmission oscillates with a frequency of 105 MHz, which corresponds to a characteristic length of 1 m (using $\epsilon_{\text{eff}} = 2.03$ for solid Polytetrafluoroethylene (PTFE) [82]). It is assumed, that the self-made flattened pin of the right angle panel jack SMA connectors (cf. Sec. 2.3.3), at the sample box are responsible for these oscillations. Reference measurements, using *Rosenberger* stripline connectors (cf. Sec. 2.3.3), showed a flat transmission spectrum without the parasitic resonant mode.

However, the major part of the LER experiments were conducted using the former configuration of the setup. Comparing the two transmission spectra of Fig. 3.5 (a) shows, that the parasitic oscillation is approximately magnetic field independent and only the LER modes are shifting in resonance frequency (see Sec. 3.1.3). Therefore, the results of the coupling experiments are expected to be independent of the oscillating background.

For a coarse calibration of the LERs the calibrated broadband transmission spectrum at liquid helium temperatures is compared to the uncalibrated spectrum at 50 mK, as show in Fig. 3.5 (b). By fitting the uncalibrated LER modes using Eq. (3.6) the amplitude factor S_0 is obtained. At the resonance frequency of each LER at 50 mK, the difference between S_0

Res.	$\omega_{\text{r}}/2\pi$ (MHz)	$2\kappa_0/2\pi$ (MHz)	Q	Q_{int}	Q_{ext}^{real}	ϕ (rad)	S_0
A	4236.87	0.809	5235.9	13697.2	8475.9	-0.357	0.757
B	4637.65	0.746	6218.3	11929.6	12988.5	0.763	0.670
C	4959.52	0.924	5365.3	10728.9	10732.4	0.668	0.631
D	5118.38	0.903	5665.9	10128.2	12860.1	0.245	0.587
E	5381.21	1.051	5121.9	9652.3	10912.4	0.833	0.554

Table 3.2: Summary of the determined parameters of the LERs at liquid helium temperatures.
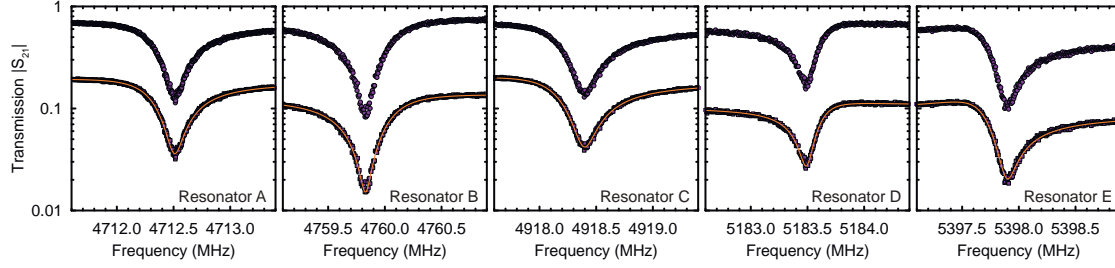
Figure 3.6: Uncalibrated (square symbols) and calibrated (round symbols) transmission $|S_{21}|$ of each LER at 50 mK. The orange solid line represents as fit to the uncalibrated spectra, using Eq. (3.6).

and the calibrated transmission is determined (green arrows in Fig. 3.5 (b)). The difference is attributed to the attenuation due to the dilution refrigerator's whole microwave circuitry and to the parasitic oscillation, ranging from 10.86 dB to 15.51 dB. This contains the contribution of the built in 70 dB attenuation of the microwave signal input line and the amplification by +35 dB and +37 dB (4 K HEMT amplifier and room temperature *B&Z Technology BZP110UC1* amplifier, respectively (see Sec. 2.3.1)) of the output line. Thus, the bare attenuation by the microwave cabling, modified by the parasitic oscillation, ranges from 8.86 dB to 13.51 dB, comprising the result obtained from the CPWR calibration in Sec. 3.1.1.

Figure 3.6 shows the uncalibrated and corrected transmission $|S_{21}|$ of all five resonant modes of the LER chip, as a function of the VNA frequency. The resonator parameters are determined by fitting Eq. (3.6) to the spectra and are summarized in Tab. 3.3. Comparing the 4.2 K and 50 mK parameter sets, shows an overall increase of the resonator performance at millikelvin temperatures. The resonance frequencies of resonators A, B, D and E increased, which is assumed to correlate with the decrease of the kinetic inductance of the superconductor with decreasing temperatures [45]. Only resonator C showed an opposing behavior, however the reason for a decrease of resonance frequency with decreasing temperature is unclear. The observed change of the external quality factor is assumed to result from a change of the inductive coupling of the resonators. Since the coupling of the LER to the transmission line is governed by a geometry dependent capacitance in addition to a temperature dependent inductance (cf. Sec. 2.1.2), a change in the external Q-factor is also expected. However, the exact dependency is not known, as a systematic study of the superconducting microwave resonator's temperature dependence was not in the focus of this thesis.

Res.	$\omega_r/2\pi$ (MHz)	$2\kappa_0/2\pi$ (MHz)	Q	Q_{int}	Q_{ext}^{real}	ϕ (rad)	Setup Att. (dB)
A	4712.42	0.627	7511.6	37217.1	9411.0	0.335	11.41
B	4759.92	0.714	6668.8	56190.6	7566.8	−0.275	14.17
C	4918.26	0.700	7028.6	29236.6	9253.1	0.460	10.86
D	5183.56	0.376	13779.9	49434.3	19105.7	−0.465	14.97
E	5397.71	0.459	11770.0	40544.3	16584.4	0.832	15.51

Table 3.3: Summary of the determined parameters of the LERs at 50 mK.

3.1.3   Resonator Field Dispersion

To study the interaction between the superconducting microwave resonators (LER and CPWR) and the phosphorus doped ^{28}Si crystal, the two systems need to be in resonance. Since the resonator frequency is fixed mostly by its geometry, it is convenient to tune the resonance frequency of the spin ensemble, by applying a static magnetic field B_0 (cf. Sec. 2.2). Although, the tuning of the resonance frequency via the Zeeman interaction is isotropic, the performance of the superconducting coplanar resonator depends on the orientation of B_0. Niobium belongs to the type-II superconductor family, with a lower critical field B_{c1} of about $200\,\text{mT}$ for bulk material and for temperatures much lower than the critical temperature $T_c = 9.2\,\text{K}$ [80, 83, 84]. When applying an external magnetic field larger than B_{c1}, but smaller than the upper critical field B_{c2}, the superconductor enters the Shubnikov state [85]. In this state, normal conducting flux vortices are present in the material, which impose a source of additional loss [86, 87]. For a thin film superconductor the critical fields become anisotropic, mainly due to demagnetization effects [80, 85]. In particular, the critical field B_{c1} is enhanced for fields applied in parallel with the film surface, if the thickness of the film d is comparable or smaller than the effective magnetic penetration depth λ_{eff}. This parallel critical field is given by [88]

$$B_{||c1} = 2\sqrt{6}B_{c1}\frac{\lambda_{\text{eff}}}{d}. \tag{3.8}$$

The effective penetration depth for a $150\,\text{nm}$ thick, polycrystalline niobium film, at $T = 50\,\text{mK}$ is about $90\,\text{nm}$ [81], resulting in $B_{||c1} \approx 590\,\text{mT}$. Thus, for an in-plane field smaller than $B_{||c1}$ the performance of the superconducting resonator does not strongly depend on the externally applied magnetic field. However, with the experimental setup a perfectly in-plane aligned magnetic field is hard to achieve. The perpendicular critical field is much smaller than B_{c1}, as the effective perpendicular magnetic field is enhanced due to demagnetization effects [80, 85]. This enhancement can be estimated by the ratio of the center conductor width w and the film thickness d. For a $150\,\text{nm}$ thick superconducting film, the perpendicular field is enhanced by a factor of 133. Thus, fields larger than $1.5\,\text{mT}$ applied normal to the superconducting surface are sufficient to exceed the lower critical field B_{c1}. The typical field strength required to tune the Zeeman interaction into resonance with the microwave resonator does not exceed $180\,\text{mT}$ in the experiments of this thesis (cf. Sec. 2.2). Therefore, the misalignment is required to be smaller than $0.5\,^\circ$, to not exceed the perpendicular critical field of $1.5\,\text{mT}$.

   For magnetic fields greater than the lower critical field B_{c1} the resonator losses increase significantly, but for magnetic fields below B_{c1}, the resonator is influenced as well. To determine the dispersion of the resonator under the influence of a static magnetic field, the resonator transmission $|S_{21}|^2$ is measured as a function of the VNA frequency for fixed discrete magnetic fields B_0, at a temperature of $50\,\text{mK}$. The resulting dispersion for the first harmonic of a CPWR and a LER is shown in Fig. 3.7 (a) and (b), respectively. The spectra show high (low) transmission when the VNA frequency matches the resonance frequency of the CPWR (LER). For both resonators, the resonance frequency decreases with increasing static magnetic field B_0. The shift in resonance frequency, from zero field to $160\,\text{mT}$, is $0.073\,\%$ for the CPWR, accompanied with an increases of the loss rate by $10\,\%$. For the LER the resonance frequency shift is $0.066\,\%$, while the loss rate stays unchanged with increasing magnetic field. The shift in resonance frequency is due to a
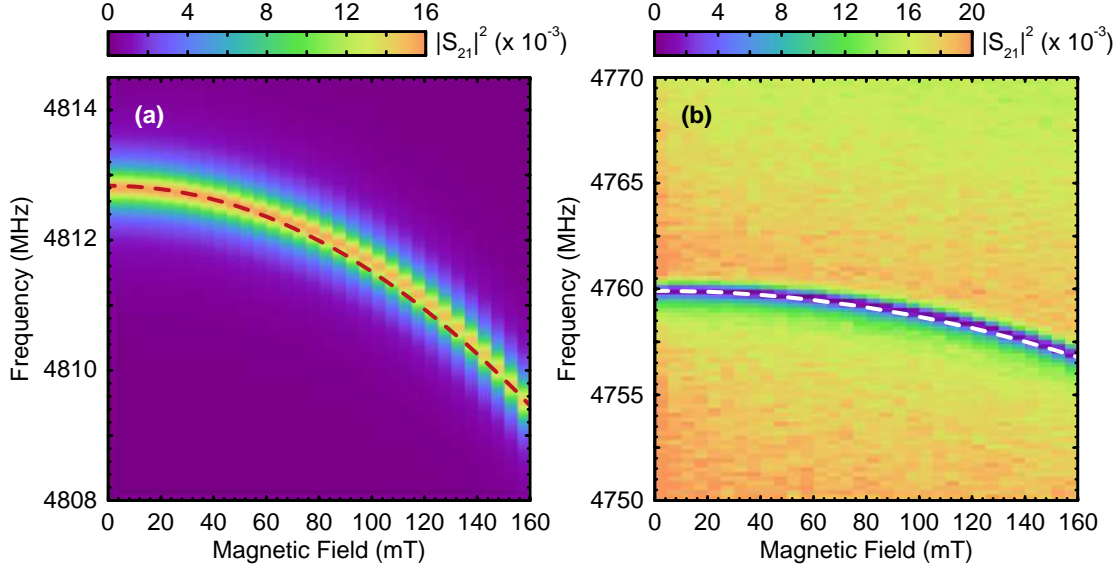
Figure 3.7: Uncalibrated power transmission $|S_{21}|^2$ of a (a) CPWR and (b) LER, as a function of the VNA frequency and static magnetic field B_0. The dashed lines in the spectroscopy data are fits to the resonance frequency dispersion, using the dependence defined in Eq. (3.9). The CPWR measured in spectrum (a) is made of a 200 nm thick niobium film, instead of a 150 nm thick film, but is otherwise of equal design.

change of the total inductance L of the resonator, which is a sum of the kinetic inductance L_k of the superconductor and the geometric inductance L_{geo}. Hereby, L_{geo} is defined by the geometry of the resonator structure, while L_k is governed by the temperature and magnetic field dependent inertia of moving cooper pairs [41]. The kinetic inductance is proportional to λ_{eff}^2, which is inversely proportional to the square root of the explicit magnetic field dependent cooper pair density n_s [80,85]. For the relation between resonance frequency ω_r and static magnetic field B_0 this yields

$$\omega_r = \frac{1}{\sqrt{C\left(L_{geo} + L_k\right)}} \propto \frac{1}{\lambda_{eff}} \propto \sqrt{n_s\left(T, B_0\right)} = \sqrt{n_s\left(T, 0\right)\left(1 - \frac{B_0^2}{B_{||c1}^2}\right)}. \qquad (3.9)$$

The dashed lines in Fig. 3.7 represent fits to the evolution of $\omega_r/2\pi$ using the dependence of Eq. (3.9). Although, the obtained values for $B_{||c1}$ are unrealistic high, as they exceed the calculated $B_{||c1} = 590\,\text{mT}$ by more than one order of magnitude, the fits demonstrate, that the measured resonator dispersions follow very well the dependence of Eq. (3.9). The given relation between ω_r and B_0 is valid for fields smaller than B_{c1}. For higher fields, the additional losses by flux vortices are expected to change this relation. Therefore, the superconducting niobium can be assumed to be in the Meißner phase, indicating that the applied magnetic field is smaller than $B_{||c1}$ and the misalignment of the sample is less than $0.5\,°$.

3.2 Coupling of Photons and Spins

For a qualitative description of the interaction of an ensemble of spins with the oscillating magnetic field of a microwave resonator a theoretical model is required, allowing to quantify the effectiveness of the coupling. In the following, the relevant parameters are introduced

on the basis of the Jaynes Cummings model, describing the coupling between a single two-level system and a single quantized field mode. This model is extended, by increasing the number of two-level systems, resulting in the Tavis-Cummings model. Finally, the results of this model assuming a continuous drive are discussed, in addition to a categorization of the coupling strength in three different regimes.

3.2.1   Jaynes-Cummings Model

This section illustrates the interaction between a single field mode and a two-level atom on the basis of the Jaynes Cummings (JC) model [89], following the arguments in Ref. [90,91]. Treating the field quantum mechanically for the first time produced a theoretical model, which has found many applications in the field of quantum information processing. Basis is the JC-Hamiltonian

$$H_{\mathrm{JC}} = H_{\mathrm{field}} + H_{\mathrm{atom}} + H_{\mathrm{inter}}, \tag{3.10}$$

describing the field, the two-level atom and their interaction, respectively.

The field Hamiltonian shall represent the energy of the microwave resonator in the experiment. The quantization of the resonator field, into single quantas of energy, is achieved by introducing the bosonic creation and annihilation operators $a^\dagger$ and a

$$H_{\mathrm{field}} = \hbar\omega_{\mathrm{r}} \left(a^\dagger a + \frac{1}{2} \right). \tag{3.11}$$

The constant energy term of $\hbar\omega_{\mathrm{r}}/2$ corresponds to the zero point energy of the vacuum field. Considering only the energy part influenced by the interaction between the two systems, this term is typically neglected.

The second term in Eq. (3.10) describes the energy levels of the two-level system. In this case, each of the two ESR transitions of the phosphorus donor electron spin represents the two-level system. A general form of the atom Hamiltonian is given by

$$H_{\mathrm{atom}} = \sum_{k=g,e} E_j \sigma_{kk} = E_g \sigma_{gg} + E_e \sigma_{ee} = \frac{\hbar\omega_{\mathrm{s}}}{2} \underbrace{\left(\sigma_{ee} - \sigma_{gg} \right)}_{\sigma_{\mathrm{z}}} + \mathbb{1}\frac{1}{2} \left(E_g + E_e \right), \tag{3.12}$$

where the transition operator $\sigma_{kk} = |k\rangle\langle k|$ projects the eigenenergies of the ground state E_g and the excited state E_e of the two-level system. For the case of a phosphorus donor, the eigenenergies of the ground state would be represented by E_4 (E_3) and for the excited state by E_1 (E_2), corresponding to the low (high) field spin transition (cf. Sec. 2.2.1). Using $E_e - E_g = \hbar\omega_{\mathrm{s}}$ and the identity of the transition operator $\sigma_{gg} + \sigma_{ee} = 1$, allows to express the two energy levels by the Pauli spin matrix σ_{z} and the spin transition energy $\hbar\omega_{\mathrm{s}}$, offset by a constant energy term. As with the field Hamiltonian, the term of constant energy can be neglected. The exact transition energies are given by the spin Hamiltonian in Eq. (2.10). For simplicity only one of the two ESR transitions is considered in the following.

Assuming, that the microwave field and the phosphorus donor spin interact via a magnetic dipole interaction, the interaction term is given by

$$H_{\mathrm{inter}} = \boldsymbol{\mu}\mathbf{B}_1 = \frac{g_{\mathrm{eP}}\mu_{\mathrm{B}}}{\hbar}\mathbf{S}\mathbf{B}_1. \tag{3.13}$$

The magnetic moment operator depends on the spin operator $\mathbf{S}$, as defined in Eq. (2.11). The corresponding eigenvalues for a spin with $s = 1/2$ are $\mathbf{S}^2|m\rangle = \hbar^2 s(s+1)|m\rangle =$

$\hbar^2 \frac{3}{4} |m\rangle$ and $S_z |m_k\rangle = \hbar m_k |m_k\rangle$, where $m_{k=g} = -1/2$ and $m_{k=e} = 1/2$. Introducing additionally the transition operator yields

$$\boldsymbol{\mu} = \frac{g_{eP}\mu_B}{\hbar} \mathbf{S} = \frac{g_{eP}\mu_B}{\hbar} \sum_{k,l} |k\rangle \langle k| \mathbf{S} |l\rangle \langle l| = \sum_{k,l} M_{kl}\sigma_{kl}, \qquad \text{with } k,l = g,e. \qquad (3.14)$$

Here, σ_{kl} connects the two energy levels with a transition probability given by the transition matrix element $M_{kl} = \frac{g_{eP}\mu_B}{\hbar} \langle k| \mathbf{S} |l\rangle$. The magnetic field operator $\mathbf{B}_1$ can be applied in the dipole-approximation, since the wavelength of the microwave field is much larger than the dimension of the phosphorus donor spin [90]. Thereby, it is assumed, that the microwave field magnitude is not spatially changing in the vicinity of the spin under investigation, allowing to neglect the spatial dependence of the field. With the spin assumed to be located at the origin, the magnetic field operator is given by

$$\mathbf{B}_1 = B_1 \left(\left(\hat{\mathbf{k}} \times \hat{\mathbf{e}} \right) a + \left(\hat{\mathbf{k}} \times \hat{\mathbf{e}}^* \right) a^\dagger \right) = B_1 \left(\hat{\mathbf{e}}_B a + \hat{\mathbf{e}}_B^* a^\dagger \right). \qquad (3.15)$$

The microwave field propagates along the unit wave vector $\hat{\mathbf{k}}$, which can be assumed to be real for a propagation in vacuum. $\hat{\mathbf{e}}_B$ is the unit polarization vector of the magnetic field and is oriented perpendicular to the wave vector $\hat{\mathbf{k}}$ and the polarization $\hat{\mathbf{e}}$ of the accompanying electric field. The magnitude B_1 is normalized to the ground state energy density of the microwave resonator [2, 3, 90]

$$\frac{1}{2}\frac{\hbar\omega_r}{2} = \frac{1}{2\mu_0} \int B_1^2 dV = \frac{1}{2\mu_0} B_1^2 V_m, \qquad (3.16)$$

$$B_1 = \sqrt{\frac{\mu_0 \hbar\omega_r}{2V_m}}, \qquad (3.17)$$

with V_m being the mode volume of the resonator. Note, that the energy stored in the resonator field is equally distributed in the magnetic and electric field. This is taken into account by the factor of $1/2$ on the left hand side of (3.16) [2]. Thus, the interaction term writes

$$H_{\text{inter}} = \boldsymbol{\mu}\mathbf{B}_1 = \sum_{k,l} M_{kl}\sigma_{kl}B_1 \left(\hat{\mathbf{e}}_B a + \hat{\mathbf{e}}_B^* a^\dagger \right)$$

$$= \sum_{k,l} \hbar\sigma_{kl} \left(g_{kl} a + g_{kl}^* a^\dagger \right), \qquad \text{where } g_{kl} = \frac{M_{kl}\hat{\mathbf{e}}_B B_1}{\hbar}, \qquad (3.18)$$

introducing the single photon single spin coupling constant g_{kl}. The coupling constant describes the rate of excitation exchange between the microwave resonator field and the single phosphorus donor spin. If the probabilities for the spin transitions are equal ($M_{kl} = M_{lk}$), the coupling constant can be simplified to $g = g_{kl} = g_{lk}$. The microwave field employed in the conducted experiments has a linear polarization. Choosing the polarization vector to $\hat{\mathbf{e}}_B = \hat{\mathbf{e}}_x$, allows to further rewrite the interaction term to

$$H_{\text{inter}} = B_1 \left(\sigma_{eg} \left(M_{eg}\hat{\mathbf{e}}_x a + M_{eg}\hat{\mathbf{e}}_x a^\dagger \right) + \sigma_{ge} \left(M_{ge}\hat{\mathbf{e}}_x a + M_{ge}\hat{\mathbf{e}}_x a^\dagger \right) \right)$$

$$= \hbar g \left(\sigma_{eg} + \sigma_{ge} \right) \left(a + a^\dagger \right) = \hbar g \left(\sigma_- + \sigma_+ \right) \left(a + a^\dagger \right)$$

$$\approx \hbar g \left(\sigma_+ a + \sigma_- a^\dagger \right). \qquad (3.19)$$

Here, the transition operators are identified with the Pauli spin raising and lowering matrices $\sigma_{\pm} = \sigma_{x} \pm i\sigma_{y}$. In the last step of Eq. (3.19) the rotating wave approximation (RWA) is employed [90]. The RWA neglects terms which create or annihilate simultaneous excitations in the spin and the harmonic oscillator. These terms become relevant for the interaction energy for a very strong coupling, which is denoted as the ultra strong coupling regime ($g \approx \omega_{r}$) [92]. For the case of the coupling between a single spin and a single photon, g is typically small. To estimate g, the matrix transition element for a linear polarized B_{l} field needs to be evaluated,

$$
\begin{aligned}
M_{eg}\hat{\mathbf{e}}_{x} &= \frac{g_{eP}\mu_{B}}{\hbar}\langle e|\,\mathbf{S}\,|g\rangle\,\hat{\mathbf{e}}_{x} = \frac{g_{eP}\mu_{B}}{\hbar}\langle e|\,S_{x}\,|g\rangle \\
&= \frac{g_{eP}\mu_{B}}{2\hbar}\left(\langle e|\,S_{+}\,|g\rangle + \langle e|\,S_{-}\,|g\rangle\right) = \frac{g_{eP}\mu_{B}}{2} = M_{ge}\hat{\mathbf{e}}_{x},
\end{aligned} \tag{3.20}
$$

where the eigenvalues for the spin rasing and lowering operator are given by $S_{\pm}\,|m_{k}\rangle = \hbar\sqrt{s\,(s+1) - m_{k}\,(m_{k} \pm 1)}\,|m_{k} \pm 1\rangle,\ k = e,g$. Together with an estimate of the mode volume of the CPWR $V_{m} \approx l \cdot s^{2} = 3.3 \times 10^{-12}\,\mathrm{m}^{3}$ [9], the coupling rate for the CPWR to a single spin is

$$
\frac{g}{2\pi} = \frac{1}{2\pi}\frac{g_{eP}\mu_{B}}{2}\sqrt{\frac{\mu_{0}\hbar\omega_{r}}{2V_{m}}} \approx 11.1\,\mathrm{Hz}. \tag{3.21}
$$

Thus, g is much smaller than ω_{r}, and the RWA is suitable to apply. Finally, the full Jaynes Cummings Hamiltonian in dipole approximation and RWA, for a linear polarized microwave field writes

$$
H_{JC} = \hbar\omega_{r}a^{\dagger}a + \frac{\hbar\omega_{s}}{2}\sigma_{z} + \hbar g\left(\sigma_{+}a + \sigma_{-}a^{\dagger}\right). \tag{3.22}
$$

To ensure a lossless transfer of the excitation between the microwave field and the spin, the coupling rate needs to be much larger than their individual loss rates κ_{0} and γ (as defined in Sec. 2.1.1 and 2.2, respectively). Here, the typical experimentally obtained loss rates range from the kHz to the MHz regime (cf. Sec. 3.1.3), several orders of magnitude larger than the estimated g. Therefore, an excitation, be it either in the field or the spin, would most probably decay in one of their individual loss channels, rather than being exchanged between the two systems. This limits the application of a single spin for quantum information processing or for quantum storage. However, this limitation can be overcome by not only using a single spin, but instead a whole ensemble of spins, utilizing collective effects.

3.2.2   Tavis-Cummings Model

Originally, R. H. Dicke pointed out, that for an ensemble of emitters, interacting via a common classical radiation field, collective effects have a significant influence on the relaxation behavior of the emitters [93]. The emitters are assumed to have an inter-particle distance, which is small compared to the radiation field wavelength, but large compared to their particle wavelength. Thus, dipole-dipole interactions within the ensemble are negligible and the only interaction is mediated by the common radiation field. Dependent on the initial state of the ensemble, the relaxation can be enhanced (superradiant) or suppressed (subradiant). Collective effects can also enhance the coupling of an ensemble of emitters to an radiation field. The Tavis-Cummings model expands the so-called Dicke

model to describe the collective interaction of an ensemble of two-level systems with a single quantized field mode [94, 95]. Here, the ensemble of two-level systems consists of the ensemble of phosphorus donor electron spins and the field mode is provided by the microwave resonator.

To describe the ensemble of spins collective operators are introduced, describing its energy states, the so-called Dicke states [96]. These operators have the same properties as the spin operator **S** of the previous section and are defined as

$$\mathbf{S} = \begin{pmatrix} S_{\mathrm{x}} \\ S_{\mathrm{y}} \\ S_{\mathrm{z}} \end{pmatrix}, \qquad S_{\mathrm{x,y,z}} = \frac{\hbar}{2} \sum_{i=1}^{N} \sigma_{\mathrm{x,y,z}}^{i} \tag{3.23}$$

$$S_{\pm} = S_{\mathrm{x}} \pm i S_{\mathrm{y}} = \frac{\hbar}{2} \sum_{i=1}^{N} \sigma_{\pm}^{i}. \tag{3.24}$$

The eigenvalues, or Dicke states, are given by

$$\mathbf{S}^2 \left| J, M \right\rangle = J \left(J + 1 \right) \left| J, M \right\rangle \tag{3.25}$$

$$\text{and } S_{\mathrm{z}} \left| J, M \right\rangle = M \left| J, M \right\rangle, \tag{3.26}$$

with the quantum numbers $J = 0 \ldots \frac{N}{2}$ and $M = -J \ldots J$, where N represents the number of spins in the ensemble. J is known as the cooperation number, corresponding to the state of the ensemble. For example, in the case of two spins, $J = 0$ represents the singlet state and $J = 1$ the triplet state. The quantum number M gives the energy state of the ensemble and characterizes the polarization of the spin ensemble. Thus, for $M = -J$ all spins are in the ground state $\left| g \right\rangle$ and for $M = +J$ all spins are in the excited state $\left| e \right\rangle$. The different energy states M are generated by applying the collective spin raising and lowering operator, defined as

$$S_{\pm} \left| J, M \right\rangle = \sqrt{\left(J \pm M + 1 \right) \left(J \mp M \right)} \left| J, M \pm 1 \right\rangle. \tag{3.27}$$

With the collective operators the Tavis-Cummings Hamiltonian writes

$$H_{\mathrm{TC}} = \hbar \omega_{\mathrm{r}} a^{\dagger} a + \frac{\hbar \omega_{\mathrm{s}}}{2} S_{\mathrm{z}} + \hbar \sum_{i=1}^{N} g_i \left(\sigma_{+}^{i} a + \sigma_{-}^{i} a^{\dagger} \right), \tag{3.28}$$

assuming identical spins, with each having the same transition frequency ($\omega_i = \omega_{\mathrm{s}}$). Here, the finite linewidth of the spin transition is neglected for the moment, but is considered in the discussion of the dynamical behavior of the coupled system (cf. Sec. 3.2.3, 3.2.4).

For the coupled system the individual quantum numbers, like the photon number n of the resonator and the collective spin energy state M, are no longer good quantum numbers. Therefore, the operators $a^{\dagger} a$ and S_{z} do not commute with H_{TC}. Instead, the number of excitations $n_{\mathrm{ex}} = n + \left(M + \frac{N}{2} \right)$ is conserved and $\left(a^{\dagger} a + S_{\mathrm{z}} \right)$ commutes with H_{TC}. The energy eigenstates of the coupled system can be described by product states of Dicke states of the spin ensemble and of resonator Fock states and are defined by n_{ex}, J and either n or M ($\left| n_{\mathrm{ex}}, J, n \right\rangle$ or $\left| n_{\mathrm{ex}}, J, M \right\rangle$).

By considering the spin ensemble in a state with a high cooperation number J, the situation can be further simplified [36]. Therefore, the spin ensemble needs to be highly

polarized, which is the case at low temperatures (cf. Sec. 3.3.4). In this state, the theoretical description of the spin system is similar to the description of an ensemble of oscillators, allowing the application of the Holstein-Primakoff approximation [97]. Thus, the single spin operators can be mapped to bosonic operators [98],

$$\sigma_{\mathrm{z}}^i \equiv b_i^\dagger b_i - \frac{1}{2}, \tag{3.29}$$

$$\sigma_+^i \equiv b_i^\dagger \sqrt{1 - b_i^\dagger b_i}, \quad \sigma_-^i \equiv \sqrt{1 - b_i^\dagger b_i}\; b_i. \tag{3.30}$$

The bosonic operators $b_i^\dagger$ and b_i create and annihilate a spin excitation, having the same properties as the ladder operators for a harmonic oscillator, but with the corresponding Fock space limited by the number of spins N. The square root term in Eq. (3.30) maintains the two-level system characteristic, ensuring that only one excitation per spin is possible [36]. Additionally restricting the number of excitations to $n_{\mathrm{ex}} \leq 1$ and assuming $J = \frac{N}{2}$, two collective spin states for identical spins can be defined to

$$|0\rangle = |J, -J\rangle = |g_1, g_2, \ldots, g_N\rangle \text{ and} \tag{3.31}$$

$$|1\rangle = |J, -J+1\rangle = \frac{1}{\sqrt{N}} \left(|e_1, g_2, \ldots, g_N\rangle + \cdots + |g_1, \ldots, g_{N-1}, e_N\rangle \right). \tag{3.32}$$

The excited collective spin state describes a single spin excitation, delocalized over the whole ensemble, where the probability of exciting a specific spin is proportional to $\frac{1}{\sqrt{N}}$. Thus, the probability to find a specific excited spin $b_i^\dagger b_i$ is inversely proportional to N. Typically, the number of spins contained in a magnetic solid is much larger than the number of excitations ($N \gg n_{\mathrm{ex}}$), allowing to neglect the square root factor in Eq. (3.30) [36]. This yields for the Tavis-Cummings Hamiltonian

$$H_{\mathrm{TC}} = \hbar\omega_{\mathrm{r}} a^\dagger a + \hbar\omega_{\mathrm{s}} \sum_{i=1}^N b_i^\dagger b_i + \hbar g_{\mathrm{eff}} \left(b^\dagger a + b a^\dagger \right), \tag{3.33}$$

with the constant energy term for the spin ensemble neglected. The operator $b^\dagger = \frac{1}{g_{\mathrm{eff}}} \sum_{i=1}^N g_i b_i^\dagger$ describes the creation of a collective spin excitation and b its annihilation. The collective coupling strength g_{eff} is defined to $\sqrt{\sum_{i=1}^N |g_i|}$ and normalizes the creation and annihilation operators. In the case of identical couplings ($g_i = g$), g_{eff} is given by the single photon single spin coupling strength g, enhanced by $\sqrt{N}$. Therefore, the collective coupling strength can exceed the individual loss rates of the microwave field and the spin ensemble, by increasing the number of (polarized) spins interacting with the microwave field. On this way, a coherent exchange of excitations can be realized.

3.2.3 Eigenstates of the Tavis-Cummings Model

For the case of a single excitation, the Tavis-Cummings Hamiltonian given in Eq. (3.33) can be expressed by a 2×2 matrix [23]

$$H_{\mathrm{TC}} = \hbar \begin{pmatrix} \omega_{\mathrm{s}} & g_{\mathrm{eff}} \\ g_{\mathrm{eff}} & \omega_{\mathrm{r}} \end{pmatrix}. \tag{3.34}$$

On the diagonal are the eigenenergies of the uncoupled resonator and spin system, which are coupled by the off diagonal elements. It is possible to introduce losses by a generalized
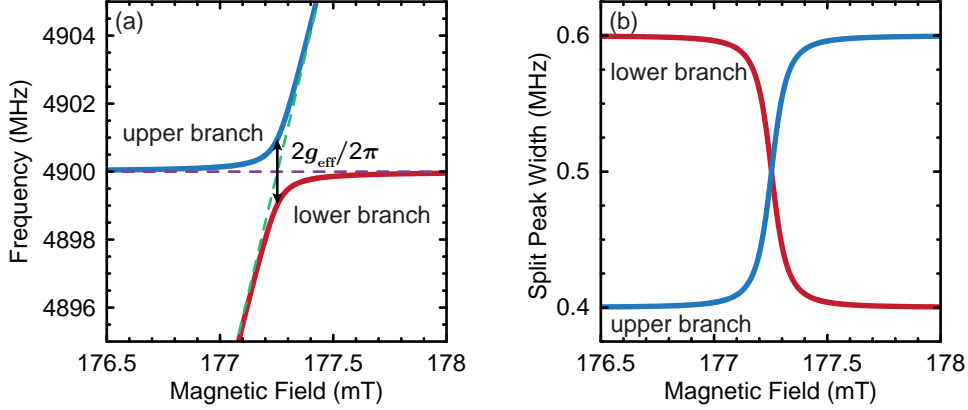
Figure 3.8: The eigenvalues $E_{u/l}/h$ as a function of static magnetic field, using $\omega_r/2\pi = 4.9\,\text{MHz}$, $\kappa_0/2\pi = 400\,\text{kHz}$, $\gamma/2\pi = 600\,\text{kHz}$ and $g_{\text{eff}}/2\pi = 1\,\text{MHz}$. For the spin transition resonance frequency $\omega_s/2\pi$, respectively resonance field, the solution from the spin Hamiltonian (2.10) in Sec. 2.2 for the high field spin transition is chosen. (a) Real part of $E_{u/l}/h$, which corresponds to the eigenfrequencies of the coupled hybrid system (solid blue and red lines), which are split by $2g_{\text{eff}}/2\pi$. Additionally, the uncoupled microwave resonator (violet dashed line) and spin ensemble (green dashed line) dispersions are shown. (b) Absolute value of the imaginary part of $E_{u/l}/h$, describing the evolution of the loss rates for the upper branch (blue) and the lower branch (red) of the avoided crossing.

Hamiltonian $H_{\text{TC,eff}}$, where the resonator and spin ensemble resonance frequencies become complex quantities [35, 99]

$$\omega_r \mapsto \tilde{\omega}_r = \omega_r - i\kappa_0, \qquad \omega_s \mapsto \tilde{\omega}_s = \omega_s - i\gamma, \tag{3.35}$$

where the loss rates are treated as imaginary contributions to the real resonance frequencies. Note, that this is a simplified approach of introducing losses to the coupled system. Typically losses are incorporated via a master equation approach in the density matrix formalism [73, 96, 99]. The relaxation is modeled by an additional operator, describing the interaction of the system with the environment. However, the simplified approach allows for a clear discussion of the evolution of the parameters of the two subsystems, when they are tuned in resonance.

The eigenvalues of Eq. (3.34), with consideration of the complex resonance frequencies, describe the complex eigenenergies, respectively the eigenfrequencies of the coupled system and are determined to

$$E_{u/l} = \frac{\hbar}{2}\left(\tilde{\omega}_r + \tilde{\omega}_s \pm \sqrt{(\tilde{\omega}_r - \tilde{\omega}_s)^2 + 4g_{\text{eff}}^2}\right). \tag{3.36}$$

Figure 3.8 plots $E_{u/l}/h$ as a function of the static magnetic field, for characteristic parameters of the microwave resonator and the spin ensemble (see legend). In Fig. 3.8 (a) the real part of Eq. (3.36) in frequency units is shown, which corresponds to the eigenfrequencies of the coupled system. In addition, the resonance frequencies of the two uncoupled subsystems are shown as dashed lines. At the degeneracy point, where both systems are in resonance, the coupled system lifts this degeneracy by splitting the resonant modes into two hybrid modes, corresponding to the microwave resonator / spin ensemble dressed states. Hereby, $\Re(E_u)$ describes the upper branch of the two hybrid modes and $\Re(E_l)$ the lower branch of the so-called avoided crossing. The splitting at the degeneracy point is

given by $2g_{\mathrm{eff}}$, the rate at which the excitation is exchanged between the two subsystems. The more the two subsystems get detuned from the degenerated interaction point, the more the systems regain their individual character until they are completely uncoupled for large detunings.

Figure 3.8 (b) plots the absolute value of the imaginary part of the eigenvalues $E_{\mathrm{u}/_{\mathrm{l}}}/h$, describing the loss rate evolution of the upper and lower branches of the avoided crossing. For a large detuning from the interaction point, the loss rates of the two branches correspond to the loss rates of the uncoupled microwave resonator and spin ensemble systems κ_0 and γ, respectively. Close to the interaction point, the loss rates converge and finally coincide when both systems are tuned in resonance. At this point, both hybrid modes exhibit a half width at half maximum of $\frac{\kappa_0+\gamma}{2}$, the average of the individual loss rates. Note, that the loss rate of the coupled system depends on the coupling-density profile, which is the convolution of the distribution of g_i to each spin in the ensemble and the spectral distribution of the spin ensemble itself [19, 35, 36]. Dependent on the spectral distribution of the coupling-density profile, the linewidth of the hybrid modes can differ from the average of the individual loss rates and instead be a function of the collective coupling strength g_{eff}.

3.2.4 Steady State Resonator Transmission Spectrum

To experimentally study the coupling between an ensemble of spins and a microwave resonator, the microwave transmission through the resonator is detected. For a theoretical description the transmission signal can be modeled by solving the corresponding master equation of the system [96, 100] or by solving the Heisenberg equations for the resonator and spin ensemble operators [35, 91, 101]. Here, the latter approach shall be discussed. The Heisenberg equations for the photon and the collective spin operators are given by

$$\dot{a} = \frac{i}{\hbar}\left[H_{\mathrm{TC}}, a\right] + \left[H_{\mathrm{drive}}, a\right] + \kappa_0 a, \tag{3.37}$$

$$\dot{b} = \frac{i}{\hbar}\left[H_{\mathrm{TC}}, b\right] + \gamma b. \tag{3.38}$$

In Eq. (3.37) a weak driving field is additionally considered, representing the measurement on the microwave resonator. The drive is characterized by its frequency ω and amplitude η, where the amplitude factor incorporates the external coupling rate into the resonator. It is useful to represent the Hamiltonians in a frame, rotating with the drive frequency ω, which yields [19, 101]

$$H'_{\mathrm{TC}} = \hbar\Delta_{\mathrm{r}} a^{\dagger} a + \hbar\Delta_{\mathrm{s}} \sum_{i=1}^{N} b_i^{\dagger} b_i + \hbar g_{\mathrm{eff}}\left(b^{\dagger} a + b a^{\dagger}\right), \tag{3.39}$$

$$H'_{\mathrm{drive}} = -i\hbar\eta\left(a - a^{\dagger}\right). \tag{3.40}$$

Thereby H'_{TC} explicitly depends on the drive frequency via $\Delta_{\mathrm{r}} = \omega_{\mathrm{r}} - \omega$ and $\Delta_{\mathrm{s}} = \omega_{\mathrm{s}} - \omega$, the detuning of the drive frequency to the microwave resonance frequency and the spin ensemble transition frequency, respectively. Thus, in the rotating frame Eq. (3.37) and (3.38) result in two coupled linear differential equations

$$\dot{a} = -\left(i\Delta_{\mathrm{r}} + \kappa_0\right)a - ig_{\mathrm{eff}} b + \eta, \tag{3.41}$$

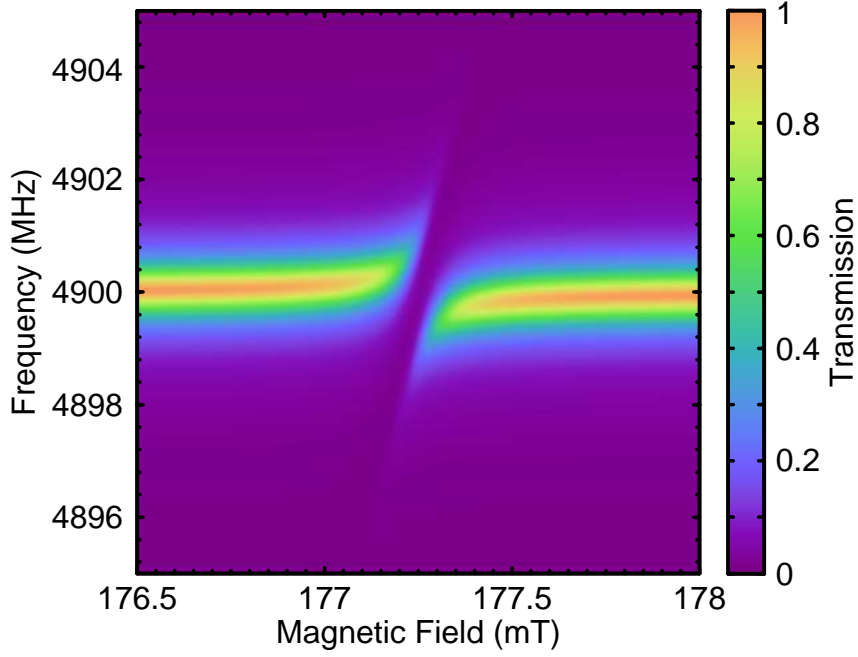$$\dot{b} = -\left(i\Delta_{\mathrm{s}} + \gamma\right)b - ig_{\mathrm{eff}} a, \tag{3.42}$$

Figure 3.9: Color coded normalized power transmission $|S_{21}|^2$ as a function of frequency and static magnetic field, using $\omega_r/2\pi = 4.9\,\text{MHz}$, $\kappa_0/2\pi = 400\,\text{kHz}$, $\gamma/2\pi = 600\,\text{kHz}$ and $g_{\text{eff}}/2\pi = 1\,\text{MHz}$. For the spin transition resonance frequency $\omega_s/2\pi$, the solution from the spin Hamiltonian (2.10) in Sec. 2.2 for the high field spin transition is chosen.

describing the dynamical behavior of the microwave resonator and the spin ensemble, coupled to each other by the collective coupling strength g_{eff}. For a continuous drive, the coupled equations are solved in the steady state ($\dot{a} = 0$ and $\dot{b} = 0$) and yield for the photon annihilation operator

$$a = \frac{\eta}{i\Delta_r + \kappa_0 + \frac{g_{\text{eff}}^2}{i\Delta_s + \gamma}} \qquad (3.43)$$

Finally, the power transmission $|S_{21}|^2$ is obtained by determining the average photon number of the microwave resonator [19, 91]

$$|S_{21}|^2 = \left\langle a^\dagger a \right\rangle = \left(\frac{\eta}{\kappa_0}\right)^2 \left| \frac{\kappa_0}{i\Delta_r + \kappa_0 + \frac{g_{\text{eff}}^2}{i\Delta_s + \gamma}} \right|^2. \qquad (3.44)$$

While the microwave resonator is decoupled from the spin ensemble, the prefactor $\left(\frac{\eta}{\kappa_0}\right)^2$ gives the peak transmission, which corresponds to the average number of photons in the resonator [91]. The transmission is a function of the drive frequency and in addition the spin transition frequency can be tuned by the static magnetic field, spanning a two-dimensional variable space. Figure 3.9 depicts a normalized simulation of the interaction of a transmission resonator at 4.9 GHz with the high field spin transition of phosphorus donors in silicon (see Sec. 2.2), using Eq. (3.44). The horizontal red line represents the resonator mode, which is interrupted at a static magnetic field of 177.25 mT. At this point, the resonator and the spin ensemble are in resonance with their resonance frequencies degenerated. To lift this degeneracy the two systems hybridize, spectroscopically resulting in an avoided crossing of the resonator mode. At the degeneracy point the separation of the two hybrid modes is given by $2g_{\text{eff}}$.
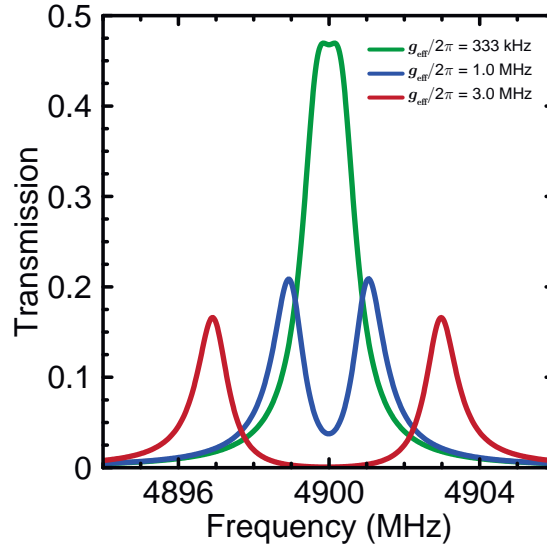
Figure 3.10: Simulated, normalized power transmission $|S_{21}|^2$ as a function of frequency for a fixed static magnetic field chosen such, that microwave resonator and spin ensemble are in resonance. For the three spectra $\kappa_0/2\pi = 400\,\text{kHz}$ and $\gamma/2\pi = 600\,\text{kHz}$, while they differ in the values for the collective coupling strength g_{eff}. The spectra illustrate three coupling regimes: Weak coupling regime (green line), the regime of high cooperativity (blue line, also corresponds to a cut in Fig. 3.9 at $B_0 = 177.25\,\text{mT}$) and the strong coupling regime (red line).

In Figure 3.10 the normalized transmission $|S_{21}|^2$ is ploted as a function of frequency for a fixed magnetic field $B_0 = 177.25\,\text{mT}$, corresponding to the center of the avoided crossing in Fig. 3.9. For comparison, three different spectra are shown, differing in the collectiv coupling strength. For a coupled system consisting of a spin ensemble and a microwave resonator, three (partly overlapping) coupling regimes can be distinguished [3]. The dimensionless cooperativity

$$C = \frac{g_{\text{eff}}^2}{\kappa_0 \gamma}, \tag{3.45}$$

allows a discrimination of the three regimes. (i) The weak coupling regime where $C < 1$ (green line in Fig. 3.10): Here, the collective coupling rate g_{eff} between the microwave resonator and the spin ensemble is smaller than their individual loss rates κ_0 and γ, respectively. The resonator transmission spectrum shows a single peak, which height is reduced compared to the uncoupled resonator transmission, since part of the energy stored in the resonant mode is absorbed by the spin ensemble. (ii) The regime of high cooperativity with the cooperativity $C > 1$ (blue line in Fig. 3.10): Here, the interaction rate g_{eff} causes a level repulsion of the eigenstates of the spin ensemble and the microwave cavity to an extend that a double peak becomes spectroscopically visible. The two peaks have a finite overlap, as g_{eff} is in the same order of magnitude as the loss rates of the coupled subsystems. (iii) The strong coupling regime with $C \gg 1$ (red line in Fig. 3.10): Here, the coupling rate g_{eff} exceeds both individual loss rates κ_0 and γ, completely separating the two peaks of the hybrid system. With the rate of excitation exchange g_{eff} being faster than the loss rates, a coherent exchange of (quantum) excitations between the subsystems is possible [102].

3.3   Coupling phosphorus donors to a CPWR

In the following, the interaction of a superconducting niobium coplanar waveguide resonator with an ensemble of phosphorus donors in an isotopically enriched ^{28}Si host is investigated [3]. The experiments are conducted in the cryogen free dilution refrigerator setup (cf. Sec. 2.3.1) with the loaded CPWR sample described in Sec. 2.3.3. At the lowest temperature used, the coupling rate g_{eff} between the microwave resonator and the electron spin ensemble is determined and it is found that it is of similar size as the spin ensembles dephasing rate γ, indicating a regime of high cooperativity. Furthermore, the coupling rate between the CPWR and the phosphorus spins as a function of temperature up to 3.5 K is investigated and is quantitatively describe in terms of the thermal spin polarization $P(T)$. The discussion on the results follows closely the argumentation presented in Ref. [3].

3.3.1   Spectroscopic Characterization

Figure 3.11 (a) shows the microwave transmission spectroscopy data of the coupled spin ensemble / microwave resonator system as a function of the magnetic field for a temperature of $T = 50$ mK. The spectrum is recorded using a microwave power of -134 dBm or 40 aW at the input of the resonator. This power corresponds to an average of 17 photons present in the microwave resonator when applied on the microwave resonator frequency. The spectrum shows the characteristic high transmission of the microwave resonator at its first harmonic with $\omega_{\mathrm{r}}/2\pi = 4.931$ GHz. Additionally, a reduction of the microwave transmission $|S_{21}|^2$ through the resonator by a factor of ten at the magnetic fields $B_{0,\mathrm{LF}} = 174.27$ mT and $B_{0,\mathrm{HF}} = 178.46$ mT is observed, where the precession frequency of the spin system matches the resonance frequency of the CPWR. The field separation of those two resonances is 4.19 mT and is in very good agreement with the characteristic hyperfine splitting of phosphorus donors in silicon [68].

For a coarse analysis, the data is fit by a lorentzian function to the $|S_{21}|^2$ data for each magnetic field point. Hereby, information about the effective half width at half maximum κ of the microwave resonator is gained, as shown in Fig. 3.11 (b). The effective half width directly corresponds to the information obtained in a conventional electron spin resonance experiment [103]. Besides the two phosphorus resonances, a broad line at $B_0 = 175.5$ mT can be identified, which is compatible with the signature expected for dangling bond defects $\mathrm{P_b}$ at the $\mathrm{Si/SiO_2}$ interface at the sample surface [104]. Additionally, the central line at $B_0 = 176.3$ mT is attributed to exchange coupled $\mathrm{P_2}$ dimers [105]. Their presence is expected for the high P doping concentration of $[\mathrm{P}] = 1 \times 10^{17}$ cm^{-3} of the sample [106].

To quantify the collective coupling g_{eff} of the donor spins to the resonator photon field the resonator transmission in the field region of the two isolated phosphorus donor electron spin resonances is investigated. Figure 3.11 (c) shows the microwave transmission $|S_{21}|^2$ for the high field spin transition at $B_0 = 178.46$ mT. It is found, that the microwave response exhibits a normal mode splitting, indicative for the high cooperativity regime. The separation of the two transmission peaks corresponds to $2g_{\mathrm{eff}}$ and thus allows a direct determination of the collective coupling rate. Fitting Eq. (3.44) to the transmission data allows for a more detailed analysis of the situation (orange line in Fig. 3.11 (c)). To account for both spin transitions of phosphorus donors in silicon and the static magnetic field
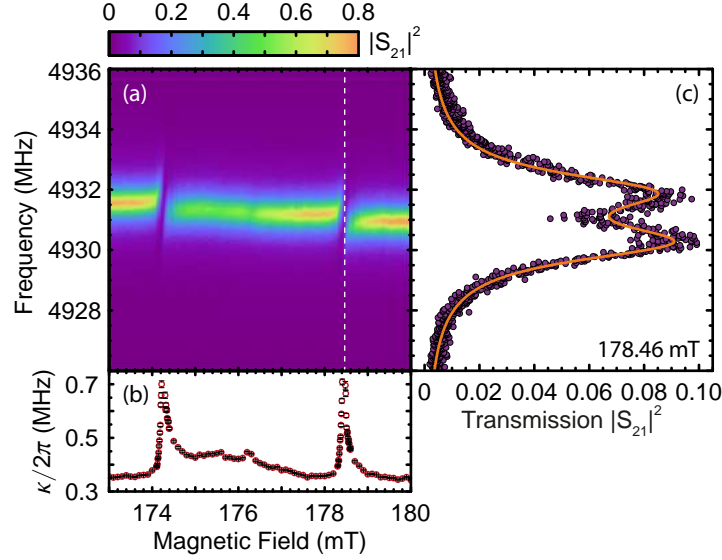
Figure 3.11: Spectroscopy data of the superconducting microwave resonator coupled to the phosphorus spin ensemble taken at a temperature of $50\,\mathrm{mK}$ and an input microwave power of $40\,\mathrm{aW}$. (a) Color coded microwave transmission data $|S_{21}|^2$ as a function of the VNA frequency and the static magnetic field B_0. The central line of high transmission indicates the resonance frequency of the CPWR. At $B_{0,\mathrm{LF}} = 174.27\,\mathrm{mT}$ and $B_{0,\mathrm{HF}} = 178.46\,\mathrm{mT}$ the resonator and the spin ensemble are in resonance resulting in a reduced transmission. These resonances are separated by $4.19\,\mathrm{mT}$, agreeing very well with the characteristic hyperfine splitting of phosphorus donors in silicon. (b) Effective linewidth (circles with error bars) of the resonator κ determined by a Lorentzian fit to the data in (a). Here, additional increases of κ are attributed to dangling bond defects P_b and P_2 dimers observed at $B_0 = 175.5\,\mathrm{mT}$ and $B_0 = 176.3\,\mathrm{mT}$, respectively. (c) Resonator transmission $|S_{21}|^2$ (circles) at $B_0 = 178.46\,\mathrm{mT}$ (white dashed line in (a)), the resonance field of the high field spin transition. The resonator mode exhibits the characteristic normal mode splitting resulting in two individual transmission peaks separated by $2g_{\mathrm{eff}}$. The solid orange line represents a fit using (3.46).

dependence, Eq. (3.44) is modified to (see Appendix A.1)

$$|S_{21}|^2 = \left| \frac{\eta}{i\left(\omega - \omega_{\mathrm{r}}\right) - \kappa_0 + \displaystyle\sum_{n=1}^{2} \frac{g_{\mathrm{eff}}^2}{i\frac{g_{\mathrm{eP}}\mu_{\mathrm{B}}}{\hbar}\left(B_0 - B_{0,\mathrm{n}}\right) - \gamma}} \right|^2 \qquad \text{with } n = \mathrm{LF}, \mathrm{HF}. \qquad (3.46)$$

The fit to the data outside the electron spin resonance yields a resonator loss rate of $\kappa_0/2\pi = 370\,\mathrm{kHz}$. Taken together with the resonator frequency of $\omega_{\mathrm{r}}/2\pi = 4.931\,\mathrm{GHz}$ this corresponds to a quality factor of $Q \approx 6600$, which is still high considering the static magnetic field of more than $170\,\mathrm{mT}$. Futhermore, the calibrated data allows to determine the external and the internal quality factor to $Q_{\mathrm{ext}} = 9793$ and $Q_{\mathrm{int}} = 20857$, respectively, indicating that the microwave resonator operates in the overcoupled regime [41]. Analyzing the data from the resonance fields $B_{0,\mathrm{LF}}$ and $B_{0,\mathrm{HF}}$, the loss rate of the spin ensemble can be determined to $\gamma/2\pi = 1.38$ and $1.40\,\mathrm{MHz}$ and the collective coupling rate is found to $g_{\mathrm{eff}}/2\pi = 1.13$ and $1.07\,\mathrm{MHz}$, respectively. Thus, the coupled system is in the high cooperativity regime for both resonances as $C = 2.5$ and 2.0, which are both > 1.

3.3.2 Modeling the Coupling

In the following, the experimentally extracted collective coupling rate g_{eff} is compared with theory. The coupling strength g_{eff} is given by the single photon single spin coupling rate g of Eq. (3.21) enhanced by the square root factor of the number of spins N [25]. Assuming an equal coupling rate for all spins

$$g_{\text{eff}} = \frac{g_{\text{eP}}\mu_{\text{B}}}{2\hbar} B_1 \sqrt{N} = \frac{g_{\text{eP}}\mu_{\text{B}}}{2} \sqrt{\frac{\mu_0 \hbar \omega_{\text{r}} N}{2V_{\text{m}}}} = \frac{g_{\text{eP}}\mu_{\text{B}}}{2\hbar} \sqrt{\frac{\mu_0 \rho \hbar \omega_{\text{r}}}{2} \frac{v_{\text{m}}}{2}}. \tag{3.47}$$

Here, the magnitude of the oscillatory magnetic field B_1 is given for spin $1/2$ and a linear polarized microwave field, as defined in Eq. (3.17) of Sec. 3.2.1. $v_{\text{m}} = \frac{V}{V_{\text{m}}}$ can be understood as the filling factor of the resonator mode volume V_{m}, filled by the phosphorus doped silicon sample of volume V and donor concentration ρ. A $g_{\text{eff}}/(2\pi) = 4.48\,\text{MHz}$ is obtained for the optimal condition that the complete upper hemisphere of the CPWR mode volume is filled, which corresponds to $v_{\text{m}} = 0.5$ and assumes a spin density $\rho = 1 \times 10^{17}\,\text{cm}^{-3}$.

Phosphorus donors in silicon show two electron spin resonance transitions due to the finite hyperfine interaction between the electron and nuclear spin of the phosphorus donor (cf. Sec. 2.2). At a temperature of $50\,\text{mK}$ the electron spins are fully polarized and the nuclear spin polarization is about $2.5\,\%$. For the specific case of phosphorus donors in silicon it can be safely approximated that each of the two hyperfine split ESR transitions contains $50\,\%$ of the total spin density ρ. Therefore, the number of transitions (2) reduces g_{eff} by an additional factor of $\sqrt{2}$ yielding $g_{\text{eff}}/(2\pi) = 3.17\,\text{MHz}$ for each individual transition. A value which is larger than the experimentally observed values of $1.07\,\text{MHz}$ and $1.13\,\text{MHz}$.

For the more realistic situation of a finite gap of width d between the ^{28}Si crystal and the coplanar microwave resonator a numerically approach to calculate g_{eff} is chosen. At first, the microwave B_1 field distribution according to Ref. [78] is simulated, where the B_1 field magnitude is again normalized to the ground state energy density of the resonator given in Eq. 3.17. This yields a position-dependent coupling strength $g(\mathbf{r}_i)$. In total, the effective coupling writes [19]

$$g_{\text{eff}} = \sqrt{\frac{1}{2}\sum_{i=1}^{N}|g(\mathbf{r}_i)|^2} = \frac{g_{\text{eP}}\mu_{\text{B}}}{2\hbar}\sqrt{\frac{1}{2}\sum_{i=1}^{N}|B_1(\mathbf{r}_i)|^2}. \tag{3.48}$$

The index i refers to each individual spin contained inside the phosphorus doped ^{28}Si crystal. The calculation is performed on a discrete lattice with lattice constant a, where at each lattice site a spin is located given by the vector $\mathbf{r}_i$. Assuming a homogeneous spin distribution in the sample, the lattice constant can be determined by the mean inter-particle distance to $26.73\,\text{nm}$ for a phosphorus donor concentration of $1 \times 10^{17}\,\text{cm}^{-3}$. The numerical B_1 field calculation is performed for the cross-section of the CPW [78], which is placed in the yz-plane with the z-coordinate being normal to the CPW surface. For the x-coordinate along the length l of the CPWR, the yz-field has a sinusoidal modulation, reflecting the shape of the first harmonic mode of the resonator,

$$g_{\text{eff}} = \frac{g_{\text{eP}}\mu_{\text{B}}}{2\hbar}\sqrt{\frac{1}{2}\sum_{i=1}^{N}|B_1(\mathbf{r}_i)|^2} = \frac{g_{\text{eP}}\mu_{\text{B}}}{2\hbar}\sqrt{\frac{1}{2}\sum_{i=1}^{N}\left[(B_{\text{y},i}^2 + B_{\text{z},i}^2)\left|\sin\left(\frac{2\pi l}{x_i}\right)\right|^2 F\right]}. \tag{3.49}$$

For electron spin resonance the oscillatory magnetic field B_1 needs to be perpendicular to the static magnetic field B_0. This condition cannot be fulfilled on the whole length l of the resonator (cf. Fig. 2.2). Thus, for the calculation only the parts of the resonator where B_1 is perpendicular to B_0 are considered, corresponding to locations where the center line of the CPWR is aligned in parallel with the static magnetic field B_0 (cf. Fig. 2.11 (a)), which is accounted for by the piecewise defined function

$$F = \begin{cases} 1 & \text{if CPW } \| \ B_0 \\ 0 & \text{else} \end{cases} . \tag{3.50}$$

For a gap of width of $d = 12.5\,\mu\text{m}$ we obtain $g_{\text{eff}}/(2\pi) = 1.10\,\text{MHz}$, which is in good agreement with the experimentally determined values. The corresponding gap is attributed to the absence of special CPWR and ^{28}Si crystal cleaning procedures prior to mounting the spin ensemble.

3.3.3   Spin Loss Rate Discussion

The extracted spin ensemble loss rate γ translates with Eq. (2.17) to a magnetic full width at half maximum (FWHM) linewidth of $\Delta B = 98.52$ and $99.80\,\mu\text{T}$ for the low and high field resonance, respectively. For phosphorus donors in isotopically purified ^{28}Si a reduced linewidth compared to ^{nat}Si is expected [4, 107, 108]. Figure 3.12 (a) shows the dependence of the ESR linewidth on the ^{29}Si concentration of a silicon crystal as reported in Ref. [70]. According to Abe *et al* (Ref. [70]), the linewidth increases linearly with the residual ^{29}Si concentration f, for $f < 0.05$. For larger concentrations, the linewidth follows a $f^{0.5}$ dependence. The additional broadening is caused by the fluctuating non-zero nuclear moment of the ^{29}Si, interacting with the phosphorus donor spin. Hereby, the Larmor frequency of each individual phosphorus donor becomes slightly offset, depending on the exact location and spin state of the ^{29}Si nuclear spin , resulting in a linewidth broadening. The Zeeman splitting of the ^{29}Si nuclear moments is in the MHz-regime. The corresponding temperature of this splitting lies in the sub mK-regime, a regime not accessible in the here presented experiments. Thus, a contribution of the fluctuating ^{29}Si moments cannot be suppressed at the temperatures employed in this thesis, but can be limited by isotopically purification.

The residual ^{29}Si concentration f of the investigated phosphorus doped ^{28}Si crystal is 0.001, which corresponds to an expected magnetic FWHM linewidth of $6\,\mu\text{T}$ (see green line in Fig. 3.12 (a)) [70], more than a factor of 10 smaller than the extracted linewidth of $\Delta B = 98.52$ and $99.80\,\mu\text{T}$, obtained from the data shown in Fig. 3.11. This discrepancy is attributed to inhomogeneities in the static magnetic field B_0 provided by the superconducting magnet. The specified inhomogeneity of the superconducting magnet is $0.01\,\%$ over 10 mm, relative to the most homogeneous point of the magnet. For an estimation, the silicon crystal's dimension on top of the CPWR is assumed to be $4 \times 4\text{mm}^2$ (cf. Fig. 2.11 (a)). This would correspond to an absolute field inhomogeneity of $70\,\mu\text{T}$ at 176 mT, applied along the axis of the magnet. However, a misalignment of the sample by only 1 mm from the optimal field position, would increase the inhomogeneity by $0.002\,\%$ and the absolute field inhomogeneity to $105\,\mu\text{T}$. This is verified by reference experiments with similar prepared crystals (cf. Sec. 2.2.2) in a commercial Bruker electron spin resonance spectrometer performed at a temperature of 8 K, yielding a linewidth of $\Delta B_{\text{Bruker}} = 37.7\,\mu\text{T}$ (see
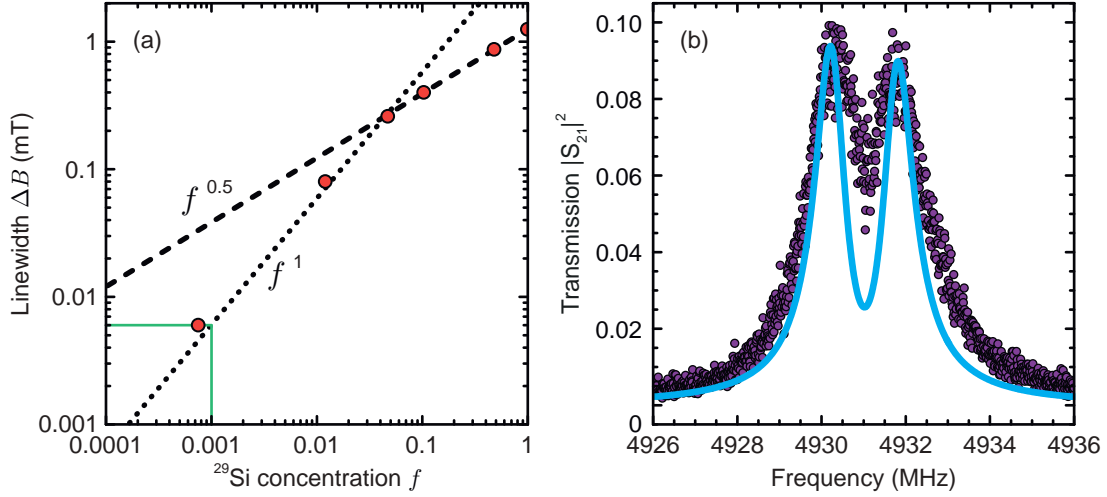
Figure 3.12: (a) ESR magnetic FWHM ΔB as a function of the residual ^{29}Si concentration f of a silicon crystal (taken from Ref. [70]). The green line indicates the ^{29}Si concentration of the used silicon crystal and the corresponding expected linewidth. (b) Resonator transmission $|S_{21}|^2$ (circles) at $B_0 = 178.46\,\mathrm{mT}$ (white dashed line in Fig. 3.11 (a)). The solid blue line represents a simulation of the transmission using the parameters obtained in Sec. 3.3.1, except that γ_{Bruker} instead of γ is used.

Sec. 4.3.2).

The extracted magnetic field linewidth corresponds to a $\gamma_{\mathrm{Bruker}}/2\pi = 530\,\mathrm{kHz}$ indicating that the observed γ in the millikelvin experiments, due to an not sufficiently homogeneous static magnetic field B_0. Therefore, considering γ_{Bruker} instead of γ places the coupled system in the strong coupling regime and correspondingly results in a cooperativity of $C = 6.5$ and 5.8 for both electron spin resonances. Furthermore, Figure 3.12 (b) compares the microwave transmission $|S_{21}|^2$ for the high field spin transition at $B_0 = 178.46\,\mathrm{mT}$ (circles), with a simulation using the extracted parameters from Sec. 3.3.1, except that the spin loss rate γ_{Bruker} is used (solid line). The two peaks are spectroscopically well separated, indicating the regime of strong coupling. Thus, the investigated phosphorus spin ensemble in the ^{28}Si host material is well in the strong coupling regime, if the limitation due to the magnetic field inhomogeneities of the superconducting magnet are reduced to by one order of magnitude. One approach would be to reduce the area taken by the sample within the static magnetic field. This reduces the effect of the field inhomogeneity and consequently the broadening of the spin resonance lines, which is also demonstrated by using the much smaller LER design in Sec. 3.4.

3.3.4   Temperature Dependence of g_{eff}

Next, the collective coupling strength g_{eff} as a function of temperature up to $3.5\,\mathrm{K}$ for both the low field and high field resonance are investigated, as shown in Fig. 3.13 (a). For each temperature, the collective coupling is determined as described in Sec. 3.3.1, using Eq. (3.46). With increasing temperature the coupling strength reduces from its maximum at $50\,\mathrm{mK}$. For temperatures above $100\,\mathrm{mK}$ the coupling to both resonances follows the same temperature dependence. Below $100\,\mathrm{mK}$ a finite difference in the coupling strength of the two resonances is observed, with the low field resonance having the higher g_{eff}. This behavior is understood as $g_{\mathrm{eff}} = g\sqrt{NP(T)}$ scales with the thermal polarization
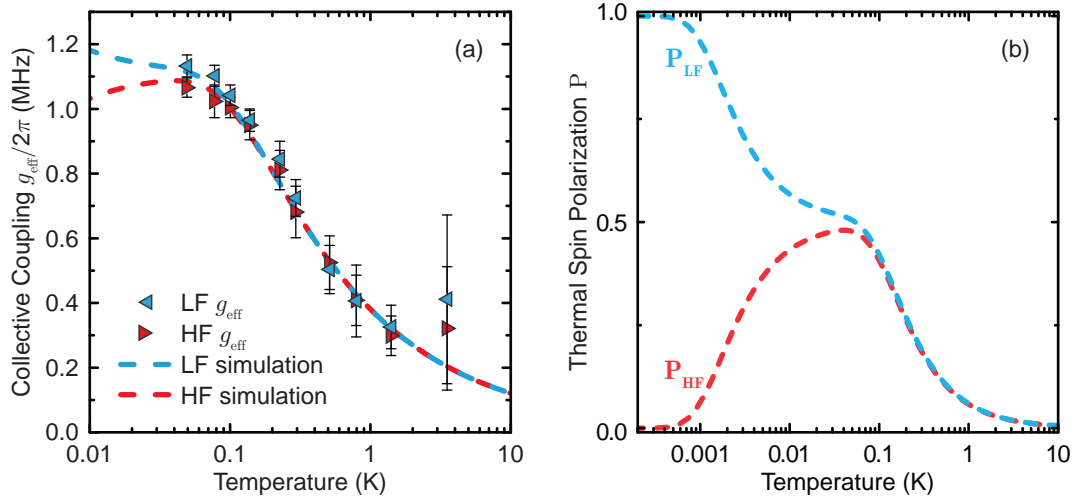
Figure 3.13: (a) Collective coupling g_{eff} as a function of logarithmic scaled temperature for both the low field (blue triangles) and high field (red triangles) spin transition. For low temperatures there is a finite difference in the coupling rates, which is attributed to the thermal nuclear spin polarization. The dependence is well described by the statistical model (dashed lines), taking all eigenenergies of the phosphorus donor ($S = 1/2$, $I = 1/2$) into account. (b) Calculated spin polarization for the two allowed electron spin resonance transitions as a function of logarithmic scaled temperature, taking into account the occupation probability of the respective transition (LF, HF).

$P(T)$ of the respective spin resonance transition [19]. $P(T)$ can be derived from the thermal population of the individual energy levels of the phosphorus donor spin system with electron spin $S = 1/2$ and nuclear spin $I = 1/2$.

The probability p_i that a given energy state E_i is occupied at a temperature T is given by [109]

$$p_i = \frac{e^{-E_i/k_{\text{B}}T}}{Z}, \qquad i = 1..4, \tag{3.51}$$

where k_{B} is the Boltzmann constant. The probability is normalized to the single particle partition function Z which is the sum of all Boltzmann factors of all available energy states E_i

$$Z = \sum_i e^{-E_i/k_{\text{B}}T}. \tag{3.52}$$

Assuming unstrained silicon the possible energy levels for phosphorus donors in silicon are given by the Hamiltonian (2.10), given in Sec. 2.2. In the limit of high fields, four distinct energy levels are present in the spin system (cf. Fig. 2.6). Using the expressions for the energy levels E_1 to E_4 of Eq. 2.16, allows to formulate the corresponding population probabilities in thermal equilibrium to

$$p_j = \frac{e^{-E_j/k_{\text{B}}T}}{\sum_{i=1..4} e^{-E_i/k_{\text{B}}T}}, \qquad j = 1..4. \tag{3.53}$$

From these the electron spin polarization $P(T, B_0)$ of the low field (LF) and the high field (HF) electron spin transitions ($E_1 \rightarrow E_4$ and $E_2 \rightarrow E_3$) can be deduced to

$$P_{\text{LF}}(T, B_0) = |p_1 - p_4| \text{ and} \tag{3.54}$$

$$P_{\text{HF}}(T, B_0) = |p_2 - p_3|, \text{ respectively.} \tag{3.55}$$

The polarization of the two electron spin resonance transitions is displayed in Figure 3.13 (b) for a fixed magnetic field of 176.5 mT, resembling the conditions of our experiment.

Our data corroborates the expected theoretical behavior as indicated by the dashed lines in Fig. 3.13 (a). Below 100 mK, the electron spin system is fully polarized and the nuclear thermal polarization gives rise to a difference in the collective coupling constants for the two spin resonance transitions. In contrast, above 100 mK, the thermal nuclear polarization is negligible and a $T^{-1/2}$ dependence for g_{eff} is found. As expected from the statistical model, the collective coupling is dominated by the thermal electron polarization of a $S = 1/2$ system, emphasizing that $g_{\text{eff}} \propto \sqrt{P(T)}$.

3.4   Coupling Phosphorus Donors to a LER

The interaction of a set of superconducting lumped element resonators with an ensemble of phosphorus donors is studied in this section. Using the LER chip described in Sec. 2.1.2, loaded with pieces of phosphorus doped ^{28}Si (cf. Sec. 2.3.3), the dependence of the coupling strength on the resonator coverage is investigated. At the base temperature of the cryogen free dilution refrigerator setup (cf. Sec. 2.3.1) low power continuous microwave spectroscopy is used to extract the relevant parameters of the hybrid system. The results are discussed and the LERs performance is compared with the of the CPWR. An unexpected asymmetry in the linewidth of the split normal mode transmission dips is observed in the experiments concerning the LER's. The origin of this asymmetry is discussed and a model is proposed for its description.

3.4.1   Spectroscopic Characterization

The loaded resonators A to C interact with the spin ensemble with different coupling strengths. The evaluation is shown exemplary for resonator B, exhibiting the largest g_{eff}. Figure 3.14 (a) shows the color coded microwave transmission $|S_{21}|^2$, coupled to the phosphorus donor spin ensemble as a function of the VNA frequency and the static magnetic field. At a temperature of 50 mK, the resonator is characterized by an asymmetric lorentzian shaped transmission reduction (cf. Sec. 3.1.2), where the power transmission is reduced by 13 dB. For $B_0 = 175$ mT, the resonance frequency is determined to $\omega_{\text{r,B}}/2\pi = 4.756$ GHz. The resonance frequency dispersion of the microwave resonator exhibits a distinct normal mode splitting at the magnetic fields $B_{0,\text{LF}} = 168.36$ mT and $B_{0,\text{HF}} = 172.54$ mT. Here, resonator and spin ensemble couple and form a hybrid system, thus they exchange energy with a rate of g_{eff}. The two avoided crossings are separated by 4.18 mT, the characteristic hyperfine splitting of the low-field (LF) and high-field (HF) electron spin transitions in phosphorus donors.

Analyzing the resonator transmission, using Eq. (3.6), allows to extract the effective HWHM κ of the coupled system, which is ploted as a function of the magnetic field in Fig. 3.14 (b). This evaluation is only valid for magnetic fields where the resonator mode shows no splitting. However, it reveals additional spectroscopic features in the field region between the two phosphorus donor electron spin transitions, since κ corresponds to the information obtained by conventional ESR experiments [103] (cf. Sec. 3.3.1). As with the CPWR experiments, a contribution of P_2 dimers centered between the low and high field transitions is observed, at $B_0 = 170.32$ mT. In contrast to the single dangling bond
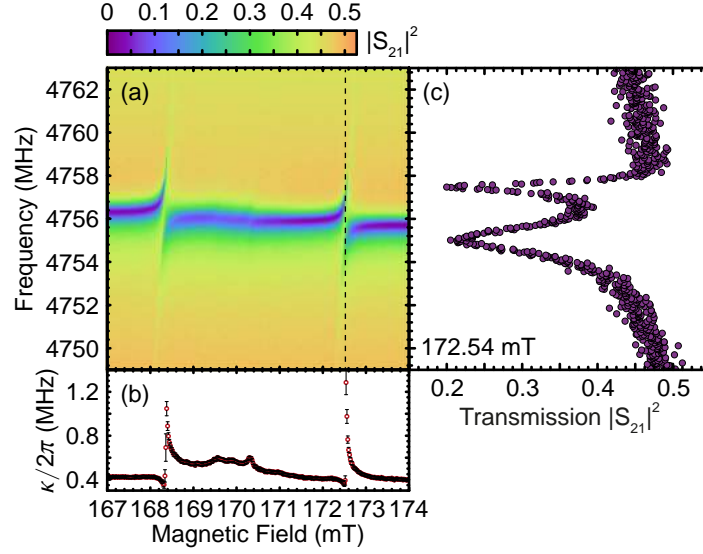
Figure 3.14: Spectroscopy data of the superconducting lumped element resonator B coupled to the phosphorus spin ensemble taken at a temperature of 50 mK and an input microwave power of 40 aW. (a) Color coded microwave transmission data $|S_{21}|^2$ as a function of the VNA frequency and the magnetic field B_0. The central line of low transmission indicates the resonance frequency of the LER. At $B_{0,LF} = 168.36$ mT and $B_{0,HF} = 172.54$ mT the resonator and the spin ensemble are in resonance resulting in an avoided crossing. These resonances are separated by 4.18 mT, the characteristic for the hyperfine splitting of phosphorus donors in silicon. (b) Effective linewidth (circles with error bars) of the resonator κ determined by the lorentzian fit (3.56) to the data in (a). Here, additional increases of κ are attributed to dangling bond defects P_{b0}, P_{b1} and P_2 dimers observed at $B_0 = 169.56$ mT, $B_0 = 169.9$ mT and $B_0 = 170.32$ mT, respectively. (c) Resonator transmission $|S_{21}|^2$ (circles) at $B_0 = 172.54$ mT (black dashed line in (a)), the resonance field of the high field spin transition. The resonator mode exhibits the characteristic normal mode splitting resulting in two individual transmission dips separated by $2g_{eff}$.

defect P_b feature found in the CPWR experiments, here two peaks can be distinguished, located at magnetic fields of 169.56 mT and 169.9 mT. These peaks can be an indication for two different Si/SiO_2 interface defects at the silicon surface, the P_{b0} and P_{b1} defects [104, 110, 111]. However, further investigations, like angle dependent ESR experiments, are needed to confirm the classification of the P_{b0} and P_{b1} defects.

Figure 3.14 (c) shows the microwave transmission $|S_{21}|$ as a function of the VNA frequency, at a magnetic field of $B_0 = 172.53$ mT (indicated by the dashed black line in Fig. 3.14 (a)). The spectrum shows two well separated transmission dips, indicating a strongly coupled resonator / spin ensemble hybrid system. However, the two dips exhibit a significant asymmetry with respect to their linewidth, which is not expected within the Tavis-Cummings model (see Sec. 3.2.3 and Sec. 3.2.4). Possible origins of the asymmetric normal mode splitting are discussed in Sec. 3.4.2.

Due to the asymmetric splitting visible in Fig. 3.14 (c), the model function given by Eq. (3.46), is not applicable to extract the relevant parameters of the coupled system. Therefore, an alternative approach for identifying the hybrid system's parameter is presented in the following.

The loss rate of the microwave resonator κ_0 is extracted from the off-resonant effective HWHM κ in Fig. 3.14 (b). At $B_0 = 167$ mT the loss rate $\kappa_0/2\pi \approx 410$ kHz, a magnetic field where resonator and spin ensemble are far detuned and can be assumed non-interacting.
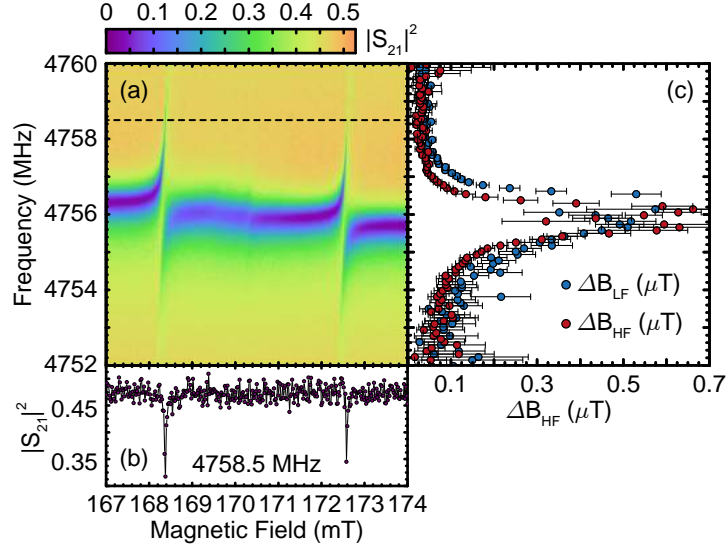
Figure 3.15: Spectroscopy data of the superconducting lumped element resonator B coupled to the phosphorus spin ensemble taken at a temperature of 50 mK and an input microwave power of 40 aW. (a) Color coded microwave transmission data $|S_{21}|^2$ as a function of the VNA frequency and the magnetic field B_0. (b) Microwave transmission $|S_{21}|^2$ as a function of B_0 for a fixed VNA frequency of 4758.5 MHz (horizontal dashed line in (a)). The two transmission dips indicate the LF and the HF spin transitions, with the spin ensemble far detuned from the microwave resonator. (c) and (d) Magnetic FWHM ΔB as a function of the VNA frequency for the LF and the HF spin transition, respectively. ΔB is determined by fitting Eq.(3.56) to the microwave transmission along the magentic field axis for a fixed frequency. Valid results are obtained only for large frequency detunings from the resonators resonance frequency.

With a resonance frequency of $\omega_{r,B}/2\pi = 4.756\,\text{GHz}$ this corresponds to a Q-factor of $Q_B = 5796$. Additionally, the fit of Eq. (3.6) to the transmission data yields an internal and external Q-factor of $Q_{int,B} = 24265$ and $Q_{ext,B} = 7636$, respectively.

The spin loss rate γ is determined using an complementary approach. Here the transmission data shown in Fig. 3.15 (a) is analyzed for a fixed frequency along the magnetic field axis. Figure 3.15 (b) shows the microwave transmission $|S_{21}|^2$ as a function of the magnetic field, at a microwave frequency of 4.7585 GHz (indicated by the horizontal dashed line in Fig. 3.15 (a)). The distinct dips correspond to the LF and HF electron spin transitions. Fitting a lorentzian transmission function to the resonance dips

$$|S_{21}|^2 = S_0^2 - A_0^2 \frac{\Delta B_n^2}{(B_0 - \Delta B_{0,n})^2 - \Delta B_n^2} \qquad \text{with } n = \text{LF, HF} \qquad (3.56)$$

results therefore in an effective magnetic FWHW field linewidth ΔB of the spin system. For frequencies far detuned from the microwave resonator we expect, analogously to the analysis of the bare linewidth of the microwave resonator, the bare linewidth of the spin ensemble. Figure 3.15 (c) shows the resulting linewidth as a function of the VNA frequency for the LF and HF spin transitions. Note, that the analysis is only valid for frequencies far detuned form the resonator frequency of $\omega_{r,B}/2\pi = 4.756\,\text{GHz}$, when the resonance lineshape resembles a lorentzian form. For frequencies larger than 4.758 GHz or lower than 4.753 GHz, the linewidth settles on a value of $\Delta B_{LF} = 37.89\,\mu\text{T} \pm 9.74\,\mu\text{T}$ and $\Delta B_{HF} = 32.66\,\mu\text{T} \pm 9.94\,\mu\text{T}$ for the LF and HF electron spin transition, respectively. The large error margins result from the limited static magnetic field resolution of the

Resonator	$\kappa_0/2\pi$ (kHz)	$\gamma_{\mathrm{LF/HF}}/2\pi$ (kHz)	$g_{\mathrm{eff,LF/HF}}/2\pi$ (MHz)	$C_{\mathrm{LF/HF}}$	Coverage
A	425	1271 / 1297	0.46 / 0.51	0.39 / 0.47	100
B	410	529.29 / 456.77	1.37 / 1.23	8.64 / 8.08	54
C	430	796.91 / 473.84	0.79 / 0.77	1.82 / 2.91	42

Table 3.4: Summary of the determined parameters of the microwave resonator / spin ensemble hybrid system, for the LERs A to C.

superconducting solenoid. However, the linewidth $B_{\mathrm{Bruker}} = 37.7\,\mu\mathrm{T}$, found from investigations on the same crystal with a commercial Bruker ESR spectrometer (see Sec. 4.3.2), resides within the error of the extracted linewidth. The magnetic FWHM translates via Eq. (2.17) to a loss rate of the spin ensemble of $\gamma_{\mathrm{LF}}/2\pi = 529.29\,\mathrm{kHz} \pm 136.22\,\mathrm{kHz}$ and $\gamma_{\mathrm{HF}}/2\pi = 456.77\,\mathrm{kHz} \pm 139.02\,\mathrm{kHz}$ for the low- and high-field spin transition, respectively. This additionally confirms that B_0 field inhomogeneities are responsible for the increased spin resonance linewidth, observed in the CPWR experiments (cf. Sec. 3.3.1). Due to the smaller area occupied by the LER in the B_0 field, it is less prone to its field inhomogeneities. The collective coupling $2g_{\mathrm{eff}}$ can be determined by the microwave resonator's normal mode splitting at the degeneracy point. At the resonance fields $B_{0,\mathrm{LF}}$ and $B_{0,\mathrm{HF}}$ the coupling rate is found to be $g_{\mathrm{eff,LF}}/2\pi = 1.37\,\mathrm{MHz}$ and $g_{\mathrm{eff,HF}}/2\pi = 1.23\,\mathrm{MHz}$. For both spin transitions g_{eff} exceeds the individual loss rates κ_0 and γ, showing that the hybrid system resides in the strong coupling regime. The corresponding cooperativities for the LF and HF spin transitions are $C_{\mathrm{LF}} = 8.64$ and $C_{\mathrm{HF}} = 8.08$, respectively.

The transmission data for the resonators A and C are analyzed equally and the results are summarized in Tab. 3.4, together with the results of resonator B. Appendix A.2 contains the transmission spectra for the resonators A and C. From the resonator's coverage, estimated from Fig. 2.11 (b), the largest collective coupling rate would have been expected for resonator A. However, resonator B exhibited the strongest coupling to the spin ensemble, with a coverage of roughly 54 %. This might be attributed to a better resonator surface / ^{28}Si crystal interface of the large central piece, covering resonators B and C (cf. Fig. 2.11 (b)). This assumption is supported by the fact, that resonator C shows the second largest coupling rate, although it is only covered by the doped silicon crystal by roughly 42 %.

In comparison to the CPWR, the LER shows an overall better performance for being coupled to the phosphorus donor spin ensemble. As the uncoupled resonator loss rate κ_0 and Q-factor are very similar for both resonator designs, the key difference is their geometrical footprint on the chip. The planar dimension of the LER is about one order of magnitude smaller than the dimension of the CPWR. Consequently, the size of the phosphorus doped ^{28}Si crystal, required to cover the LER, is also smaller. This reduces the effects of inhomogeneous broadening on the ESR linewidth, due to inhomogeneities in the static magnetic field. For the CPWR experiments the observed spin loss rate is larger than expected, preventing the microwave resonator spin ensemble hybrid system to enter the strong coupling regime. With the LER design this limitation could get resolved and allowed the realization of strong coupling.
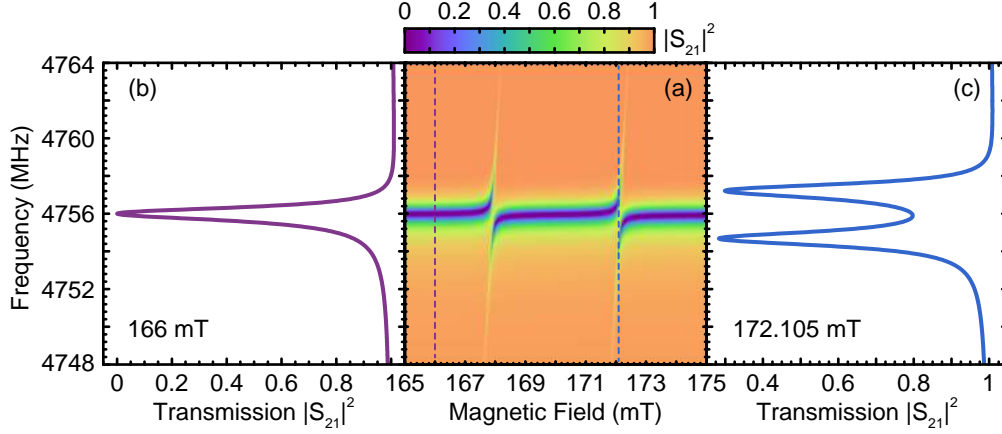
Figure 3.16: (a) Normalized simulation of the microwave transmission $|S_{21}|$ as a function of the static magnetic field and the VNA frequency, using Eq. (3.59). For the simulation $\kappa_0/2\pi = 410\,\text{kHz}$, $\gamma/2\pi = 500\,\text{kHz}$, $g_{\text{eff}}/2\pi = 1.3\,\text{MHz}$ and $\varphi = 0.1$ are used, assuming the same parameters for the LF and HF spin transitions. (b) and (c) Simulated microwave transmission as a function of the VNA frequency for fixed magnetic fields, showing the uncoupled microwave resonator (purple dashed line in Fig. 3.16 (a)) and the HF coupled resonator / spin ensemble hybrid system (blue dashed line in Fig. 3.16 (a)), respectively.

3.4.2   Asymmetric Linewidth of Normal Mode Splitting

Characteristic for the resonators B and C is that the broader dip is always located on the lower frequency side, over the full magnetic field dispersion of the avoided crossing. For resonator A this characteristic is only found for the LF spin transition and inversed for the HF spin transition. Considering the microwave transmission data of resonator B, the dip on the low frequency side is by a factor of 3.5 broader than the high frequency side dip, for both electron spin transitions. To describe the asymmetric linewidth of the two microwave transmission dips of the resonator / spin ensemble hybrid system, two different approaches are considered and discussed in the following.

(i) As the microwave transmission of all five LERs exhibits a distinct asymmetric lorentzian lineshape, it can be assumed that the microwave transmission of the coupled system also exhibits an asymmetry. To consider the LER lineshape, the drive η in Eq. 3.41 is assumed complex. This allows to describe the interference between the microwave signal on the feedline and the resonator signal by a phase φ, changing the two coupled linear differential equations for the hybrid system to,

$$\dot{a} = -\left(i\Delta_{\text{r}} + \kappa_0\right)a - ig_{\text{eff}}b + \eta e^{i\varphi}, \tag{3.57}$$

$$\dot{b} = -\left(i\Delta_{\text{s}} + \gamma\right)b - ig_{\text{eff}}a, \tag{3.58}$$

Soving the system of equations for an absorption resonator, results in the power transmission $|S_{21}|$,

$$|S_{21}|^2 = \left(\frac{\eta}{\kappa_0}\right)^2 \left| \kappa_0 - \frac{\kappa_0 e^{i\varphi}}{i\Delta_{\text{r}} + \kappa_0 + \frac{g_{\text{eff}}^2}{i\Delta_{\text{s}}+\gamma}} \right|^2. \tag{3.59}$$

Figure 3.16 (a) shows a normalized simulation of the microwave transmission $|S_{21}|^2$, using a comparable set of parameters found for resonator B (see Tab. 3.4). Assuming a phase of $\varphi = 0.1$, the simulation resembles the asymmetric lineshape of the uncoupled resonator,

as shown in Fig. 3.16 (b) (cf. Fig. 3.6). However, the microwave transmission at the two degeneracy points only show an asymmetry at the edges of the resonator's split normal mode, with a equal linewidth for the two dips (shown in Fig. 3.16 (c) for the HF spin transition). The assumption of a complex microwave drive is therefore not sufficient to describe the asymmetric linewidth distribution in the strong coupling regime. It only affects the microwave resonator's transmission and leaves the coupling between resonator and spin ensemble unchanged.

(ii) When microwave resonator and spin ensemble are not directly exchanging energy via the magnetic dipole interaction, an asymmetric linewidth of the normal mode splitting can occur [112]. In this case, the individual subsystems exchange energy via a bath of vacuum field modes, by spontaneous emission into a bath mode and subsequent reabsorption. The bath modes have arbitrary phase relations, which results in a loss of coherence of the transferred energy state. For the LER experiments, the broadband feedline could represent such a bath, able to support an infinite number of field modes, providing a way for an incoherent coupling of microwave resonator and spin ensemble.

As with the coherent coupling, the incoherent coupling is characterized by a coupling rate g_{inco}. The incoherent coupling is introduced as a complex contribution to the coupling rate g_{eff} in the Tavis-Cummings model, similar to the introduction of loss in Sec. 3.2.3. Thus, the matrix representation of $H_{TC,eff}$ changes to [112],

$$H_{TC,inco} = \hbar \begin{pmatrix} \tilde{\omega}_s & g_{eff} \\ g_{eff} & \tilde{\omega}_r \end{pmatrix} - i \begin{pmatrix} 0 & g_{inco} \\ g_{inco} & 0 \end{pmatrix}, \qquad (3.60)$$

with the corresponding energy eigenstates,

$$E_{u/l,inco} = \frac{\hbar}{2} \left(\tilde{\omega}_r + \tilde{\omega}_s \pm \sqrt{(\tilde{\omega}_r - \tilde{\omega}_s)^2 + 4 \left(g_{eff}^2 - g_{inco}^2 - 2i g_{eff} g_{inco} \right)} \right), \qquad (3.61)$$

where $\Re(E_{u/l,inco})/h$ describes the dispersion of the eigenfrequencies and $|\Im(E_{u/l,inco})/h|$ the evolution of the loss rates for the upper and lower branches of the avoided crossing. Using Eq. (3.6), the resonator transmission is fitted in the vicinity of the HF spin transition. Hereby, the fit is restricted to fit only one of the two resonance dips of the avoided crossing. This allows to extract the eigenfrequencies of the upper and lower branch. The results resemble the avoided crossing and can be very well described by $\Re(E_{u/l,inco})/h$, as shown in Fig. 3.17 (a). The incoherent coupling g_{inco} effectively reduces the coherent coupling rate g_{eff}, without changing the dispersion of the eigenfrequencies, with respect to the solutions discussed in Sec. 3.2.3. Thus, with respect to the eigenfrequencies, solely from investigating $\Re(E_{u/l,inco})$, a contribution from an incoherent interaction cannot be determined. Therefore, the linewidth of the avoided crossing branches at the HF spin transition is studied additionally, by fitting a double lorentzian function to the microwave resonator's transmission data for fixed magnetic fields. Figure 3.17 (b) plots the obtained HWHM linewidth for the upper (blue symbols) and lower (red symbols) branch as a function of the B_0 field. The analysis works best near the degeneracy point, where both transmission dips are clearly distinguishable from the background. The non constant background further complicates the analysis of the transmission dip of the spin ensemble dispersion, preventing the extraction of its linewidth far away from the degeneracy point. The linewidth of the upper branch is given by the microwave resonator's $\kappa_0/2\pi$ for fields smaller than the spin resonance field $B_{0,HF} = 172.54\,\text{mT}$. With increasing B_0 the upper branch's linewidth
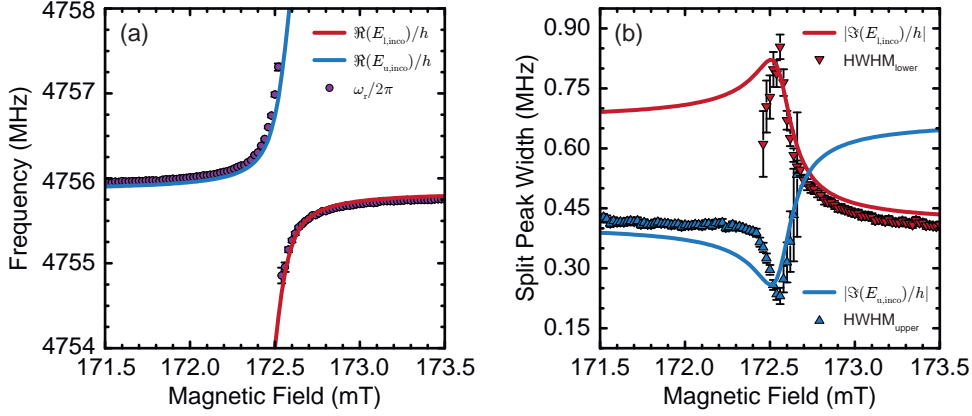
Figure 3.17: (a) Eigenfrequencies of the coupled microwave resonator / spin ensemble (symbols) at the HF spin transition as a function of the magnetic field, found by fitting Eq. (3.6) to the microwave transmission data. The solid lines represent the real part of $\Re(E_{\mathrm{u}/_1,\mathrm{inco}})/h$. (b) HWHM linewidth of the two transmission dips, for the upper (blue symbols) and lower (red symbols) branch of the avoided crossing, shown in (a). The solid lines are calculated by $|\Im(E_{\mathrm{u}/_1,\mathrm{inco}})/h|$. The best agreement with the data in (a) and (b) is obtained for $\kappa_0/2\pi = 410\,\mathrm{kHz}$, $\gamma_{\mathrm{HF}}/2\pi = 670\,\mathrm{kHz}$, $g_{\mathrm{eff}}/2\pi = 1.23\,\mathrm{MHz}$ and $g_{\mathrm{inco}}/2\pi = -250\,\mathrm{kHz}$.

decreases to a minimum of $230\,\mathrm{kHz}$ at $B_0 = 172.56\,\mathrm{mT}$. For larger magnetic fields, the linewidth increases to a value, which is expected to be governed by loss rate γ of the spin ensemble. In the case of the lower branch, the linewidth peaks at $B_0 = 172.56\,\mathrm{mT}$ with a maximum of $854\,\mathrm{kHz}$ and decreases to a linewidth given by $\kappa_0/2\pi$, for large magnetic fields. The extracted linewidth data can be described quantitatively by $|\Im(E_{\mathrm{u}/_1,\mathrm{inco}})/h|$ (solid lines in Fig. 3.17 (b)). Here, the parameters given in Tab. 3.4 are used, except for γ_{HF} to obtain a better agreement with the data (see figure caption). To reproduce the asymmetric linewidth distribution, an incoherent coupling rate of $g_{\mathrm{inco}}/2\pi = -250\,\mathrm{kHz}$ is assumed. Although, g_{inco} is by a factor of five smaller than the coherent coupling rate g_{eff}, it provides a significant contribution to the loss rate evolution of the upper and lower branches of the avoided crossing (cf. Sec. 3.2.3). The point of average linewidth, where both split transmission dips have a linewidth of $\frac{\kappa_0 + \gamma_{\mathrm{HF}}}{2}$, is shifted from the degeneracy point to a higher magnetic field.

Next, the assumption of an incoherent coupling rate is tested on the measured microwave transmission data $|S_{21}|^2$. Based on Eq. (3.59), incorporating a complex microwave drive with phase φ, g_{inco} is introduced by changing g_{eff} to $\tilde{g}_{\mathrm{eff}} = g_{\mathrm{eff}} - ig_{\mathrm{inco}}$. In addition, an offset S_0 is included to take the high frequency losses of the CPW feedline into account. Together, this yields for the microwave transmission

$$|S_{21}|^2 = S_0 \left(\frac{\eta}{\kappa_0}\right)^2 \left| \kappa_0 - \frac{\kappa_0 e^{i\varphi}}{i\Delta_{\mathrm{r}} + \kappa_0 + \frac{\tilde{g}_{\mathrm{eff}}^2}{i\Delta_{\mathrm{s}}+\gamma}} \right|^2 . \tag{3.62}$$

Figure 3.18 (a) shows the microwave transmission $|S_{21}|^2$ of the LER B. Equation (3.62) fits in good agreement to the uncoupled resonator transmission data, as shown in Fig. 3.18 (b) for $B_0 = 167.4\,\mathrm{mT}$. To describe the data in the interaction region, the resonator loss rate is fixed to $\kappa_0/2\pi = 410\,\mathrm{kHz}$ to improve the robustness of the fit. Furthermore, the selection of appropriate start values for the spin ensemble's loss rate, the coherent and incoherent coupling rates is made with respect to the previously determined parameters,
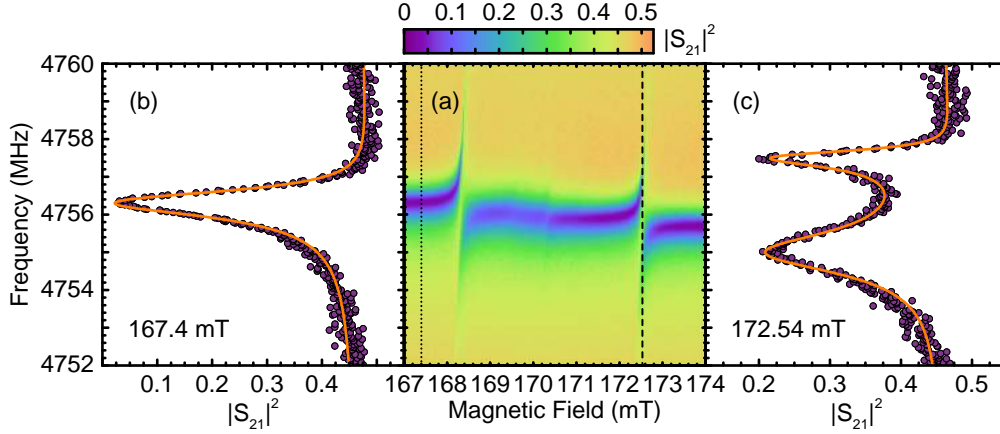
Figure 3.18: (a) Microwave transmission $|S_{21}|^2$ of the LER B as a function of the VNA frequency and magnetic field, at a temperature of 50 mK and a microwave power of 40 aW. (b) $|S_{21}|^2$ of the uncouple microwave resonator (symbols) as a function of the VNA frequency for a magnetic field of 167.4 mT (indicated by the dotted line in (a)). (c) $|S_{21}|^2$ of the coupled microwave resonator / spin ensemble hybrid system (symbols) as a function of the VNA frequency at the HF spin transition field of 172.54 mT (indicated by the dashed line in (a)). The orange solid lines in (b) and (c) are fits using Eq. (3.62).

to prevent the use of unrealistic parameters. As shown in Fig. 3.18 (c), with the assumption of an incoherent coupling rate g_{inco} in combination with a complex microwave drive allows to reproduce the asymmetric linewidth of the normal mode splitting extremely accurately. This fit returns a loss rate of the spin ensemble $\gamma_{\mathrm{LF/HF}}/2\pi = 596/602\,\mathrm{kHz}$, corresponding to a FWHM magnetic field linewidth of $\Delta B_{\mathrm{LF/HF}} = 42.61/43.04\,\mu\mathrm{T}$. Further, an incoherent coupling rate $g_{\mathrm{inco,LF/HF}}/2\pi = 265/265\,\mathrm{kHz}$ and a coherent coupling rate $g_{\mathrm{eff,LF/HF}}/2\pi = 1.32/1.15\,\mathrm{MHz}$ are determined. g_{eff} exceeds for both spin transitions the individual loss rates of microwave resonator and spin ensemble, demonstrating that the hybrid system still resides in the strong coupling regime, with cooperativities of $C_{\mathrm{LF/HF}} = 7.12/5.38$.

Extending the Tavis-Cummings model by an incoherent coupling rate g_{inco} allows to describe the asymmetric linewidth of the normal mode splitting, observed with the LER experiments. However, the exact nature of this incoherent interaction asks for further investigations. The CPW feedline of the LER can act as a possible bath for modes with no definite phase relations, providing an indirect and incoherent energy transfer between microwave resonator and spin ensemble. This assumption still needs to be verified, in addition to identifying the dependencies on the magnitude of the incoherent coupling rate g_{inco}. A possible approach would be to systematically study the hybrid system for different overlaps of the phosphorus doped $^{28}\mathrm{Si}$ crystal and the CPW feedline. When the incoherent coupling process is mediated via feedline, a dependence of g_{inco} on the overlap would be expected.

Chapter 4

Pulsed Microwave Spectroscopy

Pulsed microwave spectroscopy is a powerful tool, to investigate the properties of spins in the time domain. This includes the intrinsic relaxation and coherence time T_1 and T_2, respectively, as well as the interaction strength between spins or spin species. For quantum information processing, the coherence time is the most relevant timescale as the quantum state can only be conserved on this time scale. Therefore, for a possible quantum storage application, long coherence times are desirable. In particular, phosphorus donors in isotopically purified ^{28}Si are known for their record breaking long electron spin coherence times [4, 5, 11], these systems comprise excellent candidates for such an endeavor. An implementation in common quantum circuits requires an interface, for the incorporation of the spin system. One realization comes in the form of a microwave resonator [9, 10]. To allow for a coherent exchange of information between the individual systems, strong coupling is a mandatory requirement. Up to now only a few theoretical and experimental studies investigated the regime of a strongly coupled hybrid system [20, 35, 36], especially when concerning its characteristic time constants [37, 38].

In this chapter, the dynamical response of the coupled system comprised of a microwave resonator and a phosphorus donor spin ensemble is studied when stimulated by a microwave pulses. In Sec. 4.2 the hybrid system is excited into a steady state by a long microwave pulse. For these experiments, an additional third mode is observed, which is attributed to a high power regime of the Tavis-Cummings model. The free induction decay, present after the microwave excitation shows an enhanced decay time for the hybrid system by orders of magnitude, with respect to an uncoupled phosphorus donor spin ensemble.

Section 4.3 discusses the coherence time T_2 and energy relaxation time T_1 of the hybrid system, utilizing Hahn-echo spectroscopy and inversion recovery pulse sequences, respectively. Both characteristic time constants are investigated as a function of temperature and compared to the time constants, obtained for an extremely weak coupled phosphorus donor spin ensemble. For the coherence time, an enhancement of two orders of magnitude is observed compared to quasi uncoupled case. The energy relaxation time is found to follow the expected temperature dependence for an uncoupled spin ensemble for temperatures ranging down to 230 mK. Below this temperature, a constant T_1 time would have been expected, but a T^{-3} power-law for the T_1 time is observed.

4.1   Pulsed Mircowave Setup Calibration

During this thesis, the cryogen free dilution refrigerator setup (cf. Sec. 2.3.1) is adapted
to allow for pulsed microwave experiments. Although, the dilution refrigerator setup
is technically ready to enable pulsed experiments without any technical modifications,
the specific software for the employed equipment as described in Sec. 2.3.2 had to be
developed or adapted. Most of this work was accomplished by K. Müller, during his
master's thesis [113]. To verify the correct operation of the time domain setup, a series of
calibration measurements have been performed.

The initial experiment shall demonstrate that the phosphorus donor spin ensemble can
be excited by a single long microwave pulse, using the CPWR sample (cf. Sec. 3.3). A
250 μs long microwave pulse is applied at the resonance frequency of the first harmonic
of the CPWR, with a frequency of 4.936 GHz and a microwave power at the resonator of
$I_{\mathrm{input}}^2 = 200 \, \mathrm{pW}$. At a temperature of 50 mK the pulse sequence consisting of this pulse
and a wait-time of 25 s between each successive pulse is applied for different magnetic
field values. For static magnetic fields ranging from 178 mT to 180 mT, the temporal
response of the high-field spin transition of the phosphorus donor spin ensemble is probed.
Figure 4.1 (a) plots the logarithmic scaled microwave transmission I^2/I_{input}^2, detected by
the spectrum analyzer, as a function of the static magnetic field and time. The 250 μs long
microwave pulse is initiated at $t = 0 \, \mathrm{s}$ and ends at $t = 250 \, \mu\mathrm{s}$. The figure only shows the
last 0.5 μs of the pulse, which is indicated by the high transmission. When the microwave
power is set to zero at the end of the pulse at $t = 250 \, \mu\mathrm{s}$, the microwave transmission
decays exponentially, with a time constant τ, which is characteristic for the decay rate of
the microwave resonator and / or the spin ensemble, depending on the applied magnetic
field. At $B_0 = 178.68 \, \mathrm{mT}$, τ is significantly longer, suggesting that the emission rate
of microwave photons from the resonator is suppressed due to the presence of the spin
ensemble. The signal trace at the high-field spin transition magnetic field as a function of
the time is shown in Fig. 4.1 (b), together with a trace away from the spin resonance at
179.8 mT, for reference. The time constant τ for magnetic fields far away from the spin
transition is extracted by fitting an exponential decay function to the falling edge of the
microwave pulse,

$$\frac{I(t)}{I_{\mathrm{input}}} = A e^{-\frac{t - t_{\mathrm{off}}}{\tau}} + I_0. \tag{4.1}$$

A represents an amplitude factor, the time offset t_{off} marks the end of the pulse and I_0
represents a transmission offset, due to the finite noise in the setup and the detection
electronics. Note, that Eq. (4.1) describes a decay of the linear microwave transmission
I/I_{input}, which is proportional to a voltage signal ratio. The squared microwave trans-
mission I^2/I_{input}^2 corresponds to a power ratio, which would result in an additional factor
of 2 in the exponent of the exponential decay function. For the magnetic field range
of 179.5 mT to 180 mT, an average time constant of $\tau = 369.2 \, \mathrm{ns}$ is determined, which
translates via [72]

$$\Gamma = \frac{1}{\tau}, \tag{4.2}$$

to a frequency HWHM of $\Gamma/2\pi = 431 \, \mathrm{kHz}$. This value can be linked to the CPWR loss
rate κ_0 determined by continuous wave spectroscopy and thus can be identified with the
ring down time of the microwave resonator τ_{r}. Note, that the extracted loss rate κ_0 and
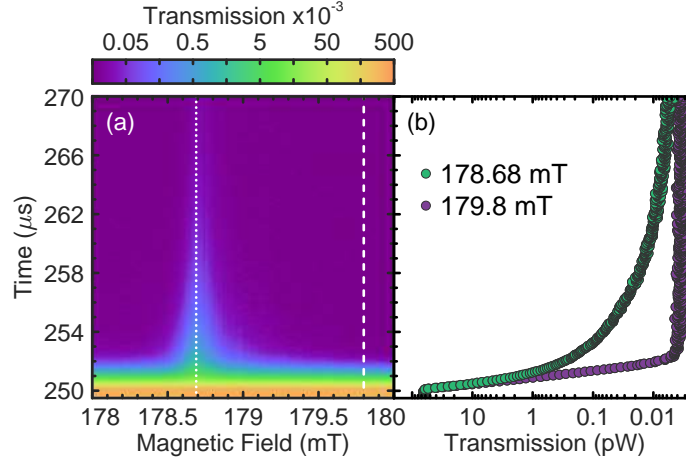
Figure 4.1: (a) Microwave transmission I^2/I_{input}^2 scaled logarithmically as a function of time at a temperature of $50\,\mathrm{mK}$, showing the dynamical response of the system to a $250\,\mu\mathrm{s}$ long microwave pulse, which is initiated at $t = 0\,\mathrm{s}$ (not shown) and ends at $t = 250\,\mu\mathrm{s}$. The pulse's frequency matches the resonance frequency of the first harmonic mode of the CPWR of $4.936\,\mathrm{GHz}$ and has a pulse amplitude of $I_{\mathrm{input}}^2 = 200\,\mathrm{pW}$ when it reaches the resonator. About a magnetic field of $178.68\,\mathrm{mT}$ the time constant of the microwave power decay is enhanced, which is attributed to the phosphorus donor high-field spin transition interacting with the microwave resonator. (b) Microwave transmission as a function of time for a fixed magnetic field of $178.68\,\mathrm{mT}$ and $179.8\,\mathrm{mT}$, indicated by the white dotted and dashed lines in (a), respectively.

resonance frequency ω_{r} are increased compared to the parameters determined in Sec. 3.3, which is attributed to the larger amount of trapped flux vortices [86, 87], due to the extensive use of static magnetic field sweeps.

Studying a spin system by pulsed microwave spectroscopy requires to ensure that the spin system is prepared in the same initial state prior each successive pulse. Here, this state is typically the ground state, which is e.g. obtained after waiting for several T_1 time constants. Waiting for $5T_1$ ensures that the system is to $99\,\%$ back into its ground state, assuming the maximal (inversion) of the spin ensemble. [114]. Thus, T_1 limits the repetition rate of a given pulse sequence, the so called shot-repetition-time (SRT). For the magnetic field sweep in Fig. 4.1 (a) a SRT of $20\,\mathrm{ms}$ is used, which is increased due to the time required to set a new magnetic field point, which is about $25\,\mathrm{s}$. Extrapolating T_1 to a temperature of $50\,\mathrm{mK}$, a static magnetic field of $178.7\,\mathrm{mT}$ and a phosphorus donor concentration of $[\mathrm{P}] = 1 \times 10^{17}\,\mathrm{cm}^{-3}$ from Ref. [115–117], a T_1 time of $46\,\mathrm{s}$ is expected, assuming an energy relaxation via a direct phonon process in the low temperature regime.

To verify this expectation without the use of more advanced pulse sequences (see inversion recovery sequence in Sec. 4.3.3), a series of single pulse experiments are conducted to estimate an appropriate SRT. Figure 4.2 shows the logarithmically scaled CPWR transmission of the falling edge of a single $11\,\mu\mathrm{s}$ long microwave pulse as a function of time, with microwave resonator and spin ensemble tuned in resonance. The signal traces, with a pulse amplitude of $2\,\mathrm{nW}$ at the resonator, are averaged for 25 times, using different SRTs, ranging from $0.5\,\mathrm{s}$ to $1000\,\mathrm{s}$. With increasing SRT the time constant of the microwave power decay increases, and saturates for the two longest SRTs. The overlapping signal traces using a SRT of $500\,\mathrm{s}$ and $1000\,\mathrm{s}$ indicate, that the spin system has reached its ground state before each successive pulse, resulting in an identical signal trace for all 25
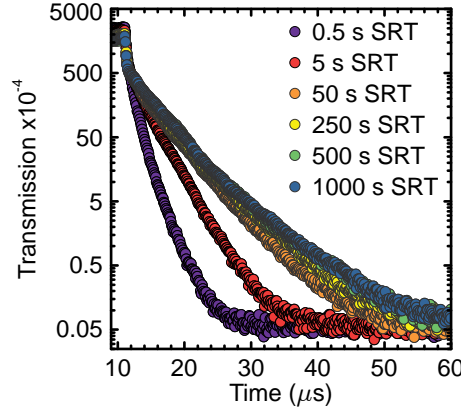
Figure 4.2: Logarithmically scaled microwave transmission I^2/I^2_{input} as a function of time, showing the falling edge of a 11 µs long pulse with an amplitude of 2 nW applied to the CPWR. Each trace is averaged 25 times, using a different SRT (see legend).

averages. Thus, for the first pulsed microwave experiments on the CPWR, a SRT of 500 s is used. The found 500 s allow to roughly estimate the T_1 time to 100 s for a temperature of 50 mK. The coarse determination of the T_1 time is only a factor of two larger than the expected relaxation time, showing that this method is well capable of identifying the order of magnitude of T_1.

After optimizing the SRT to obtain the maximum data acquisition rate, a pulsed microwave spectroscopy can be performed on the hybrid system, ensuring the same initial state prior to each successive microwave pulse.

4.2 Single Pulse Spectroscopy

In the following, the dynamical response of the coupled microwave resonator / spin ensemble hybrid system is studied, by applying a single long microwave pulse. Here, the pulse is sufficiently long to drive the coupled system into a steady state. The evolution of the dynamical response during the pulse is investigated, as a function of the detuning from the degeneracy point of the hybrid system. Furthermore, the decay behavior of the excited microwave resonator / spin ensemble system is analyzed.

4.2.1 Pulsed Steady State Dynamics

The previous chapter studied the spectroscopic features of the hybrid system under the influence of a weak continuous microwave signal. Here, the averaged response on the microwave transmission is detected, within the set measurement bandwidth of 50 - 100 Hz. In the following, a complementary approach is presented, by applying a single microwave pulse to the microwave resonator / spin ensemble hybrid system, for a sufficiently long time to drive the system into a steady state. Thereby, the length of the pulse is required to be longer than the characteristic time constants of the microwave resonator $1/\kappa_0$ and the spin ensemble $1/\gamma$, as well as the collective coupling $1/g_{\mathrm{eff}}$ [20]. During the duration of the pulse, the evolution of the coupled system is observed. Figure 4.3 (a) shows the color coded microwave transmission I^2/I^2_{input} of a 100 µs long pulse applied to the coupled resonator / spin ensemble system, as a function of the pulse frequency and time. At a
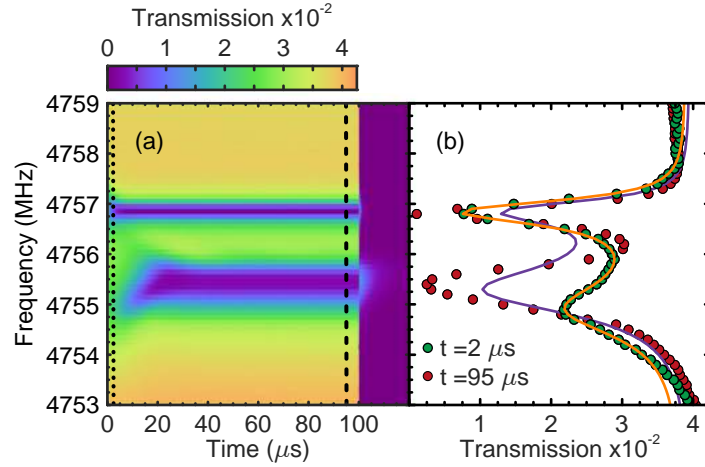
Figure 4.3: (a) Microwave transmission I^2/I_{input}^2 of a 100 µs long microwave pulse, as a function of the pulse frequency and time. The pulse is applied to lumped element resonator B, which is interacting with the high-field spin transition of the phosphorus donor spin ensemble, at a static magnetic field of 172.25 mT and a temperature of 50 mK. At $t = 0$ s the microwave pulse is initiated and ends at $t = 100$ µs, having a pulse amplitude of $I_{\text{input}}^2 = 2$ nW at the LER chip. (b) Microwave transmission I^2 as a function of the pulse frequency for two fixed times. The corresponding transmission spectra at $t = 2$ µs (green symbols) and $t = 95$ µs (red symbols) are indicated by dotted and dashed lines in (a), respectively. The orange and purple solid lines represent a fit of Eq. (3.62) to the spectroscopic data at $t = 2$ µs and $t = 95$ µs, respectively.

temperature of 50 mK the high-field spin transition of the phosphorus donors is tuned via B_0 close to the resonance frequency of lumped element resonator B ($\omega_{\text{r}} > \omega_{\text{s,HF}}$), using a static magnetic field of 172.25 mT. Using a SRT of 1000 s, a pulse is applied at each set frequency and starts at $t = 0$ s and ends at $t = 100$ µs, indicated by the high transmission in Fig. 4.3 (a), with the pulse having an amplitude of $I_{\text{input}}^2 = 2$ nW at the input of the LER chip.

Along the frequency axis, the high transmission during the microwave pulse is reduced at the frequencies of 4.7568 GHz and at about 4.7552 GHz. The two absorption dips represent the normal mode splitting of the microwave resonator, due to the interaction with the spin ensemble and are separated by twice the collective coupling g_{eff} of the hybrid system. Complementary to the CW spectroscopy results, the two absorption dips exhibit different linewidths. Here, the asymmetric linewidth of the normal mode splitting is also attributed to the in Sec. 3.4.2 discussed incoherent coupling process, where the two subsystems indirectly exchange excitations via a bath of vacuum field modes. Furthermore, the two lines show a different time evolution. The resonance frequency of the high frequency mode remains constant during the duration of the pulse, while the resonance frequency of the lower frequency mode shifts to higher frequencies with increasing time. From an initial frequency of 4.7549 GHz the mode shifts during the first 20 µs, settling on 4.7554 GHz for the rest of the pulse. The shift in frequency is attributed to the more spin-like character of the low frequency mode, since $\omega_{\text{r}} > \omega_{\text{s,HF}}$. Due to the high pulse amplitude the spin ensemble gets partly saturated, reducing the number of polarized spins N and consequently the collective coupling ($g_{\text{eff}} \propto \sqrt{N}$), reducing the separation of the two hybrid modes.

Investigating the microwave transmission along the frequency axis for fixed times allows to extract the dynamical parameters of the coupled system, similar to the evaluation of the

CW spectroscopy data (cf. Sec. 3.4). Figure 4.3 (b) plots the microwave transmission at $t = 2\,\mu s$ and $t = 95\,\mu s$, indicated by the dotted and dashed lines in Fig. 4.3 (a). The depth of the absorption dips increases with increasing pulse duration, reaching their maximal depth after about $20\,\mu s$, coincidental with the settling of the lower frequency mode's frequency shift. To extract the dynamical parameters Eq. (3.62) is fitted to the transmission spectra, using a fixed resonator loss rate of $\kappa_0/2\pi = 410\,\text{kHz}$ (cf. Sec. 3.4.2). For the spectra at $t = 2\,\mu s$ the fitted curve is in good agreement with the experimental data, yielding $\gamma_{\text{HF}}^{2\,\mu s}/2\pi = 544\,\text{kHz}$, $g_{\text{eff,HF}}^{2\,\mu s}/2\pi = 1.0\,\text{MHz}$ and $g_{\text{inco,HF}}^{2\,\mu s}/2\pi = 184\,\text{kHz}$. The determined parameters are comparable to the parameters given in Sec. 3.4.2, except for $g_{\text{inco,HF}}$ being a factor of two smaller. In contrast, fitting the spectrum at $95\,\mu s$ results in a poor fit, as the depth of the absorption dips is not reproduced by Eq. (3.62). It is suggested, that this is a result due to the high microwave power. Equation (3.62) is based on the solutions of the Tavis-Cummings model, introduced in Sec. 3.2.2. For its derivation, the number of excitations n_{ex} is assumed to be much smaller than the number of spins N. The longer the microwave pulse is applied, the more excitations are introduced to the system, until this assumption is violated. At the beginning of the microwave pulse, the number of excitations introduced to the system is still small and thus the spectra can be modeled using Eq. (3.62). At the end of the pulse, the spectra significantly differ, showing almost zero transmission at the two absorption dips. Both absorption dips exhibit an equal depth, which would not have been expected for a hybrid system detuned from the degeneracy point. Nevertheless, the frequency of the resonant modes can be reproduced very well by the fit, allowing to determine the collective coupling to $g_{\text{eff,HF}}^{95\,\mu s}/2\pi = 744\,\text{kHz}$.

For a more complete analysis of the hybrid system in the high power regime, identical experiments are conducted for various static magnetic fields B_0 in the spin-resonator coupling regime. To obtain a comparable series of spectra, B_0 is only decreased or increased between each successive measurement to avoid hysteretic effects of the superconducting microwave resonator [118]. Beginning at $B_0 = 172.46\,\text{mT}$ the magnetic field is increased stepwise, rasterizing the avoided level crossing of the hybrid system. Figure 4.4 (a) shows a corresponding low power CW microwave transmission spectroscopy of the hybrid system, as reference for the single pulse spectroscopy (cf. Sec. 3.4.1). Dashed lines indicate the magnetic field values, at which a pulse spectroscopy is performed. Figures 4.4 (b)-(f) show the color coded microwave transmission of the coupled system when stimulated by a $100\,\mu s$ long pulse, as a function of the pulse frequency and time, for magnetic fields ranging from $172.46\,\text{mT}$ to $172.51\,\text{mT}$. All experiments are conducted at a temperature of $50\,\text{mK}$ and with a pulse amplitude of $2\,\text{nW}$. The spectrum at the smallest magnetic field is comparable to the spectra shown in Fig. 4.3 (a). Note, that a similar detuning from the degeneracy point is possible for different absolute static magnetic fields, due to magnetic hysteresis effects in the superconducting microwave resonator, resulting from sweeping the magnetic field in different directions [118]. At the following magnetic field point at $172.47\,\text{mT}$, the low frequency hybrid mode becomes more prominent and exhibits an increased width. For $B_0 = 172.48\,\text{mT}$ an additional mode has separated from the low frequency mode. Further increasing B_0 to $172.5\,\text{mT}$ shifts the additional mode to higher frequencies closer to the high frequency mode of the hybrid system, with which it merges at the the last magnetic field value of $172.51\,\text{mT}$.

The resonance frequency of the individual modes is analyzed in Fig.4.5 (a) as a function of the static magnetic field at $t = 95\,\mu s$. The central mode exhibits a linear trend with
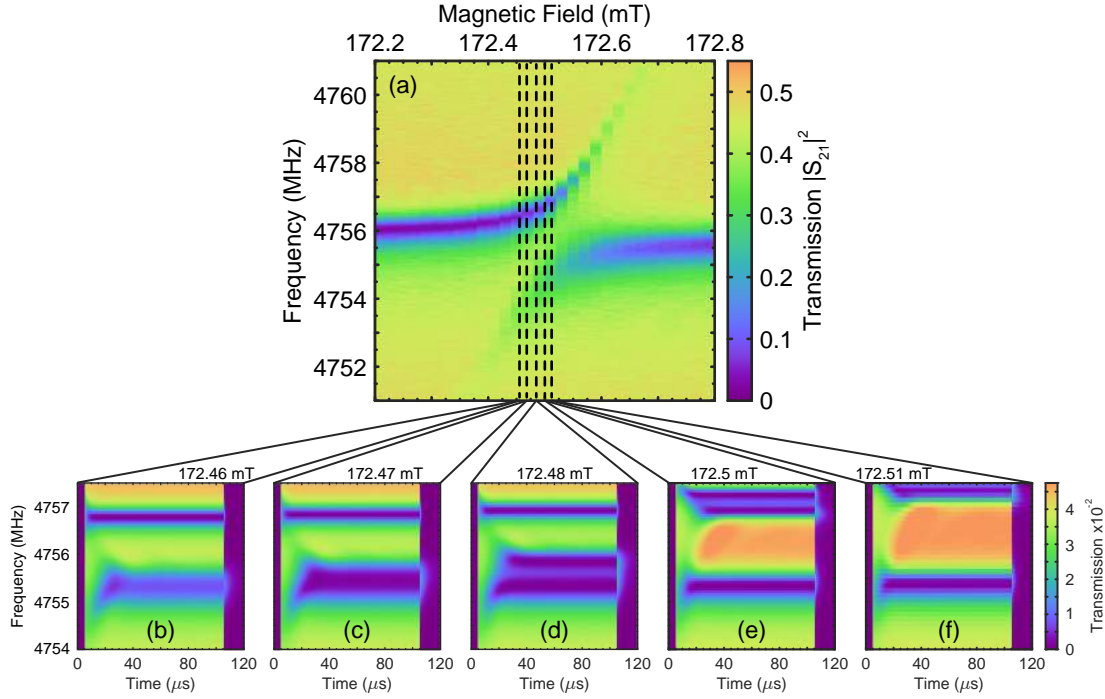
Figure 4.4: (a) Color coded microwave transmission data $|S_{21}|^2$ as a function of the VNA
frequency and the magnetic field B_0, of lumped element resonator B coupled to the high-field
spin transition of the phosphorus donor spin ensemble, taken at a temperature of 50 mK and
an input microwave power of 40 aW. (b)-(f) Microwave transmission spectra of a 100 µs long
pulse as a function of the pulse frequency and time at $T = 50$ mK. The pulses are applied to
the hybrid system at different static magnetic fields, indicated by the dashed lines in (a). A
pulse amplitude of $I_{\mathrm{input}}^2 = 2$ nW at the LER chip and a SRT of 800 s is used.

increasing B_0, connecting the upper and lower frequency modes. The magnetic field disper-
sion of the upper and lower frequency modes of the hybrid system are given by the energy
eigenstates $E_{\mathrm{u}/_1,\mathrm{inco}}$ of the Tavis-Cummings model, given in Eq. (3.61), which also includes
the incoherent coupling observed in the LER experiments (cf. Sec. 3.4.2). The resonance
frequency dispersion is calculated via $\Re(E_{\mathrm{u}/_1,\mathrm{inco}})/h$ (dashed lines in Fig. 4.5 (a)), which
significantly differs from the resonance frequencies found by single pulse spectroscopy.
For this calculation, the previously determined collective coupling $g_{\mathrm{eff,HF}}^{95\,\mu s}/2\pi = 744$ kHz is
used. Additionally, a microwave resonator resonance frequency of $\omega_\mathrm{r}/2\pi = 4.7561$ GHz
and $g_{\mathrm{inco}}/2\pi = -250$ kHz are assumed and ω_s is determined via the spin Hamiltonian
given in Eq. (2.10). Apart from the absence of the additional central mode, the theoret-
ical dispersion exhibits a steeper slope in the vicinity of the degeneracy point, especially
in comparison with the experimentally observed dispersion of the lower frequency mode.
Note, that this theoretical model only assumes a single excitation to be present in the
hybrid system, which fits the low power CW experiments with excellent agreement (cf.
Sec. 3.2), but is insufficient to describe the high power pulsed experiments. Expanding the
model to more than one excitation yields additional modes [23]. The single pulse spec-
troscopy is performed at high microwave powers, applying a pulse amplitude of 2 nW to
the resonator. LER B shows an absorption depth of 13 dB (cf. Sec. 3.4.1), which corre-
sponds to an average number of $n = 4 \times 10^7$ photons stored in the resonator. Based on the
estimation of the single photon single spin coupling rate g for the CPWR of 11.1 Hz (see
Eq. (3.21)) the coupling rate for the LER is determined to $g^{\mathrm{LER}}/2\pi = 35.1$ Hz, assuming
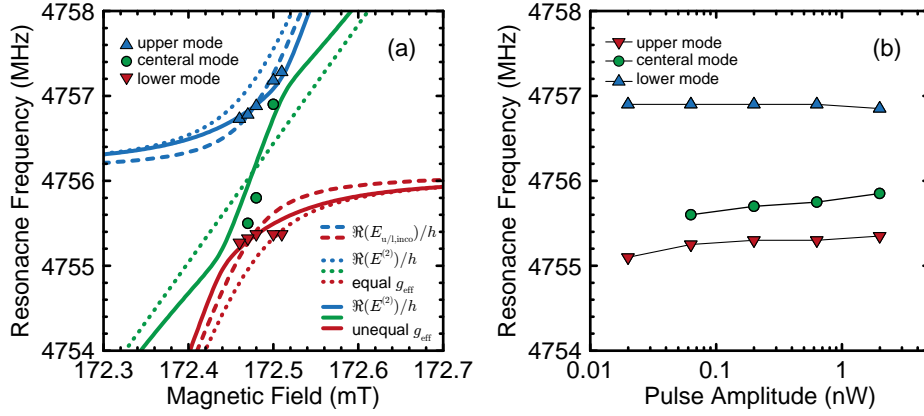
Figure 4.5: (a) Resonance frequencies of the three hybrid modes (symbols) as a function of the static magnetic field, determined from the single pulse spectroscopies shown in Fig. 4.4 (b)-(f) at the end of the 100 µs long microwave pulse. The dashed lines are the solutions $\Re(E_{u_{/1},\text{inco}})/h$ of Eq. (3.61), which considers a single excitation present in the hybrid system. Thereby, $g_{\text{eff,HF}}^{95\,\mu s}/2\pi = 744\,\text{kHz}$, $g_{\text{inco}}/2\pi = -250\,\text{kHz}$ and $\omega_r/2\pi = 4.7561\,\text{GHz}$ are used and ω_s is determined via the spin Hamiltonian in Eq. (2.10). The dotted and solid lines represent the solutions $E^{(2)}/h$ of the two excitations Tavis-Cummings Hamiltonian $H_{\text{TC}}^{(2)}$, using the same parameters, excluding g_{inco}. For the dotted line an equal collective coupling for both excitations is assumed and for the solid line the collective coupling of the second excitation is assumed to be 20 % of the collective coupling of the first excitation. (b) Resonance frequencies of the three hybrid modes as a function of the applied pulse amplitude. The power series is conducted at $B_0 = 172.48$ and the respective resonance frequencies are determined at the end of the 100 µs long microwave pulse.

that the mode volume of the LER is one order of magnitude smaller, due to its smaller dimensions. Using the found collective coupling rate $g_{\text{eff,HF}}^{95\,\mu s}$ the number of interacting spins is determined to $N = (g_{\text{eff,HF}}^{95\,\mu s}/g^{\text{LER}})^2 = 4.5 \times 10^8$. The number of photons is only a factor of 10 smaller than the number of interacting spins, making the assumption of multiple excitations in the hybrid system reasonable.

When introducing an additional excitation to the Tavis-Cummings model the number of possible energy states is increased by one. The matrix representation of this modified Hamiltonian is given by a 3×3 matrix [23]

$$H_{\text{TC}}^{(2)} = \hbar \begin{pmatrix} \omega_s & g\sqrt{2N} & 0 \\ g\sqrt{2N} & \frac{1}{2}(\omega_r + \omega_s) & g\sqrt{2(N-1)} \\ 0 & g\sqrt{2(N-1)} & \omega_s \end{pmatrix}, \tag{4.3}$$

where the losses of the individual subsystems are neglected for simplicity. Note, that the coupling strength between the multiple modes is modified due to additional excitation present in the system. The probability of exciting the spin ensemble with two excitations in the resonator is enhanced, as represented by the additional $\sqrt{2}$ factor for the coupling terms. Consequently, the probability for the second excitation of the spin ensemble is reduced, since the number of spins in the ground state is reduced to $N - 1$. Here, the number of spins is estimated to $N = 4.5 \times 10^8$, where $N - 1 \approx N$ and the collective couplings for the first and second excitation are equal. The eigenstates $E^{(2)}/h$ of $H_{\text{TC}}^{(2)}$ yield the dispersions of three hybrid modes, using $g\sqrt{2N} = g_{\text{eff,HF}}^{95\,\mu s}$. The upper and lower frequency modes describing an avoided crossing and the central mode runs at the frequency center of mass of the upper and lower modes (see dotted lines in Fig. 4.5 (a)). However,

the theoretically predicted dispersion of the central mode has a smaller slope than the experimentally observed one. To describe the experimental data a modification to the theoretical framework is suggested. The slope of the central mode's dispersion can be increased by reducing the collective coupling of the second excitation. The average photon number n in the system is determined to 4×10^7. The theory presented in Ref. [23] predicts the occurrence of additional modes in the hybrid system's spectrum, for the case when n is comparable to N. Therefore, a change of $N - 1 \mapsto N - n$ is assumed, which increases the difference between the two coupling rates, as the number of photons n is increased. For a qualitative description of the experimental data a reduction of the collective coupling for the second excitation to $0.2g\sqrt{2N}$ has to be assumed (solid lines in Fig. 4.5 (a)), whereas for the estimated values only a reduction to $0.95g\sqrt{2N}$ is obtained. Note, that the estimation of the single photon single spin coupling strength for the LER is very coarse. A more refined estimation using a finite element simulation of the magnetic field distribution of the resonator would allow a more precise approximation of the coupling strength, which could bring the number of interacting spins closer to the number of photons. Unfortunately, due to the limited amount of time available during the course of this thesis, such simulation could not be conducted. In addition to the increased slope of the central mode's dispersion with reducing collective coupling of the second excitation, the dispersion of the calculated upper and lower frequency modes get flatter in the vicinity of the degeneracy point. These characteristics can also be found for the measured magnetic field dispersion of the three hybrid modes, suggesting that the occurrence of the additional mode can be attributed to the high microwave powers used.

The static magnetic field dispersion of the additional mode notably exhibits a similar slope, as the dispersion of the uncoupled high-field spin transition of the phosphorus donor spin ensemble (cf. green dashed line in Fig. 3.8 (a)). Thus, the part of the ^{28}Si crystal covering part of the CPW feedline (cf. Sec. 2.3.3) could contribute to the observed pulsed signal. To exclude that the central mode stems from the crystal atop the CPW feedline, a microwave power series is conducted. For the suggested two excitation model, the resonance frequency of the additional mode should show a dependence on the applied microwave power. With deceasing power, the slope of the magnetic field dispersion for the central mode is expected to decrease, while for conventional ESR no change is expected. To this end, the single pulse spectroscopy at a static magnetic field of 172.48 mT, shown in Fig. 4.4 (d), is is performed as a function of the pulse amplitude. At each set power, the resonance frequencies of the three modes are determined at the end of the microwave pulse and summarized in Fig. 4.5 (b). As $\omega_\mathrm{r} > \omega_\mathrm{s,HF}$ for $B_0 = 172.48$ mT, the central mode is expected to shift to higher frequencies with decreasing pulse amplitude. As the number of photons n decreases with decreasing pulse amplitude, the dispersion approaches the case where $N - n \approx N$, where the dispersion of the central mode follows the frequency center of mass of the upper and lower modes (dotted lines in Fig. 4.5 (a)). However, a shift to smaller frequencies with decreasing pulse amplitude is observed in the experiment. A reduction of the microwave power by 15 dB shifts the central mode's resonance frequency down by 250 kHz. In addition, the occurrence of the central mode is increasingly delayed in time for decreasing power. Nevertheless, the observation of a resonance frequency shift rules out, that the central mode corresponds to a conventional ESR signal, driven by the CPW feedline.

The suggested two excitation model can qualitatively describe the static magnetic field

dispersion of the three hybrid modes, as it predicts the additional central mode. Furthermore, the slopes of the dispersion of the upper and lower frequency modes show a better agreement with the two excitation model, compared to the solutions of the Tavis-Cummings model, assuming a single excitation distributed in the hybrid system. However, the model still requires refinements, as the expected pulse amplitude dependence is not corroborated by the experimental findings. Please note, that the model is based on the assumption of two excitations present in the coupled system. Only by modifying the model to explicitly include the average number of photons n the experimental data can be described qualitatively. A possible refinement would be to use the ratio between the number of photons and the number of spins n/N instead of the absolute number of excitations. In Ref. [23] the absolute number of energy states present in the hybrid system is characterized by the number of excitations. By mapping this characterization onto the ratio n/N, the theoretical framework could be adapted to the present experiment.

4.2.2   Coupled System FID

A resonant microwave pulse ($\omega_\mathrm{r} = \omega_\mathrm{s}$) applied to a spin ensemble transfers energy to the spins during the pulse and thus is capable of driving the system into an excited state. In a classical picture, the magnetization precesses about the magnetic field vector $\mathbf{B}_1$ of the microwave pulse during this process. As this process is in a classical picture covered by the Bloch equations [119], it is evident that this process is most efficient for a perpendicular orientation of $\mathbf{B}_1$ and the static magnetic field $\mathbf{B}_0$. The angle about the magnetization is rotated during the pulse depends on the pulse length and amplitude (see Sec. 4.3). After preparation, the spin ensemble's magnetization performs a free precession about $\mathbf{B}_0$, with the Larmor frequency ω_s. The precessing magnetization can be understood as an oscillating dipole, generating an inductive response in form of a microwave signal in the resonator. The inductive response lasts as long, as the precessing magnetization has a non vanishing projection on the plane, in which $\mathbf{B}_1$ oscillated. With increasing time, the magnitude of this signal decays exponentially, due to a dephasing of the magnetization vector. Such a decaying microwave signal after a microwave pulse is know as a free induction decay (FID). Several processes can cause and contribute to a FID, such as incoherent spin-spin interactions, inhomogeneous broadenings of the spectral spin distribution or the energy relaxation via spin-phonon interactions [72]. For spins in solids, these processes typically act on a much longer time scale as the FID. Here, the dominating process is due to inhomogeneous broadenings of the spectral spin distribution of the ensemble, leading to a destructive interference of the signals from individual spins. The characteristic time constant of a FID is the phase memory time T_2^*, being typically shorter than the coherence time T_2 and the energy relaxation time T_1 [72].

In the following, the FID of the coupled microwave resonator / spin ensemble system is studied, in a regime of strong coupling. For the hybrid system a FID for each individual hybrid mode is expected after microwave pulse excitation. Figure 4.6 (a) shows the logarithmic scaled microwave transmission I^2/I_input^2 induced by the FID of the hybrid system, comprising LER B and the high-field spin transition of the phosphorus donor spin ensemble as a function of the pulse frequency and the pulse sequence time, at a static magnetic field of $172.5\,\mathrm{mT}$ and a temperature of $T = 50\,\mathrm{mK}$. The observed FID follows a $100\,\mathrm{\mu s}$ long microwave pulse, which is switched off at $t = 105\,\mathrm{\mu s}$, with a pulse amplitude of
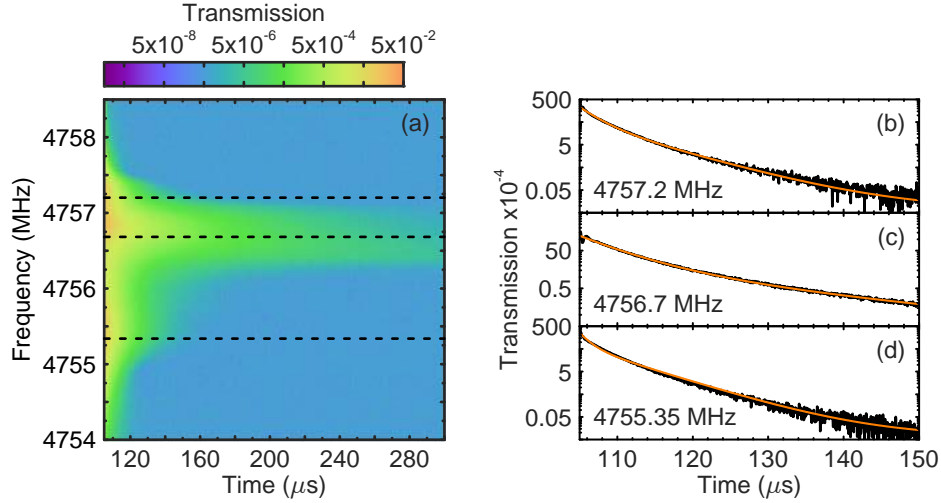
Figure 4.6: (a) Logarithmic scaled microwave transmission I^2/I_{input}^2 of a FID, induced by the LER B / high-field phosphorus donor spin transition hybrid system as a function of the pulse frequency and the pulse sequence time. The coupled system FID follows a 100 μs long microwave pulse, with a pulse amplitude of $I_{\text{input}}^2 = 2$ nW applied to the LER chip. The single pulse spectroscopy is performed at a static magnetic field of 172.5 mT and a temperature of $T = 50$ mK, corresponding to the spectrum shown in Fig. 4.4 (e). (b)-(d) Logarithmic scaled microwave transmission of the coupled system FID as a function of the pulse sequence time (black solid lines). The FIDs of the hybrid system are plotted for fixed pulse frequencies of 4.7572 GHz, 4.7567 GHz and 4.75535 GHz, indicated by the black dashed lines in (a). The solid orange lines represent fits of Eq. (4.4) to the experimental data.

$I_{\text{input}}^2 = 2$ nW applied to the LER chip. The corresponding single pulse spectroscopy over the full length of the microwave pulse is shown in Fig. 4.4 (e). Note, that the spectrum under investigation features the in the previous section discussed additional third hybrid mode (see Sec. 4.2.1). At 4.7572 GHz and 4.75535 GHz, the resonance frequencies of the upper and lower modes, the FID is prolonged and longest at 4.7567 GHz. The longest FID is not observed exactly at the resonance frequency of the additional hybrid mode at 4.7569 GHz. The difference in frequency may be attributed to the absence of the high power microwave drive. As the resonance frequency of the third hybrid mode exhibits a dependence on the applied microwave pulse amplitude (see Sec. 4.2), the small shift of 200 kHz is suggested to be connected to the end of the pulse. Therefore, the longest FID is attributed to the additional hybrid mode.

Figures 4.6 (b)-(d) plot the logarithmic scaled microwave transmission of the coupled system FID as a function of the pulse sequence time, for the respective pulse frequencies of 4.7572 GHz, 4.7567 GHz and 4.75535 GHz. At 4.7567 GHz the signal exhibits an oscillation at the initial decay. During the oscillations, the spin ensemble coherently exchanges energy with the resonator, characteristic for the regime of strong coupling [20]. The FID is best modeled by a bi-exponential decay, which is also a characteristic of strong coupling [33]. Extending Eq. (4.1) with a second exponential term yields,

$$\frac{I(t)}{I_{\text{input}}} = A_1 e^{-\frac{t-t_{\text{off}}}{\tau_1}} + A_2 e^{-\frac{t-t_{\text{off}}}{\tau_2}} + I_0. \tag{4.4}$$

The presence of a second time constant, indicates that the hybrid system decays not as one single collective ensemble, but rather decays in subensembles. Both ensembles decay with their own time constant, a short time constant τ_1 and a long τ_2.
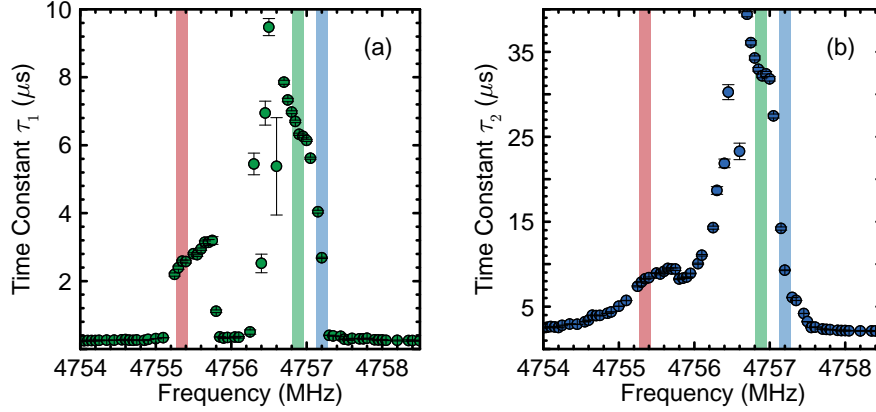
Figure 4.7: Time constants τ_1 (a) and τ_2 (b) as a function of the pulse frequency, determined by fitting Eq. (4.4) to the spectroscopic data shown in Fig. 4.6 (a). The resonance frequencies of the upper, lower and central hybrid modes are highlighted by blue, red and green bars, respectively.

The time constants τ_1 and τ_2 are determined as a function of the pulse frequency from the measured coupled system FID and summarized in Fig. 4.7 (a) and (b), respectively. For the pulse frequencies where strong coherent oscillations are present at the initial decay, the fit yielded no reliable results, which are excluded in Fig. 4.7. The longest extracted time is $\tau_2(4.7567\,\mathrm{GHz}) = 39.4\,\mathrm{\mu s}$, which is by a factor of four longer than the maximum of the shorter time constant $\tau_1(4.7565\,\mathrm{GHz}) = 9.5\,\mathrm{\mu s}$. Both are attributed to the FID of the third hybrid mode and are both exceeding the time constant, corresponding to the spin ensemble loss rate $1/\gamma_{\mathrm{HF}} = 265\,\mathrm{ns}$ by more than two orders of magnitude. The remarkable enhancement of the phase memory time of the hybrid system over the phase memory time of the uncoupled subsystems, is attributed to a subradiant decay process [38, 93, 120, 121]. In the Dicke formalism a subradiant energy state of an ensemble of two-level emitters, coupled to a resonant radiation field, shows a suppressed decay rate. Such states can also suppress decoherence, prolonging a FID [120, 121].

The symmetric nature of the spin-photon interaction in the Tavis-Cummings model connects the resonator only with highly symmetric superradiant spin states of the ensemble, not allowing a coupling to subradiant states due to angular momentum conservation. The state with the highest cooperation number $J = N/2$ (N is the number of spins, cf. Sec. 3.2.2) also poses the highest symmetry, with energy states ranging from $+J$ to $-J$. When the system is in this state, it relaxes superradiant via the resonator into the ground state $-J$, without the need to change its angular momentum [93]. Apart from the superradiant state, there are states with lower cooperation number, which are no longer including the ground state $-J$ of the spin ensemble. When considering e.g. two spin 1/2, such a state is represented by the singlet state. For relaxation to the ground state, an angular momentum change would be required, which can not be provided by a resonator. Thus, the spontaneous emission of the spin ensemble via the resonator is suppressed for these states. For these antisymmetric states, pair correlations between the spins become relevant [121]. For correlated spins the environmental noise, due to e.g. local magnetic field fluctuations, also gets correlated, to which the correlated pair is no longer susceptible [120, 122]. However, the antisymmetric states can only be accessed by breaking the symmetry of the spin-photon interaction, which can be realized by a large inhomogeneous

broadening of the spectral spin distribution or a dipole-dipole interaction [31, 121]. For the given phosphorus donor concentration of $[\text{P}] = 1 \times 10^{17}\,\text{cm}^{-3}$, dipole-dipole interactions can be considered to be sufficiently strong to break the symmetry of the spin-photon coupling. Therefore, a finite coupling to antisymmetric spin states is reasonable for the investigated hybrid system.

Determining the exact origin of the great enhancement of the hybrid system's phase memory time requires further experimental investigation. As the final state of the hybrid system is unknown at the end of the microwave pulse, it is difficult to anticipate the evolution of the system. Optimizing the applied microwave pulses to improve the transfer of energy into the hybrid system may allow to prepare the system in more definite energy states, from which the evolution can be studied more quantitatively. The experimental data shows also an indication, that within the first $100 - 200\,\text{ns}$ an additional fast decay process is present. This may be attributed to the decay of the superradiant energy state. However, with the chosen time resolution the third decay process could not be absolutely verified. This emphasizes the requirement for a well defined energy by the pulse, to analyze if several different energy stats can be prepared by a single pulse. Furthermore, tuning the collective coupling allows to investigate the transition from a conventional FID to the enhanced coupled system FID. The experiments so far are a first step towards effectively tuning the decay behavior of a hybrid system, for which a tuning from a fast processing state to a long storage state is possible.

4.3 Multiple Pulse Spectroscopy

By applying sequences of multiple pulses well known from pulse ESR, the relaxation and coherence time of the system under investigation can be determined. Both are of key interest for memory applications. The two pulse Hahn echo sequence and the three pulse inversion recovery sequence, allow access to the transverse relaxation time or coherence time T_2 and the longitudinal relaxation time or energy relaxation time T_1 of the coupled system, respectively [72]. These techniques are based on the occurrence of a microwave echo after applying the pulse sequence. Adapting the procedures known from conventional pulsed ESR [72, 103], the spin ensemble's magnetization vector is rotated by a definite angle, during the application of a microwave pulse. In the following, a general echo generation process shall be outlined. For a more detailed description of the signal generation see Ref. [72, 123].

Assuming a spin ensemble prepared in the ground state, with its magnetization $\mathbf{M}$ aligned in parallel to the static magnetic field $\mathbf{B}_0$, which defines the axis of quantization. $\mathbf{B}_0$ is assumed to be oriented along the z-axis. For a stationary frame or lab frame, the magnetization vector performs a precession about the static magnetic field $\mathbf{B}_0$, with a frequency given by the Larmor frequency ω_s. For the case of the ground state, the magnetization vector simply spins about its axis. An oscillatory magnetic field $\mathbf{B}_1$ is applied perpendicular (in the xy-plane) to the magnetization vector, oscillating about $\mathbf{M}$. Considering the experiments conducted in this thesis, the frequency of B_1 is defined by the resonance frequency ω_r of the microwave resonator. When the spin ensemble's Larmor frequency ω_s is tuned in resonance with the B_1 field, an additional precession of the magnetization about $\mathbf{B}_1$ is induced. In the stationary lab frame, the magnetization now performs two precessions. One about $\mathbf{B}_0$ with frequency ω_s and a precession about
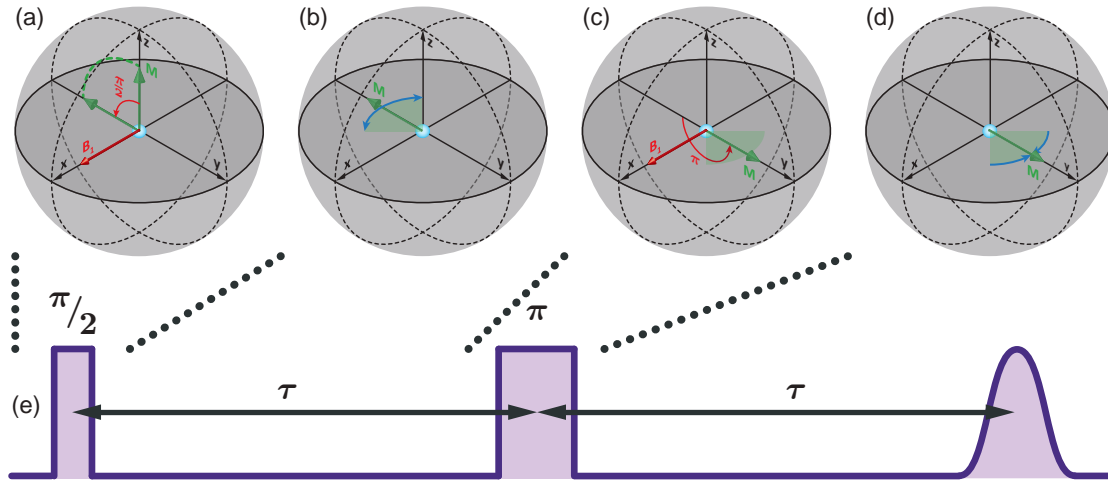
Figure 4.8: Illustration of a general echo generation pulse sequence, utilized in Hahn echo experiments. The frame shown in (a)-(d) rotates with the frequency ω_r of the oscillatory microwave magnetic field B_1, about the z-axis. The microwave field of the resonator and the spin ensemble are assumed in resonance ($\omega_r = \omega_s$). At the start of the pulse sequence, the spin ensemble shall be in its ground state and the magnetization is quantized by the static magnetic field B_0 along the z-axis. (a) The duration of the first pulse is chosen such, that the magnetization $\mathbf{M}$ performs a $\pi/2$ rotation about the oscillatory magnetic field $\mathbf{B_1}$, on the -y-axis. (b) Free evolution of the magnetization for a time τ, where inhomogeneous broadening effects lead to a fan-out of the magnetization vector $\mathbf{M}$ (indicated by the blue arrows). (c) The second pulse rotates the fanned-out magnetization by π, on the +y-axis. (d) As a result of the second pulse, the magnetization starts to refocus after the pulse. After a second evolution time of τ, the magnetization converges and induces an echo signal in the resonator. (e) Schematic of the echo pulse sequence, where the location of the different steps of (a)-(d) are indicated by the dotted lines.

$\mathbf{B_1}$, with a frequency Ω_s. Depending on the magnitude and duration of the applied pulse, the magnetization can be rotated to an arbitrary angle, relative to $\mathbf{B_0}$.

It is convenient to transform the lab frame to a frame, rotating about the quantization axis with a frequency equal to the frequency of the B_1 field. In the following, it is assumed that the resonator is always tuned in resonance with the spin ensemble ($\omega_r = \omega_s$). In this context, Fig. 4.8 (a) - (d) illustrate the main steps during an echo generation pulse sequence, considering ideal pulses [72]. The individual steps are indicated in a sample pulse sequence in Fig. 4.8 (e). The sequence starts with a pulse, applied along the x-axis (see Fig. 4.8 (a)). In the rotating frame, the B_1 field vector is stationary and acts equally on the magnetization, as the B_0 field. The magnetization precesses about $\mathbf{B_1}$, with a driven Rabi frequency Ω_s, depending on the magnitude of $\mathbf{B_1}$ [72]. During the so-called $\pi/2$-pulse, the magnetization is rotated by 90° onto the -y-axis. In the lab frame, the precessing magnetization about $\mathbf{B_0}$ represents an oscillating dipole, which induces a microwave signal with a frequency of ω_s in the resonator, used to apply the pulse. Due to a finite spectral linewidth of the spin ensemble the magnetization dephases over time, resulting in an exponential decay of the induced microwave signal (see Fig. 4.8 (b)), known as free induction decay (FID, cf. Sec. 4.2.2). The finite linewidth originates from homogeneous and inhomogeneous broadenings of the ESR transition. The homogeneous broadening is caused by incoherent scattering processes, like spin-spin interactions or spin-lattice interactions, and the inhomogeneous broadening by dephasing processes, which can be caused by inhomo-

geneities in the static magnetic field [71, 72]. Both processes contribute to the reduction of the magnitude of the magnetization vector, due to deconstructive interference. Thereby, the incoherent processes lead ultimately to the loss of coherence. However, the dephasing processes can be reversed, since they manifest as a fan-out of individual packages of magnetic moments about the magnetization vector (cf. blue arrows in Fig. 4.8 (b)), having a symmetric distribution of packages with larger and smaller frequencies, relative to ω_s. To invert the dephasing processes, a second pulse is applied along the x-axis, after a time τ. This π-pulse is twice as long as the first pulse, and rotates the dephased magnetization vector by 180°, to the +y-axis (see Fig. 4.8 (c)). The inversion acts like a time reversal for the dephasing [72]. At the end of the π-pulse, the individual packages of magnetic moments start to evolve back to the +y-axis and convergences after another time of τ has elapsed (see Fig. 4.8 (d)). Similar to the induced decaying microwave signal, due to the FID after the first pulse, the refocusing magnetization induces a rising signal, here defined as a free induction rise (FIR). At a time 2τ after the first pulse the signal peaks and is followed again by a FID (cf. Fig. 4.8 (e)). The emerging signal peak, at the end of the pulse sequence, is known as a spin-echo (or a FIR-FID).

The spin-echo pulse sequence forms the basis of the following experiments, and permits an extraction of the T_1 and T_2 relaxation times. However, the preceding illustration is strictly only valid for a spin ensemble, weakly coupled to a resonator. For this situation, a vector description of the magnetization in a quantum mechanical framework is appropriate, since the magnetic quantum number is a good quantum number. This changes, when spin ensemble and resonator are in the strong coupling regime. Here, the two systems hybridize to a system with a new set of eigenstates and eigenvalues, where the good quantum number is given by the number of excitations, present in the coupled system (cf. Sec. 3.2). Although, the scalar nature of this quantity gives no information about the orientation of the magnetization, the spin ensemble still gets excited. The excitation is continuously exchanged between the spin ensemble and the resonator, at a rate defined by the collective coupling g_{eff}. Thus, the magnetization has to rotate also during this process, suggesting that the pulse sequences, known from pulsed ESR, are also applicable to a strongly coupled system. In the following, Hahn echo and inversion recovery pulse sequences are utilized to study the microwave resonator / phosphorus donor spin ensemble hybrid system. To determine the optimal pulse lengths for the experiments, first a pulse calibration is performed.

4.3.1 Pulse Calibration

To determine the optimal pulse length for an echo pulse sequence, typically a Rabi oscillation experiment is performed [72]. The integrated signal of a FID is investigated as a function of the length τ_P of preparation pulse. On resonance, the integrated signal of the FID performs a damped oscillation, with a period representing the pulse length for a 180° or π rotation of the magnetization. Alternatively, the Rabi oscillation can be detected via an echo generation sequence, which is applied after the preparation pulse. Equivalent to the integrated signal of the FID, the integrated echo signal performs also an oscillation. However, the results of an echo detected Rabi oscillation experiment on the hybrid system are not conclusive [113]. Figure 4.9 shows the integrated echo signal as a function of the preparation pulse length τ_P at a temperature of 50 mK, utilizing the CPWR. The oscil-

lating signal is heavily damped, preventing the observation of a full period of oscillation. The high damping is assumed to be introduced via the resonator. The coupling to the resonator provides an additional loss channel for the spin ensemble, resulting in increased damping [27, 34].

An alternative method to determine an optimal pulse length, is to maximize the emerging echo signal. The fundamental idea of this approach is the assumption of maximum echo signal gain, when most of the magnetization is rotated in the xy-plane (cf. Fig. 4.8). To this end, a series of echo pulse sequences is conducted, using different pulse length. Figure 4.10 (a) shows the transmitted microwave power I^2/I^2_{input} as a function of the pulse sequence time, starting with the rising etch of the first pulse. The pulse frequency is set to the resonance frequency ω_r of the CPWR and is tuned in resonance with the high field spin transition of the phosphorus donor spin ensemble, by the static magnetic field B_0. At a temperature of $50\,mK$ microwave pulses with an amplitude of $I^2_{input} = 2\,nW$ and differing length (see legend of Fig. 4.10 (a)), are applied to the resonator. For all sequences, the same evolution time of $\tau = 300\,\mu s$ and SRT of $500\,s$ are used. Around a time of 2τ an echo emerges for all four pulse sequences. For an improved distinction between the different echos, Fig. 4.10 (b) plots the microwave power transmission of only the echos, shown in (a). The echo amplitude increases with increasing pulse length and decreases again for the longest pulses. Since the Rabi oscillation experiments performed on the hybrid system could not produce a full rotation of the spin ensemble's magnetization, the reduction of the echo amplitude for the longest pulses is not attributed to a magnetization rotation beyond 90°. With increasing pulse length the spectral width of the microwave pulse is reduced. When the pulse's spectral width gets much smaller than the spectral distribution of the coupled spin ensemble, the corresponding echo signal is also reduced, as less spins can get excited by the pulse. For the sequence consisting of $2.5\,/\,5\,\mu s$ and $5\,/\,10\,\mu s$ long pulses, the largest echo amplitudes are generated. Comparing the integrated echo signal, subtracting a contribution of the background signal [113], the $5\,/\,10\,\mu s$ pulse sequence yielded $33.9\,pW\mu s$ and the $2.5\,/\,5\,\mu s$ sequence $21.5\,pW\mu s$. Thus, for the following Hahn echo and inversion recovery experiments a sequence, which applies $5\,/\,10\,\mu s$ long microwave pulses, is chosen. The same pulse length is utilized for the CPWR and the LER, since both
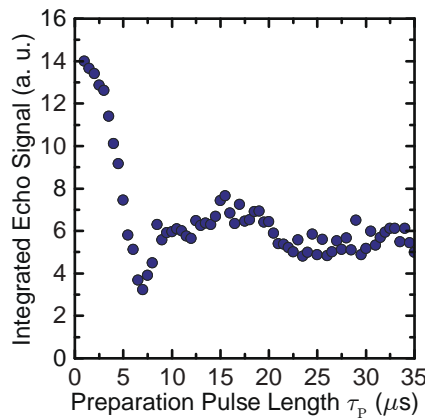
Figure 4.9: Echo detected Rabi oscillation, showing the integrated echo signal as a function of the preparation pulse length τ_P at $50\,mK$, using the CPWR. $5\,ms$ after the preparation pulse the echo generation pulse sequence is initiated, consisting of a $5\,\mu s$ and $10\,\mu s$ long microwave pulse separated by $100\,\mu s$ [113].
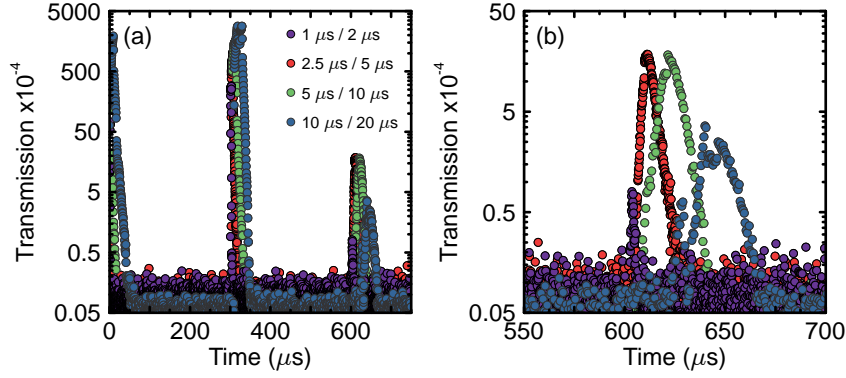
Figure 4.10: Logarithmic scaled microwave power transmission I^2/I^2_{input} of the CPWR as a function of the pulse sequence time, at a temperature of 50 mK and a pulse amplitude of $I^2_{input} = 2$ nW at the resonator. The pulse frequency matches the resonance frequency of the resonator and the high-field spin transition is tuned in resonance with the CPWR. (a) Microwave power transmission of the full pulse sequence for four traces, differing in pulse length and corresponding echo signal intensity (see legend). (b) Magnification of the microwave power transmission of (a), showing the time interval of the generated echos.

resonators exhibit similar quality factors, indicating that the same amount of microwave power is coupled in the resonator. Note, that each signal trace is recorded by applying the corresponding sequence only once. Due to the high spin polarization P (cf. Sec. 3.3.4), an excellent signal to noise ratio is achieved, rendering signal averaging unnecessary.

4.3.2 Hahn Echo Spectroscopy

Applying successive spin-echo pulse sequences, while increasing the evolution time τ for each sequence, the coherence time T_2 can be determined [72, 124]. In such a Hahn echo experiment, the echo signal decreases with increasing τ, as shown schematically in Fig. 4.11. The microwave transmission I/I_{input} of the echo signal, induced after each successive pulse sequence in the resonator, shows an exponential decay with increasing τ

$$\frac{I(\tau)}{I_{input}} \propto e^{-\frac{2\tau}{T_2}} . \tag{4.5}$$

The characteristic time constant of this decay corresponds to the coherence time T_2. Note, that the decay of the echo signal as a function of the evolution time can have additional contributions, due to relaxation processes like spectral diffusion or instantaneous diffusion [4, 72] (cf. Sec. 4.3.2). Using Hahn echo spectroscopy, the coupled microwave resonator / phosphorus donor spin ensemble system is studied, in respect of determining its coherence time. First, similar prepared phosphorus doped ^{28}Si crystals (cf. Sec. 2.2.2) are also investigated in a commercial Bruker electron spin resonance spectrometer, to obtain a reference, where the spin ensemble is only weakly coupled to a resonator.

Conventional Hahn Echo Spectroscopy

The phosphorus doped ^{28}Si crystals are studied in a commercial Bruker Elexsys E580 X-band spectrometer [3, 114], for temperatures ranging from 6 K to 15 K. The length of the applied pulses is calibrated by Rabi oscillation measurements. For a spectroscopic analysis of the ESR spin transitions, an echo detected field sweep is performed. Figure 4.12 shows
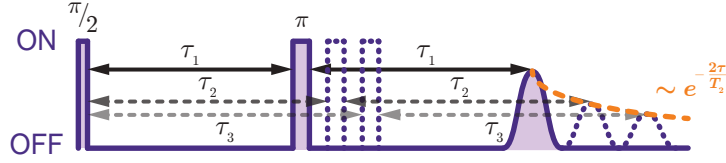
Figure 4.11: Schematic spin-echo pulse sequence. Repeatedly applying the sequence, while increasing the evolution time τ, results in a decreasing echo signal. The characteristic time constant of the decreasing echo signal corresponds to the coherence time T_2.

an acquired spectrum of the high-field spin transition, for a temperature of 8 K. Here, at each magnetic field point a spin-echo pulse sequence is applied and the integrated echo signal is detected via a magnitude detection method, similar to the method discussed in Ref. [125]. By fitting a lorentzian function to the resonance peak in Fig. 4.12 a full width at half maximum of $\Delta B_{\text{Bruker}} = 37.7\,\mu\text{T}$ is found. The spin resonance linewidth translates to a spin loss rate via Eq. (2.17) of $\gamma_{\text{Bruker}}/2\pi = 530\,\text{kHz}$. This result is nearly a factor of three smaller, than the loss rate extracted from the CW spectroscopy on the CPWR of $\gamma/2\pi = 1.40\,\text{MHz}$ (cf. Sec. 3.3). Therefore, the result consolidates the assumption, that the spin resonance line broadening originates from static magnetic field inhomogeneities.

The Hahn echo spectroscopy is conducted in resonance with the high-field spin transition, prior determined by an echo detected field sweep. Using again the magnitude detection method for signal acquisition, the integrated echo signal is measured as a function of the evolution time τ, at different temperatures. The T_2 time is determined by fitting an exponential function to the recorded echo signal (cf. Eq. (4.5)), exemplary shown in Fig. 4.13 (a). Figure 4.13 (b) shows the resulting T_2 as a function of temperature, for the ^{28}Si crystals doped with a phosphorus donor concentration of $[\text{P}] = 1 \times 10^{17}\,\text{cm}^{-3}$. For comparison, the in Ref. [4] reported coherence times for ^{28}Si crystals with $[\text{P}] = 1 \times 10^{16}\,\text{cm}^{-3}$ and $[\text{P}] = 1 \times 10^{15}\,\text{cm}^{-3}$ are additionally included in Fig. 4.13 (b). For all three concentrations, the coherence times increase with decreasing temperature and saturates at low temperatures. In the high temperature regime T_2 is limited by the longitudinal relaxation time T_1, which is dominated by resonance fluorescence by phonons and two phonon Raman and Orbach processes in this temperature regime [115, 116, 126] (cf. Sec. 4.3.3). At low temperatures T_2 saturates on a value of 28 µs, limited due to the phosphorus donor
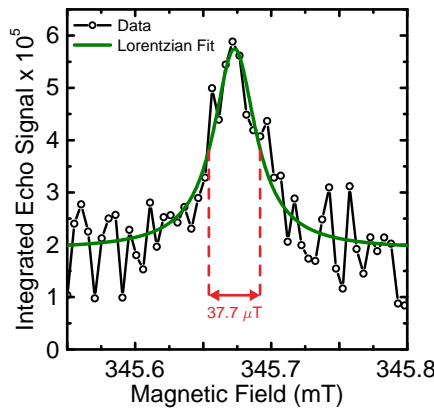
Figure 4.12: Echo detected magnetic field sweep of the high field phosphorus donor spin resonance.
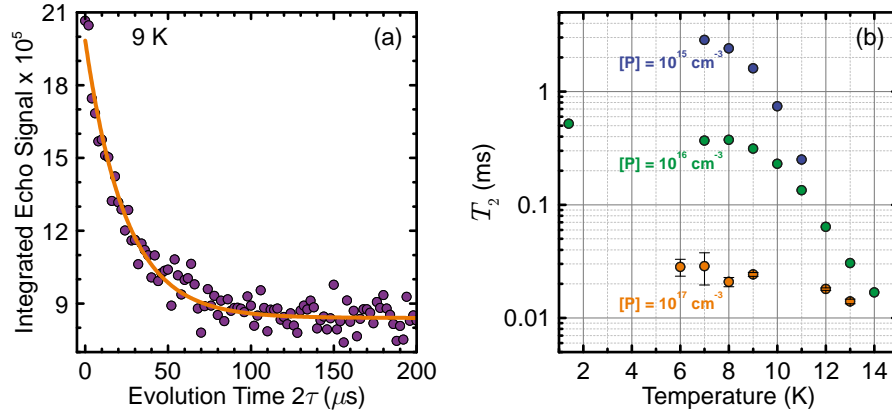
Figure 4.13: (a) Integrated echo signal as a function of twice the evolution time τ (symbols), recorded in a conventional pulse ESR setup at a temperature of $9\,\mathrm{K}$. The echos signal decrease is fitted with an exponential decay (solid line), to extract the characteristic time constant T_2. (b) Logarithmic scaled coherence time T_2 as a function of temperature. The orange symbols are measurement results on the $^{28}\mathrm{Si}$ crystals doped with a phosphorus donor concentration of $[\mathrm{P}] = 1 \times 10^{17}\,\mathrm{cm}^{-3}$, investigated in this thesis. The green and blue symbols are taken from Ref. [4] for comparison.

concentration [4]. Comparing the measured coherence time with the data from Ref. [4] shows the expected inverse proportionality to [P], additionally confirming the phosphorus donor concentration of the investigated $^{28}\mathrm{Si}$ crystals. In this temperature regime, the main mechanism of decoherence is instantaneous diffusion, a process coming along with the application of a microwave pulse [4,72]. By exciting spins via a microwave pulse, the local dipole fields observed by individual spins is changed. Due to the statistical distribution of the spins, the change in the local dipole fields can be different for each spin. As a result, some of the excited spins are shifted in resonance frequency after the pulse, due to the change of their local field environment. Thus, during the pulse a (instantaneous) spin diffusion occurs, which results in an overall reduction of resonant spins contributing to a detectable signal. Considering the spin-echo pulse sequence, the second pulse refocuses the dispersed magnetization of the spin ensemble, leading to the echo generation (see. Sec. 4.3). If all spins are inverted by the refocusing pulse the inversion is also accompanied by a large change in local dipole fields, resulting in a large contribution to instantaneous diffusion. For an ensemble of spins, this process leads also to an exponential echo signal decay, as in Eq. (4.5) [4]. To overcome this effect, the refocusing pulse is shortened, reducing the amount of spins being inverted simultaneously and consequently the amount of local dipole field changes [4]. As a consequence, the echo signal intensity is reduced with the reduction of the length of the second pulse, with a vanishing echo signal for an infinitely short pulse. The influence of instantaneous diffusion is also discussed for the millikelvin Hahn echo spectroscopy results in Sec. 4.3.2.

The results obtained for T_2 in the conventional pulse ESR setup are in good agreement with the expectations, when compared to current results in literature. They serve as a point of reference for the discussion of the coherence time of the strongly coupled microwave resonator / spin ensemble hybrid system.

Millikelvin Hahn Echo Spectroscopy

The coupled microwave resonator / phosphorus donor spin ensemble hybrid system is studied in the cryogen free dilution refrigerator setup (cf. Sec. 2.3.1), applying the in Sec. 4.3.1 determined spin-echo pulse sequence. The Hahn echo spectroscopy is conducted using both CPWR and LER to provide the microwave pulses. The high-field spin transition of the spin ensemble is tuned into resonance with the resonator, determining the degeneracy point of the two subsystems by CW spectroscopy (cf. Sec. 3.3.1 or 3.4.1). The microwave pulses are applied at the center frequency of the normal mode splitting of the resonator transmission spectrum ($\omega_{\mathrm{r}} = \omega_{\mathrm{s,HF}}$), where the splitting is given by twice the collective coupling strength $2g_{\mathrm{eff}}$. For the experiments involving the CPWR, its first harmonic mode is utilized and in the case of the LER experiments, resonator B is used.

Figure 4.14 shows the microwave transmission I^2/I^2_{input} of the CPWR as a function of the spin-echo pulse sequence time, at a temperature of 50 mK. In addition, a schematic of the pulse sequence is depicted to illustrate the signal trace. The sequence consists of a 5 µs and 10 µs long microwave pulses, separated by an evolution time of $\tau = 110$ µs. The echo occurs at a time of 240 µs, which is delayed with respect to the expected time of $2\tau + 5\,\mu\mathrm{s} + 10\,\mu\mathrm{s} = 235\,\mu\mathrm{s}$. However, for the broad line case the emerging echo is known to be delayed, suggesting that the spectral linewidth of the transition is broader than the spectral linewidth of the applied microwave pulses [127].

From the linear microwave transmission I/I_{input} ($\propto V$) of the Hahn echo spectroscopy, the integrated echo signal is extracted at $T = 50$ mK and plotted as a function of twice the evolution time 2τ in Fig. 4.15 (a) and (b), for the CPWR and the LER, respectively. The integrated echo signal decreases for both resonator types, however, only for the LER data the signal decreases exponentially, as given in Eq. (4.5). The CPWR data shows an additional quadratic exponential decay, which indicates a contribution from spectral diffusion to the echo decay [72, 128–130]. In pulsed ESR, spectral diffusion can arise if the
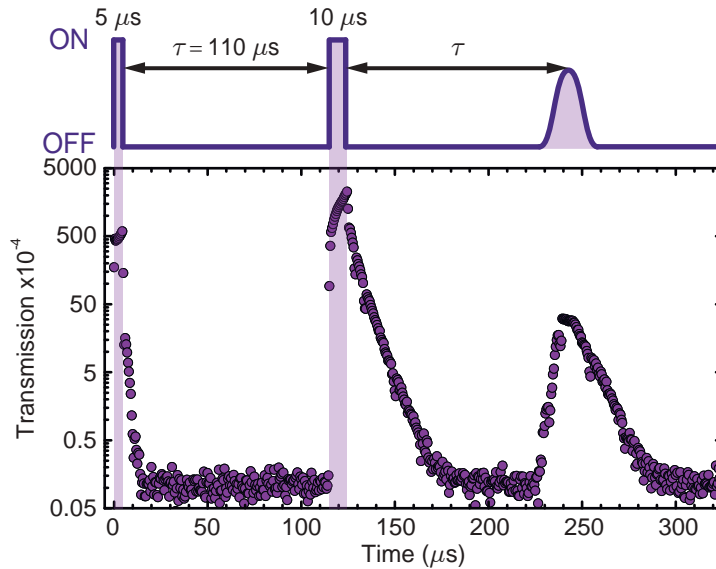
Figure 4.14: CPWR microwave transmission I^2/I^2_{input} as a function of the sequence time, for a temperature of 50 mK and $I^2_{\mathrm{input}} = 2$ nW. The measurement trace is additionally illustrated by a schematic of the applied pulse sequence, highlighting the microwave pulses.
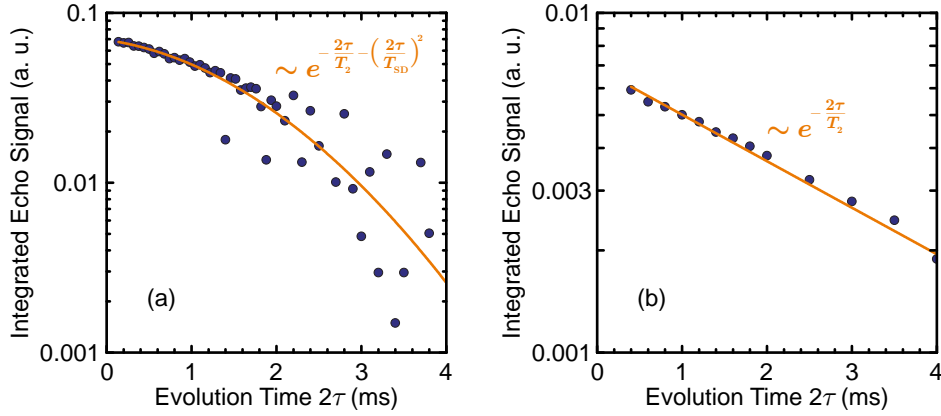
Figure 4.15: Logarithmic scaled integrated echo signal as a function of twice the evolution time τ obtained from a Hahn echo spectroscopy on the hybrid system at $50\,\mathrm{mK}$, using the CPWR and LER (symbols in (a) and (b), respectively). The solid lines represent a fit to the decaying echo signal, with the proportionality given in plot.

spectral linewidth of the microwave pulses is smaller than the spectral linewidth of the spin ensemble, a condition which is also supported by the delayed echo manifestation. In this case, only part of the (inhomogeneous) spectral distribution of the ensemble gets excited by the pulse. If the thermal energy is larger than the Zeeman splitting, T_1 processes accompanied by spin-spin interactions in the unexcited part of the spectrum result in local field fluctuations, which influence the excited spins. The fluctuating fields lead to an exchange of excited and equilibrium spins, transferring excitation to parts of the spectrum, which is not in the detection bandwidth. As a consequence, this diffusion process reduces the generated echo signal [72]. For the case where the thermal energy is smaller than the Zeeman splitting, spin-spin interactions between equilibrium spins and excited spins can still occur, resulting also in a diffusion of excited spins. Thus, spectral diffusion adds to the transverse relaxation of the spin ensemble, which leads to an additional quadratic term for the echo signal decay [129, 130]

$$\frac{I(\tau)}{I_{\mathrm{input}}} \propto e^{-\frac{2\tau}{T_2} - \left(\frac{2\tau}{T_{\mathrm{SD}}}\right)^2} , \tag{4.6}$$

where T_{SD} gives the characteristic time constant of the spectral diffusion process. The fact, that this contribution is only observed in the CPWR experiments and not for the measurements using the LER, suggests that the inhomogeneous broadening of the spin resonance line, found for the CPWR CW spectroscopy in Sec. 3.3.3, is also influencing the Hahn echo spectroscopy.

For the CPWR / spin ensemble hybrid system a coherence time of $T_{2,\mathrm{CPWR}} = 4.65\,\mathrm{ms} \pm 1.7\,\mathrm{ms}$ is found, which is limited to $T_{\mathrm{SD}} = 2.47\,\mathrm{ms} \pm 0.26\,\mathrm{ms}$, due to spectral diffusion. Using the LER, a coherence time of $T_{2,\mathrm{LER}} = 3.24\,\mathrm{ms} \pm 0.08\,\mathrm{ms}$ is extracted from the echo decay. The found T_2 times are about three orders of magnitude longer, than the by conventional pulse ESR determined coherence time of $28\,\mathrm{\mu s}$ at a temperature of $8\,\mathrm{K}$ (cf. Sec. 4.3.2). To discern the origin of the enhancement a temperature series is conducted, to allow a better connection of the data from the two measuement setups.

Prior to each Hahn echo spectroscopy at the different temperatures, the degeneracy point of the microwave resonator dispersion and the high-field spin transition dispersion
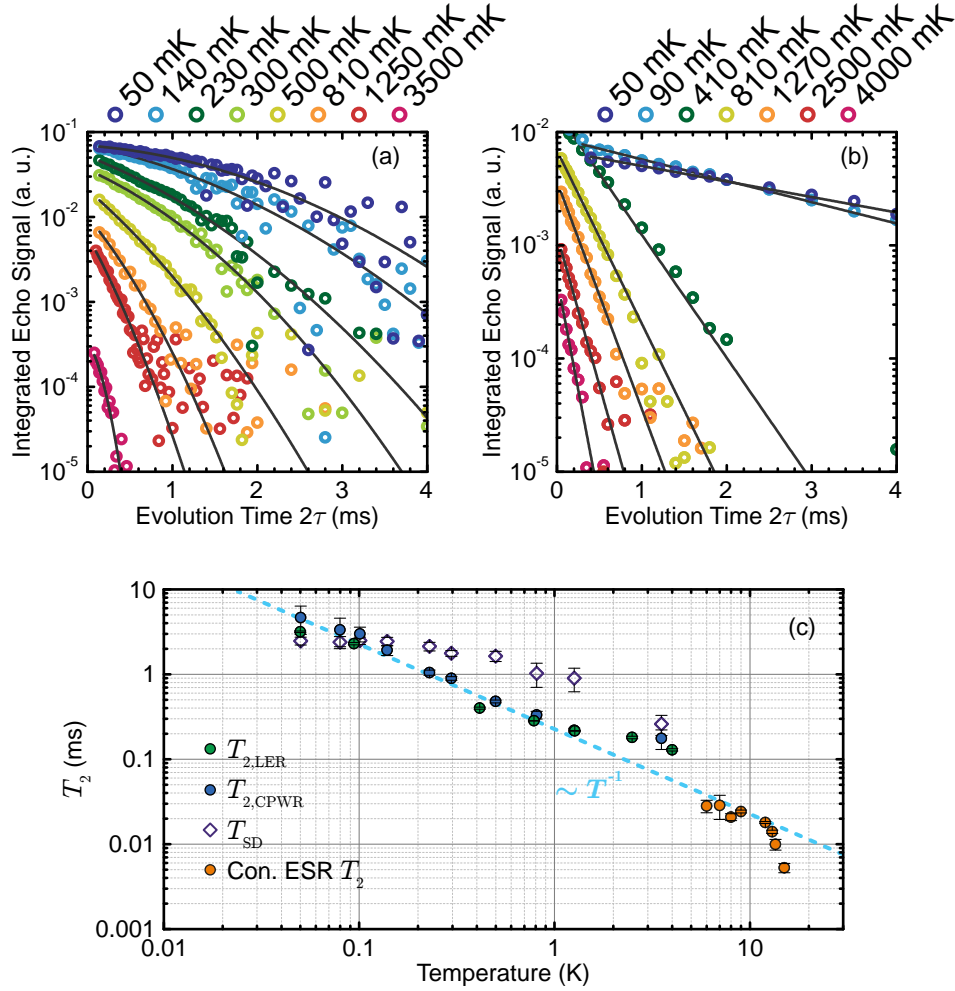
Figure 4.16: (a) and (b) Logarithmic scaled integrated echo signal (symbols) as a function of twice the evolution time τ obtained from a Hahn echo spectroscopy on the hybrid system for temperatures ranging from $50\,\text{mK}$ up to $4\,\text{K}$ (see legend), utilizing the CPWR and the LER, respectively. The solid lines represent fits to the data, using an exponential decay function. Note, that the echo signal decay from the CPWR exhibits an additional quadratic exponential decay, as given in Eq. (4.6), while the LER data follows a single exponential decay, as given in Eq. (4.5). (c) Extracted coherence times $T_{2,\text{CPWR}}$ and $T_{2,\text{LER}}$ as a function of temperature, using a double logarithmic scaling. Additionally, the time constant T_{SD} of the in the CPWR experiments observed spectral diffusion process, as well as the T_2 time determined by conventional pulse ESR (see Sec. 4.3.2) are included in (c) (see legend). For low temperatures, the hybrid system's coherence times follow a T^{-1} temperature dependence, indicated by the blue dashed line.

is determined by CW spectroscopy, at which the pulses are applied. Also, the T_1 time is measured in advance, for an optimization of the SRT (cf. Sec. 4.3.3). The at the different temperatures obtained integrated echo signal decays are shown in Fig. 4.16 (a) and (b), for the CPWR and the LER, respectively. For both resonator designs the signal decay becomes faster with increasing temperature. For the CPWR / spin ensemble hybrid system, a contribution from spectral diffusion can be observed at all temperatures, while for the coupled LER / spin ensemble system the decay follows a single exponential for all temperatures (cf. fits (solid lines) in Fig. 4.16 (a) and (b)). The time constants are determined by fitting the decaying echo signal with the corresponding functions (see Fig. 4.15), summa-

rizing the results in Fig. 4.16 (c). For comparison, the T_2 time obtained in the conventional pulse ESR setup is also included. At the lowest temperature of 50 mK, the longest coherence time and spectral diffusion time constant is observed. Upon temperature increase the coherence times $T_{2,\mathrm{CPWR}}$ and $T_{2,\mathrm{LER}}$ decrease, exhibiting a T^{-1} dependence (see dashed line in Fig. 4.16 (c)). T_{SD} stays constant within the error margin, up to about a temperature of 240 mK, which corresponds to the Zeeman splitting of the high-field spin transition. Above this temperature, T_1 processes begin to contribute to the spectral diffusion process, further reducing the respective time constant. However, the decrease of T_{SD} with increasing temperature is slower, than the decrease of $T_{2,\mathrm{CPWR}}$. At about 140 mK the two time constants are of equal magnitude and for higher temperatures spectral diffusion is no longer the limiting mechanism for the coherence time of the hybrid system. When the trend for both T_2 temperature series is extrapolated qualitatively, it would intersect with the results from the conventional pulse ESR setup at about 10 K. From this temperature on T_2 is limited by T_1 processes. However, above 1.5 K the found T_2 times no longer follow this trend. The dependence on temperature is reduced, but the data obtained so far is inconclusive about, whether this is a change in dependence or an overall onset of saturation. In this temperature regime, the thermal spin polarization is small, as well as the quality factor of the microwave resonator is reduced, due to the degradation of the superconduction. Consequently, the observed echo amplitudes are small, making a Hahn echo spectroscopy more challenging. Nevertheless, the data from both measurement setups can be connect qualitatively. From the conducted temperature series two mechanisms are suggested, which are attributed to the coherence time enhancement. In the following, a reduction of instantaneous diffusion and the collective coupling between microwave resonator and spin ensemble are discussed as possible sources for this enhancement.

Instantaneous diffusion describes the spin diffusion due to changes in local dipole fields, induced by pulse excitation of the spin ensemble (see Sec. 4.3.2). A method to overcome instantaneous diffusion in spin-echo pulse sequences is to reduce the angle Θ_2 by which the spin ensemble's magnetization is rotated by the refocusing pulse [4, 72]. In this context, the instantaneous diffusion time constant T_{ID} is given by [4]

$$T_{\mathrm{ID}} = \frac{8h}{5\mu_0 \left(g_{\mathrm{eP}}\mu_{\mathrm{B}}\right)^2} \frac{1}{[\mathrm{P}]} \sin^{-2}\left(\Theta_2/2\right). \tag{4.7}$$

Assuming a standard spin-echo pulse sequence, with $\Theta_2 = 180°$ and a phosphorus donor concentration of $[\mathrm{P}] = 1 \times 10^{17}\,\mathrm{cm}^{-3}$, Eq. (4.7) yields $T_{\mathrm{ID}} = 24.6\,\mu\mathrm{s}$. The result is in good agreement with the by conventional pulse ESR found coherence time of 28 μs at 8 K (cf. Sec 4.3.2). To achieve an enhancement of about three orders of magnitude to either $T_{2,\mathrm{CPWR}} = 4.65\,\mathrm{ms}$ or $T_{2,\mathrm{LER}} = 3.24\,\mathrm{ms}$, a theoretical rotation angle of 9° or 10° would be required, respectively.

Reducing the rotation angle Θ_2 is equivalent to a reduction of the absolute number of flipped spins. The coupled microwave resonator / spin ensemble system provides an alternative way to modify the number of excited spins. By changing the collective coupling g_{eff}, the spectral overlap A of the pulse bandwidth with the spectral distribution of the hybrid system can be tuned, whereas pulse amplitude and pulse length are held constant. To this end, spin ensemble and resonator are tuned in resonance ($\omega_{\mathrm{r}} = \omega_{\mathrm{s}}$). The frequency of the applied pulses is fixed to ω_{r}, while the spectral overlap is tuned by changing g_{eff}, e.g. due to temperature (cf. Sec. 3.3.4). Figure 4.17 (a) plots three theoretical CW transmission
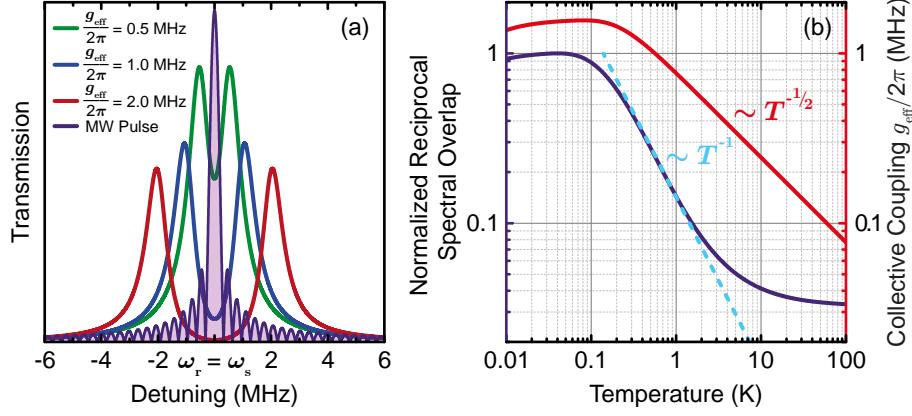
Figure 4.17: (a) Calculated CW transmission spectra of a hybrid system as a function of the detuning from the degeneracy point ($\omega_r = \omega_s$), for three different collective couplings g_{eff} (see legend). The spectra are calculated using Eq. (3.44), where $\kappa_0/2\pi = 400\,\text{kHz}$ and $\gamma/2\pi = 500\,\text{kHz}$. All three spectra are normalized on the uncoupled resonator transmission. At the resonance frequency the spectral distribution of a 500 ns long, rectangular microwave pulse is shown (purple line), which is rescaled to be of comparable amplitude as the hybrid system spectra. Note, that the length of the pulse is chosen shorter than in the actual experiment to improve visibility. (b) Logarithmic scaled normalized reciprocal spectral overlap $1/A$ (left axis) as a function of the logarithmic scaled temperature. For calculating the spectral overlap between the hybrid system's spectrum and the spectral distribution of the pulse, a 10 µs long, rectangular microwave pulse is assumed. For comparison, the in Sec. 3.3.4 derived model function, describing the temperature dependence for the collective coupling g_{eff} of the high-field spin transition (right axis), is also plotted.

spectra of a hybrid system as a function of the detuning from the degeneracy point ($\omega_r = \omega_s$) with differing g_{eff}, all normalized on the uncoupled resonator transmission. In addition, the spectral distribution of a rectangular pulse is included, to illustrate the change in spectral overlap A of the hybrid system and pulse for the different collective coupling strength. As g_{eff} is increased the spectral distribution of the pulse covers less of the spectrum of the hybrid system. The power transferred into the spin ensemble is also reduced and consequently the number of flipped spins. As a result, the contribution from instantaneous diffusion gets suppressed.

In Section 3.3.4 the temperature dependence of the collective coupling g_{eff} is investigated. The dependence is described via the thermal spin polarization of the spin ensemble, derived from the thermal population of the energy levels of the phosphorus donor spin system. Using the found temperature dependence for g_{eff} the spectrum of the hybrid system is calculated using Eq. (3.44). The resonance frequencies are fixed to the degeneracy point and $\kappa_0/2\pi = 400\,\text{kHz}$ and $\gamma/2\pi = 500\,\text{kHz}$ are assumed. Finally, the spectral overlap A between a 10 µs long microwave pulse and the hybrid system spectra is determined as a function of temperature. Figure 4.17 (b) shows the resulting spectral overlap, which is plotted normalized and reciprocal to allow a better comparison to the additionally included model function describing the temperature dependence for the collective coupling of the high-field spin transition (see Sec. 3.3.4). Up to a temperature of about 1.5 K the inverse spectral overlap $1/A$ follows a similar temperature dependence as g_{eff}. A comparison of the temperature regimes where both curves exhibit a T^{-x} power-law dependence (see Fig 4.17 (b)), shows that $1/A \propto g_{\text{eff}}^2$. This proportionality holds as long as the two peaks of the resonator's normal mode splitting are fully separated ($g_{\text{eff}} > \kappa_0, \gamma$). When the

two peaks start two merge ($g_{\text{eff}} < \kappa_0$ or γ), the inverse spectral overlap $1/A$ becomes less dependent on temperature, until it gets constant for the limit when $g_{\text{eff}} \ll \kappa_0, \gamma$.

The found temperature dependence of $1/A$ resembles the experimentally observed dependence of the coherence time over a large temperature range. Therefore, the assumption that the reduction of the spectral overlap has an equivalent influence on instantaneous diffusion as the reduction of the rotation angle Θ_2 of the refocusing pulse is confirmed. This allows to establish the following proportionality for the instantaneous diffusion time constant T_{ID},

$$T_{\text{ID}} \propto \frac{1}{\sin^2(\Theta_2/2)} \propto \frac{1}{A} \propto g_{\text{eff}}^2. \tag{4.8}$$

The result can describe the temperature dependence of the hybrid system's coherence time qualitatively, for temperatures above $200\,\text{mK}$. The T^{-1} dependence is in good agreement with the experimental findings, as well as the transition to a weaker dependence on temperature at about $1.5\,\text{K}$. For temperatures below $200\,\text{mK}$ the suggested proportionality of $T_{\text{ID}} \propto g_{\text{eff}}^2$ no longer describes the experimental data, from either the CPWR or the LER. The data continuous to follow the T^{-1} dependence in this temperature regime (cf. Fig. 4.16 (c)), while T_{ID} reaches a maximum at about $40\,\text{mK}$, subsequently followed by a decrease of T_{ID} with decreasing temperature. Since amplitude, duration and frequency of the applied microwave pulses are kept constant for the conducted experiments, only the change in spectral overlap could influence the energy transferred to the spin ensemble and consequently the instantaneous diffusion process, corroborating that T_{ID} is proportional to g_{eff}^2. However, the discrepancy between the measured T_2 times and the expected dependence of T_{ID} on temperature, suggests that instantaneous diffusion is not the dominating mechanism of decoherence for the hybrid system.

To verify, whether instantaneous diffusion is limiting the coherence time of the investigated hybrid system below $200\,\text{mK}$, Hahn echo spectroscopy experiments are performed, using pulse frequencies deviating from the frequency of the degeneracy point, where $\omega_r = \omega_s$. Following the preceding argument of increasing instantaneous diffusion with increasing spectral overlap of the microwave pulse and the hybrid system's spectrum. Therefore, a pulse applied at the frequency of one of the two peaks of the resonator's split normal mode, would result in a significantly larger spectral overlap. Due to the larger overlap T_{ID} is reduced, as well as the overall coherence time, for when instantaneous diffusion is dominating the coherence. At a temperature of $50\,\text{mK}$ a Hahn echo spectroscopy is conducted on the LER / spin ensemble hybrid system for different static magnetic fields and pulse frequencies. Note, that for each magnetic field value, the superconducting magnet is set into the persistent current mode to reduce magnetic field fluctuations. The coherence time T_2 is determined for the upper and lower branch of the avoided crossing at the high-field spin transition, as well as for the frequency center of mass between upper and lower branch. Figure 4.18 (a) shows the CW microwave transmission $|S_{21}|^2$ of LER B, coupled to the phosphorus donor high-field spin transition as a function of the VNA frequency and the static magnetic field, at $T = 50\,\text{mK}$ (cf. Sec. 3.4). The frequency and magnetic field values, at which a Hahn echo spectroscopy is performed, are indicated by the symbols in Fig. 4.18 (a). The applied spin-echo pulse sequence uses the in Sec. 4.3.1 determined pulse amplitude and length.

The resulting coherence times for the upper and lower branches and their respective frequency center of mass, are shown in Fig. 4.18 (b) as a function of static magnetic field.
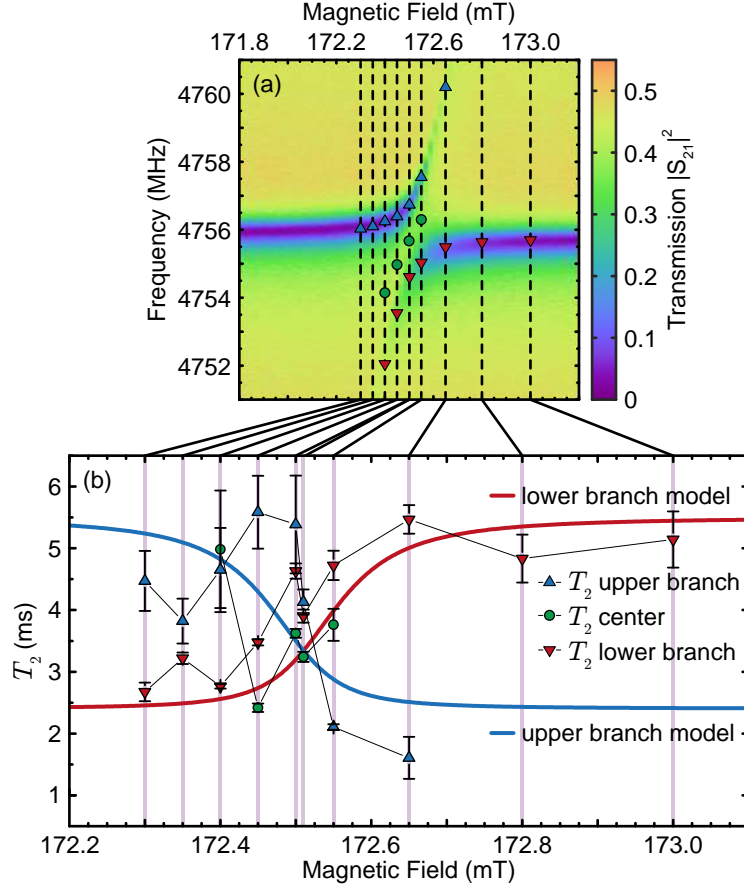
Figure 4.18: (a) Color encoded microwave transmission data $|S_{21}|^2$ as a function of the VNA frequency and the magnetic field B_0. The central line of low transmission indicates the resonance frequency dispersion of the LER, which is interrupted by an avoided crossing at $B_{0,\mathrm{HF}} = 172.54\,\mathrm{mT}$, indicating the interaction between the microwave resonator and the high-field spin transition of the phosphorus donor spin ensemble (cf. Sec. 3.4). The vertical dashed lines indicate the static magnetic field values, at which a Hahn echo spectroscopy is performed, and the symbols indicate the used pulse frequencies. (b) Coherence time T_2 as a function of the static magnetic field determined on the upper branch (blue symbols) and the lower branch (red symbols) of the avoided crossing, as well as on the frequency center of mass of the upper and lower branch (green symbols). The solid lines represent a model function, calculated using the imaginary part of the eigenenergies of the Tavis-Cummings model, given in Eq.(3.36) (see text for more details).

Not at every static magnetic field and pulse frequency a Hahn echo spectroscopy is conducted, as the signal intensities are reduced for a large detuning from the microwave resonator's resonance frequency ω_r. Note, that there is a small difference in resonance frequencies between the two measurements, shown in Fig. 4.18 (a) and (b). For the CW microwave transmission spectroscopy, the degeneracy point is found at a static magnetic field of 172.54 mT, while it is located at 172.51 mT for the Hahn echo spectroscopy series. The finite difference is attributed to magnetic hysteresis effects of the superconducting microwave resonator, due to static magnetic field sweeps performed between the two measurements [118]. At the degeneracy point, the coherence times obtained for the lower and upper branch are $T_{2,\triangledown} = 3.9\,\mathrm{ms} \pm 0.1\mathrm{ms}$ and $T_{2,\triangle} = 4.13\,\mathrm{ms} \pm 0.2\mathrm{ms}$, respectively. The found times are more than 20 % longer, than the time extracted at the frequency center of $T_{2,\bigcirc} = 3.24\,\mathrm{ms} \pm 0.08\,\mathrm{ms}$, which is not expected from instantaneous diffusion. Here,

a decrease in T_2 would have been expected, due to the larger spectral overlap, when the pulse frequency is centered on one of the two branches of the avoided crossing. Therefore, the findings suggest, that instantaneous diffusion is not limiting the coherence time of the hybrid system, at temperatures of $50\,\mathrm{mK}$.

Tuning the static magnetic field away from the degeneracy point reveals a considerable dependence on the magnetic field. $T_{2,\triangle}$ is longest for magnetic fields smaller than the field of the degeneracy point of $172.51\,\mathrm{mT}$, and shortest for larger magnetic fields. $T_{2,\triangledown}$ exhibits an inverse dependence, intersecting with $T_{2,\triangle}$ at the degeneracy point. Thus, the coherence time of the hybrid system is increased the more resonator-like a branch becomes and decreased when its characteristic becomes more spin-like. Note, that at $B_0 = 173\,\mathrm{mT}$ a Hahn echo spectroscopy is still possible to conduct, despite the large detuning of resonator and spin ensemble resonance frequency of about $15\,\mathrm{MHz}$. The found collective coupling between the high-field spin transition and the microwave resonator is $g_{\mathrm{eff,HF}}/2\pi = 1.23\,\mathrm{MHz}$ (see Sec. 3.4.1), which is more than a factor of ten smaller than the resonance frequency detuning at $B_0 = 173\,\mathrm{mT}$. Thus, even at this large detunings, the two sub-systems can not be considered completely uncoupled. Assuming $T_{2,\triangle}$ and $T_{2,\triangledown}$ saturate for a large detuning of the static magnetic field, the behavior can be modeled qualitatively, by the eigenstates of the Tavis-Cummings model (see Sec. 3.2.3). Thereby, Eq. (3.36) describes the complex eigenenergies $E_{\mathrm{u}_{/l}}$ for the upper and lower branch of the avoided crossing. $|\Im(E_{\mathrm{u}_{/l}})/\hbar|$ gives the loss rate evolution of the microwave resonator κ_0 and the spin ensemble γ over the course of the avoided crossing. Here, the respective effective loss rates are defined by the coherence times, on which the upper and lower branches saturate, assuming $5.5\,\mathrm{ms}$ and $2.4\,\mathrm{ms}$, respectively. These times are translated via Eq. (4.2) to a respective effective resonator-like loss rate of $\kappa_{\mathrm{eff}}/2\pi = 31.83\,\mathrm{Hz}$ and a respective spin ensemble loss rate of $\gamma_{\mathrm{eff}}/2\pi = 66.31\,\mathrm{Hz}$. The respective effective loss rates used in this model are not representing the loss rates of the individual uncoupled sub-systems. They rather correspond to a decoherence rate of the hybrid system in its resonator-like or spin-like limits. Inserting the effective loss rates in Eq. (3.36), together with the in Sec. 3.4.1 determined parameters for the resonator resonance frequency $\omega_{\mathrm{r}}/2\pi = 4.756\,\mathrm{GHz}$ and the collective coupling $g_{\mathrm{eff,HF}}/2\pi = 1.23\,\mathrm{MHz}$, their corresponding evolution is calculated. The result is translated in a coherence time evolution via

$$T_{2,\triangle\,/\,\triangledown} = \frac{\hbar}{|\Im(E_{\mathrm{u}_{/l}})|}, \qquad (4.9)$$

represented by the solid lines in Fig. 4.18 (b). The model can qualitatively describe the evolution of the coherence times determined on the two branches of the avoided crossings. Note, that the modeling assumes no incoherent coupling g_{inco}, as in the discussion on the asymmetric linewidth of the normal mode splitting in Sec. 3.4.2. Since a Hahn echo spectroscopy compensates for inhomogeneous broadening effects, the incoherent coupling is assumed to be also compensated by this measurement technique. The differing coherence times determined in the two limits of the hybrid system, gives information about the dominating decoherence mechanism. The two limits exhibit a considerable difference in their static magnetic field dispersion (cf. Fig. 4.18 (a)). The more spin-like the hybrid system becomes, the steeper gets its dispersion, approaching the dispersion relation of the uncoupled high-field electron spin transition (see Sec. 2.2.1). In this regime, the hybrid system is more susceptible to fluctuations in the static magnetic field. These translate via

the Zeeman interaction in a fluctuation of the spin ensemble's resonance frequency, which results in an increased decoherence rate [11, 131]. Although, the superconducting magnet system is operated in the persistent current mode, small fluctuations in the set field can still occur. These can be attributed to flux creep in the superconducting solenoid, or to mechanical vibrations of the magnet itself, induced by an incomplete decoupling from the vibrations caused by the pulse tube cooler. In contrast, the influence of the static magnetic field fluctuations on the coherence time decreases, as the coupled system becomes more resonator-like. Here, the hybrid system approaches the static magnetic field dispersion of the uncoupled microwave resonator, which can be assumed independent of the magnetic field within this small field region (cf. Fig. 4.18 (a)). Due to the almost vanishing slope of the dispersion, the hybrid system is more robust against magnetic field fluctuations, resulting in a longer coherence time. As the spin-like and the resonator-like limit approaches a dispersion with a constant slope, also the respective coherence times settle on a constant value, which is shown qualitatively by the experimental data. Therefore, the experimental findings corroborate, that at a temperature of $50\,\mathrm{mK}$ fluctuations in the static magnetic field are the dominating source of decoherence for the studied coupled microwave resonator / spin ensemble system. Additionally, due to the found dependence of the coherence time on the magnetic field and the pulse frequency, instantaneous diffusion can be ruled out as the limiting decoherence mechanism.

For concluding the discussion about the hybrid system's coherence time, the dependence of the T_2 time on the high-field cooperativity C_{HF} is analyzed. Note, that each $T_2(C_{\mathrm{HF}})$ is determined at an equal temperature. Figure 4.19 plots the coherence time, extracted at the degeneracy point of the microwave resonator and the high-field spin transition, as a function of the high-field cooperativity, using a double logarithmic scaling. Here, the $T_{2,\mathrm{CPWR}}$ time from the CPWR / spin ensemble hybrid system is plotted for two different cooperativities. As given in Eq. (3.45), the cooperativity is defined by the collective coupling g_{eff} , the microwave resonator loss rate κ_0 and the spin ensemble loss rate γ. For one data series, C_{HF} is calculated using the spin loss rate γ_{HF}, obtained by fitting Eq. (3.46) to the resonator transmission $|S_{21}|^2$, at the static magnetic field of the high-field spin transition (see Sec. 3.3.1). For the other data series, the by conventional pulse ESR determined spin loss rate γ_{Bruker} is utilized for the calculation (see Sec. 3.3.3). As discussed in Sec. 3.3.3, the found γ_{HF} is larger than expected from the phosphorus doped $^{28}\mathrm{Si}$ crystal. The increased loss rate is attributed to an inhomogeneous broadening of the electron spin resonance line, due to an effect of the inhomogeneous the static magnetic field on the large sample. Reference measurements in a commercial Bruker ESR spectrometer verified the assumption, yielding the smaller loss rate γ_{Bruker} (see Sec. 4.3.2). Additionally, γ_{Bruker} is of similar magnitude, as the loss rate found for the LER / spin ensemble hybrid system, for which no influence of inhomogeneous broadening on the resonance line is observed, due to the smaller sample used. As a result, the data series $T_{2,\mathrm{CPWR}}(C_{\mathrm{HF}})$, using γ_{Bruker}, and $T_{2,\mathrm{LER}}(C_{\mathrm{HF}})$ overlap, demonstrating the equivalence of both investigated hybrid systems.

In the evolution of the coherence time as a function of the cooperativity, three regimes can be discriminated, showing differing dependencies. These regimes are attributed to the three regimes of coupling, discussed in Sec. 3.2.4. For $C_{\mathrm{HF}} < 1$ the hybrid system is only weakly coupled, exhibiting an onset of saturation for the T_2 time, with deceasing cooperativity. In the high cooperativity regime ($C_{\mathrm{HF}} < 1$), the coherence time shows a direct proportionality to the cooperativity. The preceding two regimes are in good agreement
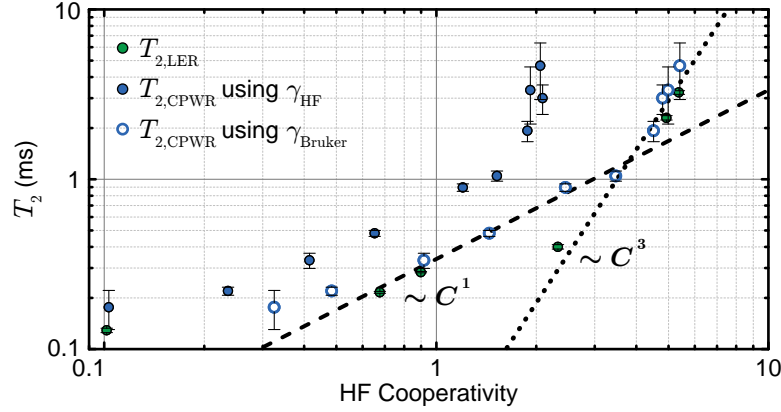
Figure 4.19: At the degeneracy point of microwave resonator and high-field spin transition extracted coherence time $T_{2,\mathrm{CPWR}}$ (blue symbols) and $T_{2,\mathrm{LER}}$ (green symbols) as a function of the high-field cooperativity C_{HF}. T_2 and the corresponding C_{HF} are determined at similar temperatures. The coherence time $T_{2,\mathrm{CPWR}}$ of the CPWR / spin ensemble hybrid system is plotted twice, for differently calculated C_{HF}, using γ_{HF}, determined as described in Sec. 3.3.1 (filled blue circles), and using γ_{Bruker}, determined in Sec. 3.3.3 (blue circles).

with the in Eq. (4.8) found dependence for the instantaneous diffusion time constant T_{ID} on the collective coupling g_{eff}. This corroborates, that a suppression of the instantaneous diffusion process can account for the enhancement of the hybrid system's coherence time, in the weak coupling and the high cooperativity regime. However, for $C_{\mathrm{HF}} > 4$ the proportionality changes to $T_2 \propto C_{\mathrm{HF}}^3$, which is not expected from only considering the suppression of instantaneous diffusion. It is assumed, that the change in proportionality is connected to the onset of strong coupling between the microwave resonator and the phosphorus donor spin ensemble. The preceding discussions, suggest static magnetic field fluctuations as the dominating mechanism of decoherence, below 200 mK. However, a suppression of the influence from field fluctuations is only expected for the resonator-like hybrid system, and not for the hybrid system tuned to its degeneracy point (cf. Fig. 4.18 (b)). Unfortunately, the present experimental data on the hybrid system's coherence time shows no clear indication on the underlying mechanisms of decoherence, at low temperatures. Still, further investigations are required, to extend the available data for the strong coupling regime.

4.3.3   Inversion Recovery Spectroscopy

When exciting the magnetization of the spin ensemble by a microwave pulse, the magnetization's projection on the quantization axis can be extracted by applying a spin-echo pulse sequence. The echo signal from the equilibrium magnetization defines a reference, as it yields the largest signal intensity. Thus, by subsequently increasing the waiting time T, between an initial preparation pulse and the spin-echo pulse sequence, the relaxation of the magnetization can be observed [72]. In conventional pulse ESR, the preparation pulse fully inverts the magnetization and its complete recovery into the equilibrium is detected. The obtained echo signal of the so-called inversion recovery pulse sequence exponentially increases to the equilibrium intensity with increasing T [72]

$$\frac{I(\mathrm{T})}{I_{\mathrm{input}}} \propto 1 - 2e^{-\frac{\mathrm{T}}{T_1}}. \tag{4.10}$$
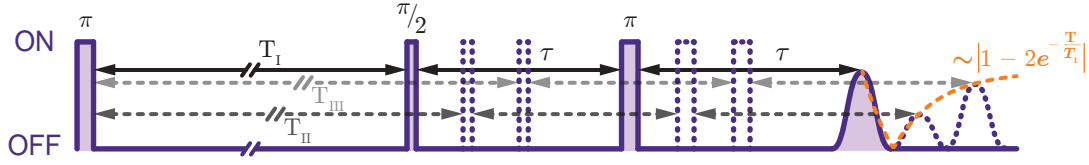
Figure 4.20: Schematic inversion recovery pulse sequence, when using the magnitude detection method [125]. Repeatedly applying the sequence, while increasing the wait time T, results in an echo signal evolution as given in Eq. (4.11). The characteristic time constant of the echo signal evolution corresponds to the longitudinal relaxation time T_1.

The characteristic time constant corresponds to the longitudinal relaxation time T_1. For magnitude detection [125], the echo signal evolution changes to

$$\frac{I(\mathrm{T})}{I_{\mathrm{input}}} \propto \left| 1 - 2e^{-\frac{\mathrm{T}}{T_1}} \right|. \tag{4.11}$$

Figure 4.20 schematically shows the inversion recovery pulse sequence, for the case of magnitude detection.

In the following, the microwave resonator / spin ensemble hybrid system is studied by inversion recovery spectroscopy. The T_1 time is determined for temperatures, ranging from 50 mK to 4 K. The acquired relaxation times are compared to results obtained by conventional pulse ESR, either from Ref. [4], or from reference measurements on similar prepared phosphorus doped ^{28}Si crystals (cf. Sec. 2.2.2), using the commercial Bruker electron spin resonance spectrometer, as described in Sec. 4.3.2. Finally, the influence of the coupling, between microwave resonator and spin ensemble, on the energy relaxation is discussed.

Millikelvin Inversion Recovery Spectroscopy

The microwave resonator / spin ensemble hybrid system is studied in the cryogen free dilution refrigerator setup (cf. Sec. 2.3.1). The T_1 time is extracted as a function of temperature and for both hybrid systems, comprising the CPWR and the LER. Thereby, the high-field spin transition of the phosphorus donor spin ensemble is either coupled to the first harmonic of the CPWR, or to resonator B of the LER (cf. Sec. 3.3.1 and Sec. 3.4.1, respectively). The applied pulses for the inversion recovery sequence are determined as outlined in Sec. 4.3.1. As with the Hahn echo spectroscopy in Sec. 4.3.2, the inversion recovery pulse sequence is applied at the degeneracy point of resonator and spin ensemble, where $\omega_{\mathrm{r}} = \omega_{\mathrm{s,HF}}$.

Figure 4.21 (a) and (b) show the integrated echo signal of the inversion recovery spectroscopies as a function of the wait time T at 50 mK, using the CPWR and LER, respectively. For both inversion recovery spectroscopies no complete inversion of the observed spins is achieved. Using the CPWR about 50 % of the spins are inverted, while with the LER about 60 % of the observed spins are inverted. The incomplete inversion of the observed spins is attributed to the limited microwave power, which can be applied to the resonator in this setup (cf. Sec. 2.3.1). Furthermore, the difference in inverted spins is assumed to be a result of the differing collective coupling strength g_{eff} of both hybrid systems. As g_{eff} for the LER is about 10 % larger than for the CPWR, the energy transfer between LER and spin ensemble is more effective, resulting in a more effective inversion of the observed spins.
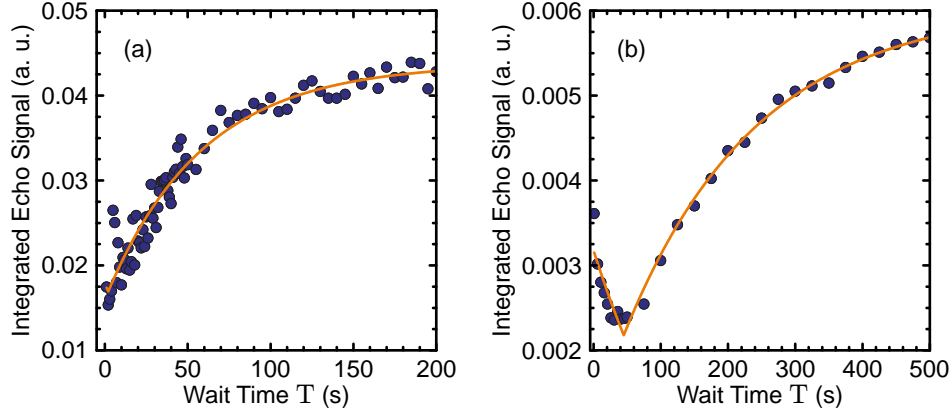
Figure 4.21: Integrated echo signal as a function of the wait time T obtained from a inversion recovery spectroscopy on the hybrid system at 50 mK, using the CPWR and LER (symbols in (a) and (b), respectively). The solid lines represent a fit to the echo signal, with the proportionality given in Eq. (4.11).

The extracted relaxation times for the CPWR and LER are $T_{1,\mathrm{CPWR}} = 58.71\,\mathrm{s} \pm 5.1\,\mathrm{s}$ and $T_{1,\mathrm{LER}} = 196.81\,\mathrm{s} \pm 17.4\,\mathrm{s}$, respectively. From Ref. [115–117] a T_1 time for the CPWR (LER) of 46 s (54 s) is expected, extrapolated for 50 mK, a static magnetic field of 178.5 mT (172.5 mT) and a phosphorus donor concentration of $[\mathrm{P}] = 1 \times 10^{17}\,\mathrm{cm}^{-3}$, assuming an energy relaxation via a direct phonon process in the low temperature limit. The determined $T_{1,\mathrm{CPWR}}$ is comparable to the expected relaxation time. In contrast, $T_{1,\mathrm{LER}}$ is about a factor of four longer than expected. For both experiments the same phosphorus doped ^{28}Si crystal is utilized, suggesting that the observed difference is connected to the coupling to the microwave resonator.

To reveal a possible dependence of T_1 on g_{eff}, a temperature series is conducted, determining the relaxation time in a temperature range between 50 mK and 4 K, for both hybrid systems. At each set temperature, the inversion recovery spectroscopy is performed at the degeneracy point of the hybrid system, prior identified by CW spectroscopy. The found relaxation times $T_{1,\mathrm{CPWR}}$ and $T_{1,\mathrm{LER}}$ are summarized in Fig. 4.22. For reference, T_1 for similar prepared ^{28}Si crystals is determined for temperatures ranging from 6 K to 13 K, in a conventional pulse ESR setup, introduced in Sec. 4.3.2.

First, the from an uncoupled phosphorus donor spin ensemble expected dependence of T_1 on temperature shall be discussed. Over the experimentally investigated temperature range, the longitudinal relaxation time is expected to exhibit several changes in its dependence on temperature (solid and dotted lines in Fig. 4.22). For temperatures above 6 K, T_1 decreases exponentially with increasing temperature. Here, the dominating relaxation process is given by resonance fluorescence by phonons, which are resonant with one of the phosphorus donor electron doublet or triplet energy states [116]. In its excited state, the donor electron spin can relax before reemitting the absorbed phonon, being more effective than a spin relaxation in the donor electron ground state. Below 6 K, T_1 is known to exhibits a transition to a power-law dependence, corresponding to two phonon Raman spin scattering processes [115, 116]. In this region, a T^{-9} and a T^{-7} dependence contribute to the evolution of T_1, corresponding to spin flip mechanisms due to spin-orbit interactions or anisotropic Zeeman interactions of the donor electron doublet state, respectively [116]. For the experimentally found relaxation times, the Raman processes are
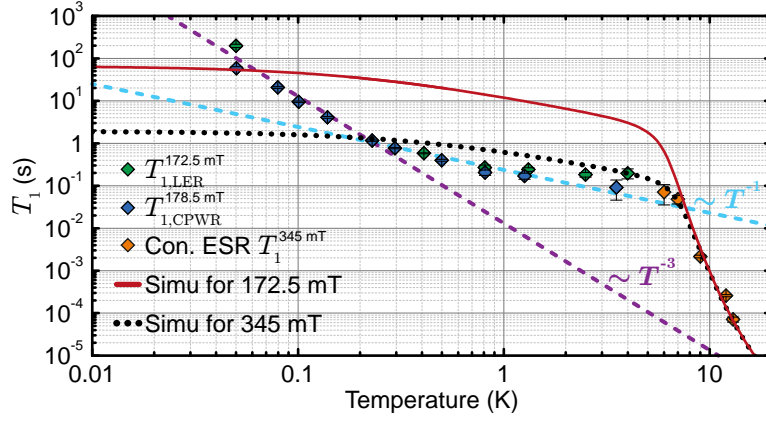
Figure 4.22: Longitudinal relaxation time T_1 of the ^{28}Si crystal containing a phosphorus donor concentration of $[P] = 1 \times 10^{17}$ cm^{-3} as a function of temperature. The plot summarizes the T_1 times determined by conventional pulse ESR (orange symbols) and extracted from the hybrid system, comprising either LER B (green symbols) or the CPWR (blue symbols). The solid and the dotted lines represent a model function, showing the from an uncouple phosphorus donor spin ensemble expected temperature dependence of T_1, for a static magnetic field of 172.5 mT and 345 mT, respectively. The dashed lines are intended as guides for the eye, illustrating the temperature dependence of the experimental data.

surpassed by the at low temperature dominating direct phonon process. For the given phosphorus donor concentration, the direct phonon process is strongly enhanced, masking the contributions from the Raman processes [115, 116, 132]. For a dominating direct phonon process $T_1 \propto T^{-1}$ [115, 116, 133]. This process dominates as long as the energy of the phonons is sufficient to excite an electron spin. When the thermal energy is reduced below the Zeeman energy splitting ($k_B T < g_{eP} \mu_B B_0$), thermal phonons no longer can contribute to the relaxation process. In this low temperature limit, the longitudinal relaxation time becomes temperature independent [117, 134, 135].

The during the course of this thesis acquired T_1 data, on the ^{28}Si crystal containing a phosphorus donor concentration of $[P] = 1 \times 10^{17}$ cm^{-3}, exhibits the transition from the exponential to the linear temperature dependence below 6 K. As expected, the data around 6 K shows no clear evidence for a power-law temperature dependence, corresponding to two phonon Raman relaxation processes. Down to a temperature of about 230 mK, the T_1 time of both hybrid systems is of similar magnitude and exhibits a linear dependence on temperature, suggesting a direct phonon process as the leading mechanism of relaxation. Below 230 mK, the dependence on temperature becomes stronger, with $T_1 \propto T^{-3}$, which strongly differs from the expected temperature independent behavior.

However, the results from both setups cannot be directly compared, as they are acquired at different static magnetic fields. Besides a temperature dependence, the direct phonon and the T^{-7} Raman process also show a strong dependence on the applied static magnetic field B_0, with respective dependencies of $\propto B_0^{-4} T^{-1}$ and $\propto B_0^{-2} T^{-7}$ [116, 133]. In the low temperature limit, the dependence of the direct phonon process changes to $T_1 \propto B_0^{-5}$ [117, 134, 135]. To allow a comparison of the obtained data, two model functions are included in Fig. 4.22, representing the expected temperature dependence for the two individual static magnetic fields applied during the experiments. For the experimental data concerning the hybrid system, only one model function is shown, since the applied B_0 for both temperature series is of comparable magnitude. The model function for the

relaxation rate $1/T_1$ is given by

$$\frac{1}{T_1} = K_1 e^{-\frac{\Delta}{k_B}T} + K_2 B_0^2 T^7 + K_3 B_0^4 T + \frac{g_{eP}\mu_B}{k_b} K_3 B_0^5. \qquad (4.12)$$

The first term on the right hand side of the model function corresponds to resonance fluorescence, the second to a Raman process, the third to a direct phonon process and the last to the low temperature limit of the direct phonon process. The model is based on the results of Ref. [115–117] and is adapted for the investigated ^{28}Si crystal. K_1, K_2, K_3 and Δ are considered as free parameters and are determined to $1.1 \times 10^8\,\mathrm{s^{-1}}$, $9.1 \times 10^{-5}\,\mathrm{s^{-1}T^{-2}K^{-7}}$, $105.2\,\mathrm{s^{-1}T^{-4}K^{-1}}$ and $123\,\mathrm{K}$, respectively

Within the investigated temperature region, the T_1 of the hybrid system is shorter than the expected T_1 for an uncoupled spin ensemble, for $B_0 = 172.5\,\mathrm{mT}$, except for the lowest investigated temperature. Between $230\,\mathrm{mK}$ and $4\,\mathrm{K}$ the hybrid system's relaxation time is about a factor of 50 shorter than expected, while below $230\,\mathrm{mK}$ the differnece becomes smaller with decreasing temperature, showing a temperature dependence proportional to T^{-3}. At $T = 50\,\mathrm{mK}$, $T_{1,\mathrm{CPWR}}$ is comparable to the expected value, while $T_{1,\mathrm{LER}}$ is about a factor of four longer than expected.

The discrepancy between $230\,\mathrm{mK}$ and $4\,\mathrm{K}$ can be attributed to a finite error in the absolute phosphorus donor concentration. For the investigated donor concentrations, T_1 exhibits a strong dependence on the actual concentration [115, 132]. Figure 4.23 plots the relaxation rate $1/T_1$ as a function of the phosphorus donor concentration in $^{\mathrm{nat}}$Si, taken from Ref. [115]. The different samples are investigated at a temperature of $1.25\,\mathrm{K}$ and a static magnetic field of $320\,\mathrm{mT}$. Two distinct regions can be identified for the relaxation rate. A concentration independent region below $10^{16}\,\mathrm{cm^{-3}}$ and a region which strongly depends on the phosphorus donor concentration above $10^{16}\,\mathrm{cm^{-3}}$, following a $[\mathrm{P}]^9$ dependence. An uncertainty of about $20\,\%$ in concentration would translate in an uncertainty of more than an order of magnitude in the relaxation rate (highlighted area in Fig. 4.23. The data extracted from the hybrid system would be well inside this error margin. The T_1 time determined at $6\,\mathrm{K}$ by conventional pulse ESR, also shows a large uncertainty, tolerating a $20\,\%$ uncertainty in concentration, too. Furthermore, the exact phosphorus donor concentration was not verified during the course of this thesis, justifying the assumption of a finite error in the absolute phosphorus donor concentration. Thus, when considering an about $20\,\%$ higher phosphorus donor concentration, the expectations from the model function would coincide with the experimental data, for temperatures ranging from $230\,\mathrm{mK}$ to $4\,\mathrm{K}$.

The increase of the T_1 time below a temperature of $230\,\mathrm{mK}$, however, is not corroborated by the model function. The observed difference to the expected behavior is suggested to be connected with the collective coupling between microwave resonator and spin ensemble. The underlying process is assumed to relate to the enhancement of the phase memory time, discussed in Sec. 4.2.2. Here, the prolonged FID is attributed to the relaxation of antisymmetric energy states, to which the hybrid system's superradiant energy states can couple under the influence of e.g. an inhomogeneous broadening or dipole-dipole interactions among the spins [31, 121]. These antisymmetric energy states of the spin ensemble no longer contain the ground state, like e.g. the singlet energy state for two spin 1/2. An additional change of angular momentum would be required to access the ground state, which the resonator can not provide. In this context, a trapping of the
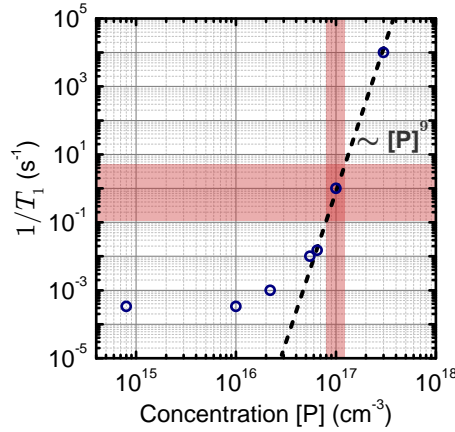
Figure 4.23: Relaxation rate $1/T_1$ as a function of the phosphorus donor concentration, at a temperature of $1.25\,\mathrm{K}$ and a static magnetic field of $320\,\mathrm{mT}$. The data is obtained from Ref. [115].

polarization can occur, prohibiting a relaxation to the equilibrium [31]. A characteristic of such a process would be a bi-exponential recovery of the magnetization, observed in an inversion recovery spectroscopy. The acquired integrated echo signals as a function of the wait time T, at $50\,\mathrm{mK}$ show only an onset of complete saturation, for both hybrid systems (cf. Fig. 4.21). Extending the wait time could reveal the presence of a second time constant. As a consequence, the determined relaxation times would be a superposition of a short and a long time constant, not representing the actual time required by the system to reach full equilibrium.

Finally, the obtained data on the relaxation time of the microwave resonator / phosphorus donor spin ensemble hybrid system demonstrates the applicability of known concepts from conventional pulse ESR. The expected behavior differs from the experimental observation, when the interaction between the two subsystems becomes strong. The conducted experiments are a proof of principal, that the regime of strong coupling is indeed a field of most interest, since it can have a significant influence on the known behavior of the individual subsystems.

Chapter 5

Summary & Conclusion

The thesis concentrats on the spectroscopic investigation of a hybrid system, constituated of a superconducting coplanar microwave resonator and an ensemble of phosphorus donor spins in an isotopically purified ^{28}Si host crystal. The hybrid system is studied, utilizing two different designs of microwave resonators, a coplanar waveguide resonator (CPWR) and a lumped element resonator (LER), both based on superconducting niobium. Employing continuous wave (CW) and pulsed spectroscopy techniques, the hybrid system is characterized in the frequency and the time domain, respectively. The results demonstrate the great potential of hybrid systems, in the field of quantum information processing.

During the course of this thesis, pulsed microwave spectroscopy experiments have been performed, at millikelvin temperatures. Applying the well known concepts of pulsed electron spin resonance, the dynamical response as well as the intrinsic relaxation and coherence time of the hybrid system are investigated. By single pulse spectroscopy, the hybrid system's steady state response to a high power and long microwave pulse is analyzed. The resonator normal mode splitting could be resolved by this method, equivalent to the results obtained from CW spectroscopy. The parameters of the hybrid system are extracted, using the evaluation procedure utilized in the analysis of the CW data. Investigating the normal mode splitting at the beginning of the microwave pulse, both measurement methods yield comparable parameters. Additionally, pulsed ESR spectroscopy using a single pulse excitation scheme performed at small detunings from the degeneracy point, revealed a third hybrid mode. The magnetic field dispersion of the three modes is investigated and modeled by a modified Tavis-Cummings model, including an additional excitation. The model allowed a qualitative description of the three hybrid mode's resonance frequency dispersion. The free induction decay after a single high power microwave pulse, exhibited a bi-exponential decay. The additional decay process is attributed to subradiant energy states, which suppress the decoherence mechanisms. A remarkable enhancement of the decay time is found, in respect to the from an uncoupled spin ensemble expected decay time. The longest decay time is found at the resonance frequency of the additional hybrid mode, which is determined to $39.4\,\mu s$, corresponding to an enhancement of more than two orders of magnitude.

The coherence time of the hybrid system is determined systematically by Hahn echo spectroscopy, in a temperature range between $50\,mK$ and $4\,K$. By comparing the results with the coherence time obtained from conventional pulsed electron spin resonance for

temperatures from 6 K to 15 K, an exceptional and unexpected enhancement of more than two orders of magnitude is found for the hybrid system at the lowest temperature. Over the investigated temperature range, the coherence time of the hybrid system is found to increase linearly with decreasing temperature, whereas the coherence time would have been expected to be temperature independent. These findings are modeled by a suppression of instantaneous diffusion, due to a decreased spectral overlap between the microwave pulse spectrum and the hybrid system's spectrum, which is equivalent to a smaller rotation angle of the spin system's magnetization. The model allows to describe the temperature dependence of the coherence time down to a temperature of 200 mK. Below 200 mK, it differs from the experimentally observed dependence, suggesting that at this temperatures instantaneous diffusion is no longer dominating the decoherence mechanism. These experiments are performed at the degeneracy point of the hybrid system, where pulse frequency and spin transition frequency of the spin ensemble are in resonance. At 50 mK, the hybrid system's coherence time is also determined at the resonance frequencies of the two hybrid modes as a function of the detuning from the degeneracy point. For large detunings, the hybrid system's dispersion approaches the individual dispersions of the resonator and spin ensemble, becoming more resonator-like or spin-like. For when the hybrid system becomes more resonator-like, the coherence time is found to be even more enhanced, compared to the coherence time extracted at the degeneracy point. Contrary, the coherence time is reduced for the more spin-like hybrid system. This is attributed to a suppressed influence from magnetic field fluctuations, as the magnetic field dispersion of the resonator-like branch of the hybrid system flattens out. Finally, the dependence of the coherence time on the cooperativity of the hybrid system is discussed, where three different regimes are identified and classified by the three coupling regimes: (i) In the regime of weak coupling the coherence time shows only a weak dependence on the cooperativity, indicating an onset of saturation. (ii) In the regime of high cooperativity a linear dependence between coherence time and cooperativity is found and (iii) in the strong coupling regime this increases to a cubic dependence.

The relaxation time of the hybrid system is studied using a inversion recovery pulse sequence, in a temperature range between 50 mK and 4 K. Down to a temperature of 230 mK the relaxation time can be described with the expectations from an uncoupled spin ensemble. The modeling of the relaxation time includes an exponential decrease above 7 K, due to resonance fluorescence by phonons, a T^{-7} Raman process between 6 K and 7 K and a T^{-1} direct phonon process for low temperatures. For temperatures below 230 mK, the relaxation time exhibited a T^{-3} dependence on temperature, significantly differing from the temperature independent behavior, reported in the literature. In this temperature regime, the hybrid system is assumed to couple to long living subradiant energy states, in which the polarization is effectively trapped.

By CW spectroscopy, the CPWR / phosphorus donor spin ensemble hybrid system is shown to operate in a regime of high cooperativity [3]. At a temperature of 50 mK, a collective coupling $g_{\text{eff}}/2\pi = 1.13$ MHz and 1.07 MHz between the spin ensemble and the microwave resonator is determined for each of the two hyperfine split phosphorus donor spin transitions. The resulting collective coupling is corroborated quantitatively by numerical calculations. For the given microwave resonator design, a theoretical maximum value of $g_{\text{eff,theo}}/(2\pi) = 3.17$ MHz is expected and the discrepancy is attributed to a finite gap present between the superconducting resonator surface and the phospho-

rus doped ^{28}Si crystal. The found loss rates of the phosphorus donor spin ensemble $\gamma/2\pi = 1.38$ and 1.40 MHz exceeded both the collective coupling rate, preventing the hybrid system to reach the strong coupling regime. Measurements on similarly prepared ^{28}Si crystals in a commercial electron spin resonance spectrometer showed a loss rate of $\gamma_{\text{Bruker}}/2\pi = 530$ kHz, which is also in agreement with the results from the experiments comprising the LER. This allows to attribute the increase in loss rate to a inhomogeneity of the static magnetic field generated by the superconducting magnet. Additionally, the experimentally found temperature dependence is modeled by a statistical function, which considers the thermal polarization of the spin ensemble. The derived statistical function shows to be in excellent agreement with the determined collective couplings, showing a scaling of g_{eff} with the square root of the number of thermally polarized spins.

The change of the microwave resonator design from the CPWR to the LER, allowed to circumvent the inhomogeneities of the static magnetic field, due to its more compact design. This pushed the LER / phosphorus donor spin ensemble hybrid system into the regime of strong coupling, which is demonstrated for the first time for phosphorus donors in silicon. In these experiments, the CW microwave transmission of the resonator exhibited a clear normal mode splitting, with two well separated hybrid modes. However, the two hybrid modes showed a distingtly different linewidth for the two split modes at the degeneracy point, which is not expected from the Tavis-Cummings model. Therefore, the parameters for the resonator and spin ensemble loss rate are determined at their individual dispersions, far detuned from the degeneracy point, while the collective coupling is determined by the normal mode splitting. The collective coupling is identified to 1.37 MHz and 1.23 MHz for both hyperfine split phosphorus donor spin transitions, exceeding the resonator loss rate of 410 kHz as well as the respective spin ensemble loss rates of 529.29 kHz and 456.77 kHz. To explain the asymmetric linewidth of the normal mode splitting, the Tavis-Cummings model is extended to include a complex microwave drive and an incoherent coupling process. This incoherent process is assumed to couple the resonator and the spin ensemble indirectly via a bath of vacuum field modes, which could be provided by the broadband coplanar waveguide feedline, present for the LER design. The introduced model can qualitatively describe the evolution of the hybrid mode's linewidth dispersion. Furthermore, the characteristic shape of the resonator's microwave transmission spectrum can be described by this model with very good agreement. The extracted collective coupling for both phosphorus donor spin transitions are 1.32 MHz and 1.15 MHz, while the incoherent coupling is identified to 265 kHz. The results still exceed the resonator loss rate of 410 kHz as well as the via the extended model determined respective spin ensemble loss rates of 596 kHz and 602 kHz.

In summary, the presented results demonstrate the vast potential of hybrid systems in the field of quantum information processing. These systems grant the advantages of both constituents, while simultaneously their individual limitations are overcome. Still, the individual subsystems can be tuned independently from each other, when it is required. This tunability allows a continuous transition between the coupled and uncoupled state, with the hybrid system to be able to provide a regime with long coherence times, as well as a regime with strong interactions. Furthermore, the studies on the characteristic time constants of the hybrid system revealed the impact of the collective coupling. By controlling the collective coupling, the storage properties can be tuned on an extraordinary large scale. The investigated system allows to change its coherence time by two orders of magnitude, exceeding the coherence time of the individual subsystems. Furthermore, the

longest achieved coherence time is in the same order of magnitude as expected from spin ensembles containing a two orders of magnitude lower phosphorus donor concentration [4]. This allows to realize long, as well as tunable, storage times, while maintaining an excellent signal quality due to the high doping concentration. Combining these properties with the generation of additional long living states in the hybrid system, under the influence of high power microwave pulses, opens up new possibilities for storage applications. By achieving a direct preparation of these states, a multi mode storage could be implemented in a single hybrid system, within a decoherence free subspace [120]. For a spin 1/2 system, the dimension of such a subspace would be $N/2$, where N gives the number of spins. Thus, a spin ensemble based hybrid system would allow to store a vast amount of information. Already, schemes are being investigated, which allow the preparation of long living states in a hybrid system [38]. This thesis, represents an initial step towards a full control of the hybrids system's coherence time. Further, an initial scheme is investigated to allow for a preparation of long living states within the hybrid system.

Optimizing the applied microwave pulses, to compensate for the oscillating magnetic field inhomogeneities, inherent to the coplanar design [78], would allow a more definite preparation of the hybrid system. This could be realized by adiabatic pulses [136] or optimal control pulses [137, 138]. Pulse optimization could be the key for a definite state preparation, allowing for the engineering of long living states.

By changing the collective coupling between the microwave resonator and the phosphorus donor spin ensemble, the coherence time as well as the relaxation time could be controlled. However, this process always involved a change in temperature. More desirable would be an in-situ control of the collective coupling, without changing the experimental parameters of the resonator and the spin ensemble. A possible approach for such an endeavor, is to utilize piezo nano positioners for an in-situ control of the relative sample position on the coplanar microwave resonator. By changing the distance between resonator surface and the spin ensemble's host crystal, the collective coupling will become tunable. This allows for an investigation on the dependence of the hybrid system's coherence time and relaxation time on the collective coupling at a constant temperature. Furthermore, considering the incoherent coupling process assumed for the LER experiments, an in-situ sample positioning can also be used to test this assumption. For these experiments, the phosphorus doped ^{28}Si crystal also covers the broadband feedline for the LERs (cf. Fig. 2.11 (b)), which is assumed to act as a bath of incoherent vacuum field modes. By changing the overlap of the ^{28}Si crystal on the feedline a change in the incoherent coupling would also be expected, verifying whether incoherent coupling is responsible for the asymmetric linewidth of the normal mode splitting.

Recent experiments on the electrical control of single phosphorus donor spin qubits [139] demonstrated an alternative way of tuning a phosphorus donor electron spin. By applying an electrical field to the donor, the electron wave function can effectively be shifted away from the donor. Hereby, the hyperfine interaction between the donor and the electron is changed, which is known as the Stark effect. A change in the hyperfine interaction would directly translate in a change of the electron's Larmor frequency. Implementing such an electrical control for the hybrid system, would allow for fast modulations of the spin ensemble's resonance frequency. This would be a clear advantage over the rather slow static magnetic field tuning, which requires about 25 s for a small field change. Furthermore, the well known concept of magnetic field modulations could also be implemented on this way,

boosting the sensitivity of the millikelvin setup.

Considering the outlined improvements an enhanced control on the hybrid system can be achieved. This would allow a more detailed study of the hybrid system's inherent potential, which could pose a major step towards the realization of a quantum computer, and also maybe to "the Answer to the Great Question of Life, the Universe and Everything" [1].

Appendix A

Appendix

A.1 Tranmission Function $|S_{21}|^2$ Including Phosphorus Donors

Using Eq. (3.46), the microwave transmission of the superconducting coplanar waveguide resonator / phosphorus donors spin ensemble hybrid system is modeled. The function is modified to include a dependence on the static magnetic field B_0, which is used to tune the spin ensemble's resonance frequency ω_s. The modified function is based on the transmission function derived in Sec. 3.2.4, which is given by

$$|S_{21}|^2 = \left(\frac{\eta}{\kappa_0}\right)^2 \left|\frac{\kappa_0}{i\Delta_r + \kappa_0 + \frac{g_{eff}^2}{i\Delta_s + \gamma}}\right|^2, \tag{A.1}$$

where the resonance frequencies of the microwave resonator and the spin ensemble are included in the respective detuning via $\Delta_r = \omega_r - \omega$ and $\Delta_s = \omega_s - \omega$. The spin ensemble's resonance frequencies are determined by the solutions of the spin Hamiltonian, given in Sec. 2.2.1. The resonance frequency for the LF and HF spin transitions are

$$\omega_{s,\,LF/HF} = \pm\frac{A}{2\hbar} + \frac{B_0}{2\hbar}\left(g_{eP}\mu_B + g_{NP}\mu_N\right) + \frac{1}{2\hbar}\sqrt{A^2 + B_0^2\left(g_{eP}\mu_B - g_{NP}\mu_N\right)^2}. \tag{A.2}$$

Including this expression in a fit function would decrease its effectiveness, due to the large amount of parameters. Therefore two simplifications are made. Since the nuclear magnetic moment is three orders of magnitude smaller than the electron magnetic moment, its contribution to the electron spin resonance frequency can be neglected at the in the experiments applied static magnetic fields. Additionally, the characteristic hyperfine splitting of 4.2 mT is also much smaller than the used static magnetic fields, allowing to neglect it in the square root term. Thus, the spin ensemble's resonance frequencies simplifies to

$$\omega_{s,\,LF/HF} = \pm\frac{A}{2\hbar} + \frac{g_{eP}\mu_B}{\hbar}B_0 = \frac{g_{eP}\mu_B}{\hbar}B_{0,\,LF/HF}, \tag{A.3}$$

including the hyperfine splitting in the expression for the resonance fields $B_{0,\,LF/HF}$. For the drive frequency ω only the electron Zeeman is assumed

$$\omega = \frac{g_{eP}\mu_B}{\hbar}B_0. \tag{A.4}$$

Inserting the expressions for ω_{s} and ω in Eq. (A.1) yields the fit function used in Sec. 3.3.1

$$|S_{21}|^2 = \left(\frac{\eta}{\kappa_0}\right)^2 \left|\frac{\kappa_0}{i(\omega_{\mathrm{r}} - \omega) + \kappa_0 + \sum\limits_{n=1}^{2} \dfrac{g_{\mathrm{eff}}^2}{i\frac{g_{\mathrm{eP}}\mu_{\mathrm{B}}}{\hbar}\left(B_{0,n} - B_0\right) + \gamma}}\right|^2, \qquad \text{with } n = \mathrm{LF}, \mathrm{HF}.$$

$$(\mathrm{A.5})$$

A.2   Transmission Spectra for LER A and C

Figures A.1 and A.2 show the microwave transmission spectra obtained for the hybrid system, comprising LER A and LER C, respectively.
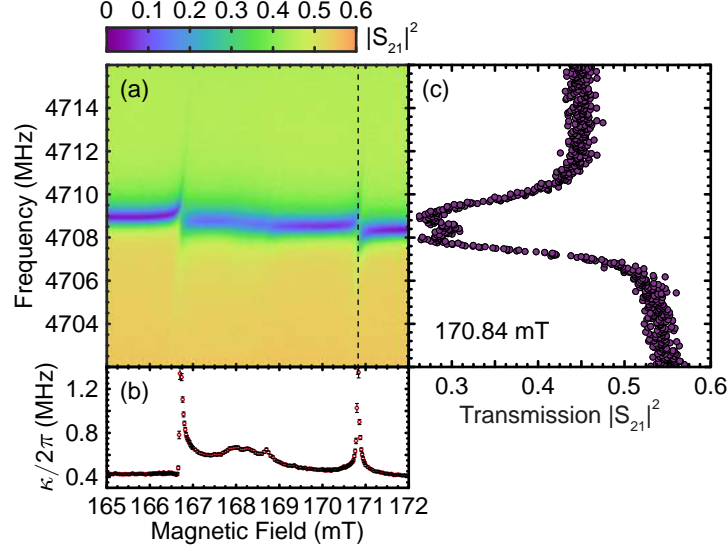
Figure A.1: Spectroscopy data of the superconducting lumped element resonator A coupled to the phosphorus spin ensemble taken at a temperature of 50 mK and an input microwave power of 40 aW. (a) Color coded microwave transmission data $|S_{21}|^2$ as a function of the VNA frequency and the magnetic field B_0. The central line of low transmission indicates the resonance frequency of the LER. At $B_{0,\mathrm{LF}} = 166.72\,\mathrm{mT}$ and $B_{0,\mathrm{HF}} = 170.84\,\mathrm{mT}$ the resonator and the spin ensemble are in resonance reducing the absorption depth. These resonances are separated by 4.14 mT, characteristic for the hyperfine splitting of phosphorus donors in silicon. (b) Effective linewidth (circles with error bars) of the resonator κ determined by the lorentzian fit (3.56) to the data in (a). (c) Resonator transmission $|S_{21}|^2$ (circles) at $B_0 = 170.84\,\mathrm{mT}$ (black dashed line in (a)), the resonance field of the high field spin transition. The resonator mode exhibits an onset of a normal mode splitting, without a clear separation in two individual transmission dips.
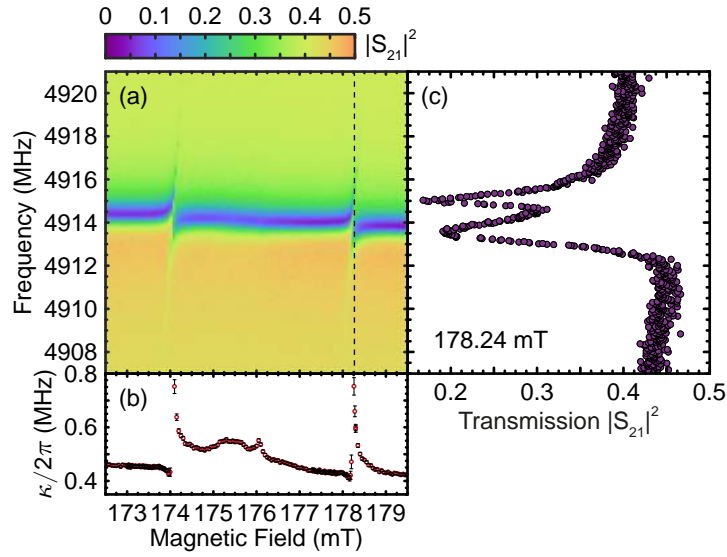
Figure A.2: Spectroscopy data of the superconducting lumped element resonator C coupled to the phosphorus spin ensemble taken at a temperature of 50 mK and an input microwave power of 40 aW. (a) Color coded microwave transmission data $|S_{21}|^2$ as a function of the VNA frequency and the magnetic field B_0. The central line of low transmission indicates the resonance frequency of the LER. At $B_{0,\mathrm{LF}} = 174.05$ mT and $B_{0,\mathrm{HF}} = 178.24$ mT the resonator and the spin ensemble are in resonance resulting in an avoided crossing. These resonances are separated by 4.19 mT, the characteristic for the hyperfine splitting of phosphorus donors in silicon. (b) Effective linewidth (circles with error bars) of the resonator κ determined by the lorentzian fit (3.56) to the data in (a). (c) Resonator transmission $|S_{21}|^2$ (circles) at $B_0 = 178.24$ mT (black dashed line in (a)), the resonance field of the high field spin transition. The resonator mode exhibits the characteristic normal mode splitting resulting in two individual transmission dips separated by $2g_{\mathrm{eff}}$.

Bibliography

[1] Adams, D. *The Hitchhiker's Guide to the Galaxy* (Del Rey, 1979).

[2] Schoelkopf, R. J. & Girvin, S. M. Wiring up quantum systems. *Nature* **451**, 664–669 (2008).

[3] Zollitsch, C. W. *et al.* High cooperativity coupling between a phosphorus donor spin ensemble and a superconducting microwave resonator. *Applied Physics Letters* **107**, – (2015).

[4] Tyryshkin, A. M. *et al.* Electron spin coherence exceeding seconds in high-purity silicon. *Nature Materials* **11**, 143–147 (2012).

[5] Saeedi, K. *et al.* Room-Temperature Quantum Bit Storage Exceeding 39 Minutes Using Ionized Donors in Silicon-28. *Science* **342**, 830 (2013).

[6] Hofheinz, M. *et al.* Synthesizing arbitrary quantum states in a superconducting resonator. *Nature* **459**, 546–549 (2009).

[7] Xiang, Z.-L., Ashhab, S., You, J. Q. & Nori, F. Hybrid quantum circuits: Superconducting circuits interacting with other quantum systems. *Reviews of Modern Physics* **85**, 623–653 (2013).

[8] Grezes, C. *et al.* Storage and retrieval of microwave fields at the single-photon level in a spin ensemble. *Physical Review A* **92**, 020301 (2015).

[9] Imamoğlu, A. Cavity QED Based on Collective Magnetic Dipole Coupling: Spin Ensembles as Hybrid Two-Level Systems. *Physical Review Letters* **102**, 083602 (2009).

[10] Wesenberg, J. H. *et al.* Quantum Computing with an Electron Spin Ensemble. *Physical Review Letters* **103**, 070502 (2009).

[11] Muhonen, J. T. *et al.* Storing quantum information for 30 seconds in a nanoelectronic device. *Nature Nanotechnology* **9**, 986–991 (2014).

[12] Niemczyk, T. *et al.* Circuit quantum electrodynamics in the ultrastrong-coupling regime. *Nature Physics* **6**, 772–776 (2010).

[13] Wallraff, A. *et al.* Strong coupling of a single photon to a superconducting qubit using circuit quantum electrodynamics. *Nature* **431**, 162–167 (2004).

[14] Kubo, Y. *et al.* Storage and retrieval of a microwave field in a spin ensemble. *Physical Review A* **85**, 012333 (2012).

[15] Grezes, C. *et al.* Multimode Storage and Retrieval of Microwave Fields in a Spin Ensemble. *Physical Review X* **4**, 021049 (2014).

[16] Wu, H. *et al.* Storage of Multiple Coherent Microwave Excitations in an Electron Spin Ensemble. *Physical Review Letters* **105**, 140503 (2010).

[17] Kubo, Y. *et al.* Strong Coupling of a Spin Ensemble to a Superconducting Resonator. *Physical Review Letters* **105**, 140502 (2010).

[18] Kubo, Y. *et al.* Hybrid Quantum Circuit with a Superconducting Qubit Coupled to a Spin Ensemble. *Physical Review Letters* **107**, 220501 (2011).

[19] Sandner, K. *et al.* Strong magnetic coupling of an inhomogeneous nitrogen-vacancy ensemble to a cavity. *Physical Review A* **85**, 053806 (2012).

[20] Putz, S. *et al.* Protecting a spin ensemble against decoherence in the strong-coupling regime of cavity QED. *Nature Physics* **10**, 720–724 (2014).

[21] Ranjan, V. *et al.* Probing Dynamics of an Electron-Spin Ensemble via a Superconducting Resonator. *Physical Review Letters* **110**, 067004 (2013).

[22] Schuster, D. I. *et al.* High-Cooperativity Coupling of Electron-Spin Ensembles to Superconducting Cavities. *Physical Review Letters* **105**, 140501 (2010).

[23] Chiorescu, I., Groll, N., Bertaina, S., Mori, T. & Miyashita, S. Magnetic strong coupling in a spin-photon system and transition to classical regime. *Physical Review B* **82**, 024413 (2010).

[24] Bushev, P. *et al.* Ultralow-power spectroscopy of a rare-earth spin ensemble using a superconducting resonator. *Physical Review B* **84**, 060501 (2011).

[25] Huebl, H. *et al.* High Cooperativity in Coupled Microwave Resonator Ferrimagnetic Insulator Hybrids. *Physical Review Letters* **111**, 127003 (2013).

[26] Tabuchi, Y. *et al.* Hybridizing Ferromagnetic Magnons and Microwave Photons in the Quantum Limit. *Physical Review Letters* **113**, 083603 (2014).

[27] Zhang, X., Zou, C.-L., Jiang, L. & Tang, H. X. Strongly Coupled Magnons and Cavity Microwave Photons. *Physical Review Letters* **113**, 156401 (2014).

[28] Cao, Y., Yan, P., Huebl, H., Goennenwein, S. T. B. & Bauer, G. E. W. Exchange magnon-polaritons in microwave cavities. *Physical Review B* **91**, 094423 (2015).

[29] Bai, L. *et al.* Spin Pumping in Electrodynamically Coupled Magnon-Photon Systems. *Physical Review Letters* **114**, 227201 (2015).

[30] Sigillito, A. J. *et al.* Fast, low-power manipulation of spin ensembles in superconducting microresonators. *Applied Physics Letters* **104**, – (2014).

[31] Butler, M. C. & Weitekamp, D. P. Polarization of nuclear spins by a cold nanoscale resonator. *Physical Review A* **84**, 063407 (2011).

[32] Bradford, M. & Shen, J.-T. Spontaneous emission in cavity qed with a terminated waveguide. *Physical Review A* **87**, 063830 (2013).

[33] Wood, C. J. & Cory, D. G. Cavity cooling to the ground state of an ensemble quantum system. *Physical Review A* **93**, 023414 (2016).

[34] Bienfait, A. *et al.* Controlling spin relaxation with a cavity. *Nature* **531**, 74–77 (2016).

[35] Diniz, I. *et al.* Strongly coupling a cavity to inhomogeneous ensembles of emitters: Potential for long-lived solid-state quantum memories. *Physical Review A* **84**, 063810 (2011).

[36] Kurucz, Z., Wesenberg, J. H. & Mølmer, K. Spectroscopic properties of inhomogeneously broadened spin ensembles in a cavity. *Physical Review A* **83**, 053852 (2011).

[37] Krimer, D. O., Hartl, B. & Rotter, S. Hybrid Quantum Systems with Collectively Coupled Spin States: Suppression of Decoherence through Spectral Hole Burning. *Physical Review Letters* **115**, 033601 (2015).

[38] Putz, S. *et al.* Engineering Long-Lived Collective Dark States in Spin Ensembles. *arXiv* (2015).

[39] Zhang, X. *et al.* Magnon dark modes and gradient memory. *Nature Communications* **6**, – (2015).

[40] Blais, A., Huang, R.-S., Wallraff, A., Girvin, S. M. & Schoelkopf, R. J. Cavity quantum electrodynamics for superconducting electrical circuits: An architecture for quantum computation. *Physical Review A* **69**, 062320 (2004).

[41] Göppl, M. *et al.* Coplanar waveguide resonators for circuit quantum electrodynamics. *Journal of Applied Physics* **104**, 113904 (2008).

[42] Simons, R. N. *Coplanar Waveguide Circuits, Components, and Systems* (Wiley-Interscience, New York, 2001).

[43] Pozar, D. M. *Microwave Engineering* (John Wiley and Sons Inc., New York, 1998).

[44] Niemczyk, T. *From strong to ultrastrong coupling in circuit QED architectures.* Ph.D. thesis, Technische Universität München (2011).

[45] Mazin, B. A. *Microwave Kinetic Inductance Detectors.* Ph.D. thesis, California Institute of Technology (2004).

[46] Khalil, M., Wellstood, F. & Osborn, K. Loss Dependence on Geometry and Applied Power in Superconducting Coplanar Resonators. *IEEE Transactions on Applied Superconductivity* **21**, 879–882 (2011).

[47] Geerlings, K. *et al.* Improving the quality factor of microwave compact resonators by optimizing their geometrical parameters. *Applied Physics Letters* **100**, 192601 (2012).

[48] Lindström, T., Healey, J. E., Colclough, M. S., Muirhead, C. M. & Tzalenchuk, A. Y. Properties of superconducting planar resonators at millikelvin temperatures. *Physical Review B* **80**, 132501 (2009).

[49] Doyle, S. *Lumped Element Kinetic Inductance Detectors*. Ph.D. thesis, Cardiff University (2008).

[50] Wadell, B. C. *Transmission line design handbook* (Artech House, USA, 1991).

[51] Probst, S. *et al.* Anisotropic Rare-Earth Spin Ensemble Strongly Coupled to a Superconducting Resonator. *Physical Review Letters* **110**, 157001 (2013).

[52] Fano, U. Effects of Configuration Interaction on Intensities and Phase Shifts. *Physical Review* **124**, 1866–1878 (1961).

[53] Ladd, T. D. *et al.* All-Silicon Quantum Computer. *Physical Review Letters* **89**, 017901 (2002).

[54] Pla, J. J. *et al.* Coherent Control of a Single ^{29}Si Nuclear Spin Qubit. *Physical Review Letters* **113**, 246801 (2014).

[55] Morton, J. J. L., McCamey, D. R., Eriksson, M. A. & Lyon, S. A. Embracing the quantum limit in silicon computing. *Nature* **479**, 345–353 (2011).

[56] Kane, B. E. A silicon-based nuclear spin quantum computer. *Nature* **393**, 133–137 (1998).

[57] Becker, P., Pohl, H.-J., Riemann, H. & Abrosimov, N. Enrichment of silicon for a better kilogram. *physica status solidi (a)* **207**, 49–66 (2010).

[58] Steger, M. *et al.* Quantum Information Storage for over 180 s Using Donor Spins in a 28Si "Semiconductor Vacuum". *Science* **336**, 1280–1283 (2012).

[59] Zwanenburg, F. A. *et al.* Silicon quantum electronics. *Review of Modern Physics* **85**, 961–1019 (2013).

[60] Kohn, W. & Luttinger, J. M. Hyperfine Splitting of Donor States in Silicon. *Physical Review* **97**, 883–888 (1955).

[61] Luttinger, J. M. & Kohn, W. Motion of Electrons and Holes in Perturbed Periodic Fields. *Physical Review* **97**, 869–883 (1955).

[62] Pantelides, S. T. The electronic structure of impurities and other point defects in semiconductors. *Reviews of Modern Physics* **50**, 797–858 (1978).

[63] Koiller, B., Capaz, R. B., Hu, X. & Das Sarma, S. Shallow-donor wave functions and donor-pair exchange in silicon: *Ab initio* theory and floating-phase heitler-london approach. *Physical Review B* **70**, 115207 (2004).

[64] Overhof, H. & Gerstmann, U. *Ab Initio* Calculation of Hyperfine and Superhyperfine Interactions for Shallow Donors in Semiconductors. *Physical Review Letters* **92**, 087602 (2004).

[65] Wilson, D. K. & Feher, G. Electron Spin Resonance Experiments on Donors in Silicon. III. Investigation of Excited States by the Application of Uniaxial Stress and Their Importance in Relaxation Processes. *Physical Review* **124**, 1068–1083 (1961).

[66] Kohn, W. Shallow impurity states in semiconductors. *Il Nuovo Cimento (1955-1965)* **7**, 713–723 (2007).

[67] Huebl, H. *et al.* Phosphorus Donors in Highly Strained Silicon. *Physical Review Letters* **97**, 166402 (2006).

[68] Feher, G. Electron Spin Resonance Experiments on Donors in Silicon. I. Electronic Structure of Donors by the Electron Nuclear Double Resonance Technique. *Physical Review* **114**, 1219–1244 (1959).

[69] Stone, N. Table of nuclear magnetic dipole and electric quadrupole moments. *Atomic Data and Nuclear Data Tables* **90**, 75 – 176 (2005).

[70] Abe, E. *et al.* Electron spin coherence of phosphorus donors in silicon: Effect of environmental nuclei. *Physical Review B* **82**, 121201 (2010).

[71] Portis, A. M. Electronic Structure of *F* Centers: Saturation of the Electron Spin Resonance. *Physical Review* **91**, 1071–1078 (1953).

[72] Schweiger, A. & Jeschke, G. *Principles of Pulse Electron Paramagnetic Resonance* (Oxford University Press, 2001).

[73] Hübl, H. *Coherent Manipulation and Electrical Detection of Phosphorus Donor Spins in Silicon*. Ph.D. thesis, Technische Universität München (2007).

[74] Schneider, C. M. F. *On-chip Superconducting Microwave Beam Splitter*. Master's thesis, Technische Universität München (2014).

[75] Oxford Instruments. *Triton*^{TM} *200/400 Cryofree*® *Dilution Refrigerator, Operator's Handbook*.

[76] Greifenstein, M. A. *Elektronenspinresonanz mit supraleitenden Mikrowellenres-onatoren bei Millikelvin-Temperaturen*. Master's thesis, Technische Universität München (2012).

[77] Hiebel, M. *Grundlagen der vektoriellen Netzwerkanalyse* (Rohde & Schwarz GmbH & Co. KG, München, 2006).

[78] Simons, R. & Arora, R. Coupled Slot Line Field Components. *IEEE Transactions on Microwave Theory and Techniques* **30**, 1094–1099 (1982).

[79] Khalil, M. S., Stoutimore, M. J. A., Wellstood, F. C. & Osborn, K. D. An analysis method for asymmetric resonator transmission applied to superconducting devices. *Journal of Applied Physics* **111**, – (2012).

[80] Wallace, W. J. & Silsbee, R. H. Microstrip resonators for electron-spin resonance. *Review of Scientific Instruments* **62**, 1754–1766 (1991).

[81] Gubin, A. I., Il'in, K. S., Vitusevich, S. A., Siegel, M. & Klein, N. Dependence of magnetic penetration depth on the thickness of superconducting Nb thin films. *Physical Review B* **72**, 064503 (2005).

[82] Micro-Coax. *Microwave & RF Cable*. URL `http://micro-coax.com/wp-content/themes/micro_coax/includes/pdf/13-MIC-0006.Semi-Rigid_Brochure_FINAL_Web.pdf`.

[83] Kerchner, H. R., Christen, D. K. & Sekula, S. T. Critical fields H_c and H_{c2} of superconducting niobium. *Physical Review B* **24**, 1200–1204 (1981).

[84] Poepel, R. Exact solutions of the Mattis Bardeen theory for thin superconducting films and bulk material. *IEEE Transactions on Magnetics* **27**, 1306–1309 (1991).

[85] Gross, R. & Marx, A. *Festkörperphysik*. De Gruyter Studium (De Gruyter, 2014).

[86] Song, C., DeFeo, M. P., Yu, K. & Plourde, B. L. T. Reducing microwave loss in superconducting resonators due to trapped vortices. *Applied Physics Letters* **95**, – (2009).

[87] Bothner, D., Gaber, T., Kemmler, M., Koelle, D. & Kleiner, R. Improving the performance of superconducting microwave resonators in magnetic fields. *Applied Physics Letters* **98**, – (2011).

[88] Tinkham, M. *Introduction to Superconductivity: Second Edition*. Dover Books on Physics (Dover Publications, 2004).

[89] Jaynes, E. & Cummings, F. Comparison of quantum and semiclassical radiation theories with application to the beam maser. *Proceedings of the IEEE* **51**, 89–109 (1963).

[90] Scully, M. & Zubairy, M. *Quantum Optics* (Cambridge University Press, 1997).

[91] Amsüss, D. R. *Strong coupling of an NV^- spin ensemble to a superconducting resonator*. Ph.D. thesis, Technische Universität Wien (2012).

[92] Baust, A. *Tunable Coupling and Ultrastrong Interaction in Circuit Quantum Electrodynamics*. Ph.D. thesis, Technische Universität München (2015).

[93] Dicke, R. H. Coherence in Spontaneous Radiation Processes. *Physical Review* **93**, 99–110 (1954).

[94] Tavis, M. & Cummings, F. W. Exact Solution for an N-Molecule-Radiation-Field Hamiltonian. *Physical Review* **170**, 379–384 (1968).

[95] Tavis, M. & Cummings, F. W. Approximate Solutions for an N-Molecule-Radiation-Field Hamiltonian. *Physical Review* **188**, 692–695 (1969).

[96] Henschel, K., Majer, J., Schmiedmayer, J. & Ritsch, H. Cavity QED with an ultra-cold ensemble on a chip: Prospects for strong magnetic coupling at finite temperatures. *Physical Review A* **82**, 033810 (2010).

[97] Holstein, T. & Primakoff, H. Field Dependence of the Intrinsic Domain Magnetization of a Ferromagnet. *Physical Review* **58**, 1098–1113 (1940).

[98] Klein, A. & Marshalek, E. R. Boson realizations of Lie algebras with applications to nuclear physics. *Review of Modern Physics* **63**, 375–558 (1991).

[99] Laussy, F. P., del Valle, E., Schrapp, M., Laucht, A. & Finley, J. J. Climbing the Jaynes-Cummings ladder by photon counting. *Journal of Nanophotonics* **6**, 061803–061803 (2012).

[100] Andreani, L. C., Panzarini, G. & Gérard, J.-M. Strong-coupling regime for quantum boxes in pillar microcavities: Theory. *Physical Review B* **60**, 13276–13279 (1999).

[101] Hechenblaikner, G., Gangl, M., Horak, P. & Ritsch, H. Cooling an atom in a weakly driven high-Q cavity. *Physical Review A* **58**, 3030–3042 (1998).

[102] Walls, D. & Milburn, G. *Quantum Optics* (Springer, 2008).

[103] Poole Jr., C. P. *Electron Spin Resonance: A Comprehensive Treatise on Experimental Techniques* (Dover Publications, 1997).

[104] Stesmans, A. & Afanas'ev, V. V. Electron spin resonance features of interface defects in thermal (100)Si/SiO2. *Journal of Applied Physics* **83**, 2449–2457 (1998).

[105] Feher, G., Fletcher, R. C. & Gere, E. A. Exchange Effects in Spin Resonance of Impurity Atoms in Silicon. *Physical Review* **100**, 1784–1786 (1955).

[106] Cullis, P. R. & Marko, J. R. Electron paramagnetic resonance properties of n-type silicon in the intermediate impurity-concentration range. *Physical Review B* **11**, 4184–4200 (1975).

[107] Morishita, H. *et al.* Linewidth of Low-Field Electrically Detected Magnetic Resonance of Phosphorus in Isotopically Controlled Silicon. *Applied Physics Express* **4**, 021302 (2011).

[108] Gordon, J. P. & Bowers, K. D. Microwave Spin Echoes from Donor Electrons in Silicon. *Physical Review Letters* **1**, 368–370 (1958).

[109] Blundell, S. *Magnetism in Condensed Matter* (Oxford University Press, England, 2001).

[110] Stesmans, A., Nouwen, B. & Afanas'ev, V. V. P_{b1} interface defect in thermal (100)Si/SiO$_2$: ^{29}Si hyperfine interaction. *Physical Review B* **58**, 15801–15809 (1998).

[111] Hoehne, F. *Electrical Detection of Hyperfine Interactions in Silicon.* Ph.D. thesis, Technische Universität München (2012).

[112] Wang, W. *et al.* Interplay between Strong Coupling and Radiative Damping of Excitons and Surface Plasmon Polaritons in Hybrid Nanostructures. *ACS Nano* **8**, 1056–1064 (2014).

[113] Müller, K. *Coherent Manipulation of Phosphorus Donor Spins in Silicon at Low Temperatures.* Master's thesis, Technische Universität München (2014).

[114] Weber, R. T. *Elexys E 580 Pulse EPR Spectrometer Users's Manual.* Bruker BioSpin Corporation (2001).

[115] Feher, G. & Gere, E. A. Electron Spin Resonance Experiments on Donors in Silicon. II. Electron Spin Relaxation Effects. *Physical Review* **114**, 1245–1256 (1959).

[116] Castner, T. G. Raman Spin-Lattice Relaxation of Shallow Donors in Silicon. *Physical Review* **130**, 58–75 (1963).

[117] Morello, A. *et al.* Single-shot readout of an electron spin in silicon. *Nature* **467**, 687–691 (2010).

[118] Bothner, D. *et al.* Magnetic hysteresis effects in superconducting coplanar microwave resonators. *Physical Review B* **86**, 014517 (2012).

[119] Bloch, F. Nuclear induction. *Physical Review* **70**, 460–474 (1946).

[120] Beige, A., Braun, D. & Knight, P. L. Driving atoms into decoherence-free states. *New Journal of Physics* **2**, 22 (2000). URL `http://stacks.iop.org/1367-2630/2/i=1/a=322`.

[121] Temnov, V. V. & Woggon, U. Superradiance and Subradiance in an Inhomogeneously Broadened Ensemble of Two-Level Systems Coupled to a Low-Q Cavity. *Physical Review Letters* **95**, 243602 (2005).

[122] Cai, J., Cohen, I., Retzker, A. & Plenio, M. B. Proposal for High-Fidelity Quantum Simulation Using a Hybrid Dressed State. *Physical Review Letters* **115**, 160504 (2015).

[123] Levitt, M. *Spin Dynamics: Basics of Nuclear Magnetic Resonance* (John Wiley & Sons, 2013).

[124] Hahn, E. L. Spin Echoes. *Physical Review* **80**, 580–594 (1950).

[125] Tyryshkin, A. M., Lyon, S. A., Astashkin, A. V. & Raitsimring, A. M. Electron spin relaxation times of phosphorus donors in silicon. *Physical Review B* **68**, 193207 (2003).

[126] Castner, T. G. Orbach Spin-Lattice Relaxation of Shallow Donors in Silicon. *Physical Review* **155**, 816–825 (1967).

[127] Mims, W. B. Electron Echo Methods in Spin Resonance Spectrometry. *Review of Scientific Instruments* **36**, 1472–1479 (1965).

[128] Hu, P. & Hartmann, S. R. Theory of spectral diffusion decay using an uncorrelated-sudden-jump model. *Physical Review B* **9**, 1–13 (1974).

[129] Zhidomirov, G. & Salikhov, K. Contribution to the Theory of Spectral Diffusion in Magnetically Diluted Solids. *Journal of Experimental and Theoretical Physics* (1969).

[130] Mims, W. B. Phase Memory in Electron Spin Echoes, Lattice Relaxation Effects in CaWO$_4$: Er, Ce, Mn. *Physical Review* **168**, 370–389 (1968).

[131] Biercuk, M. J. *et al.* Optimized dynamical decoupling in a model quantum memory. *Nature* **458**, 996–1000 (2009).

[132] Gershenzon, E. M., Semenov, I. T., Fogelson, M. S. & Chambootkin, D. P. Spin-lattice relaxation of p donors in si for different concentrations of majority and compensating impurities. *physica status solidi (b)* **69**, 679–686 (1975).

[133] Hasegawa, H. Spin-Lattice Relaxation of Shallow Donor States in Ge and Si through a Direct Phonon Process. *Physical Review* **118**, 1523–1534 (1960).

[134] Tahan, C. & Joynt, R. Relaxation of excited spin, orbital, and valley qubit states in ideal silicon quantum dots. *Physical Review B* **89**, 075302 (2014).

[135] Hsueh, Y.-L. *et al.* Spin-Lattice Relaxation Times of Single Donors and Donor Clusters in Silicon. *Physical Review Letters* **113**, 246406 (2014).

[136] Tannus, A. & Garwood, M. Adiabatic pulses. *NMR in Biomedicine* **10**, 423–434 (1997).

[137] Nielsen, N. C., Kehlet, C., Glaser, S. J. & Khaneja, N. *Optimal Control Methods in NMR Spectroscopy* (John Wiley & Sons, Ltd, 2007).

[138] Braun, M. & Glaser, S. J. Concurrently optimized cooperative pulses in robust quantum control: application to broadband Ramsey-type pulse sequence elements. *New Journal of Physics* **16**, 115002 (2014). URL `http://stacks.iop.org/1367-2630/16/i=11/a=115002`.

[139] Laucht, A. *et al.* Electrically controlling single-spin qubits in a continuous microwave field. *Science Advances* **1**, 1–5 (2015).

List of Publications

- C. W. Zollitsch, K. Mueller, D. P. Franke, S. T. B. Goennenwein, M. S. Brandt, R. Gross, H. Huebl. High cooperativity coupling between a phosphorus donor spin ensemble and a superconducting microwave resonator
  Applied Physics Letters **107**, 142105 (2015)

- H. Huebl, C. W. Zollitsch, J. Lotze, F. Hocke, M. Greifenstein, A. Marx, R. Gross, S. T. B. Goennenwein High cooperativity in Coupled Microwave Resonator Ferrimagnetic Insulator Hybrids
  Physical Review Letters **111**, 127003 (2013)

- J. Goetz, F. Deppe, M. Haeberlein, F. Wulschner, C. W. Zollitsch, S. Meier, M. Fischer, P. Eder, E. Xie, K. G. Fedorov, E. P. Menzel, A. Marx, R. Gross. Loss mechanisms in superconducting thin film microwave resonators
  Journal of Applied Physics **119**, 015304 (2016)

- F. Wulschner, J. Goetz, F. R. Koessel, E. Hoffmann, A. Baust, P. Eder, M. Fischer, M. Haeberlein, M. J. Schwarz, M. Pernpeintner, E. Xie, L. Zhong, C. W. Zollitsch, B. Peropadre, J.-J. Garcia Ripoll, E. Solano, K. Fedorov, E. P. Menzel, F. Deppe, A. Marx, R. Gross. Tunable coupling of transmission-line microwave resonators mediated by an rf SQUID
  arXiv:1508.06758

Acknowledgement

Finally, I would like to express my thanks to all people who helped and supported me during the work on my thesis at the Walther-Meißner-Institut. I sincerely thank:

Prof. Dr. Rudolf Gross, for giving me the opportunity for doing my thesis at the WMI. For his support and his insightful discussions about my thesis and general physics. For offering help even when he has so much other important things to do. For his help in getting my first Postdoc position, which opens a new chapter in my scientific career.

Dr. Hans Hübl, for a great supervision of my thesis and for showing me the ways of a physicist. His tremendous help on all the little challenges, which I encountered during the course of my thesis. For the elaborate discussions on my experimental data, which provided always new insights, allowing me to better understand the underlying physical processes and plan my next experimental steps. For his support during my work and even beyond, in finding my Postdoc position.

Prof. Dr. Martin Brandt, for his constant support during the course of my thesis. For providing me with very good and encouraging feedback, motivating me in pushing forward. For granting me access to the ESR laboratory at the WSI, which allowed me to acquire valuable data for my thesis. For offering me a boat trip on the San Antonio canals, which we still have to do.

Dr. Stephan Geprägs, for his support and his encouragement. For the many discussions on various topics, which I always enjoyed very much. For cheering me up, when my mood was clouded. I really appreciate your support during the last years.

Dr. Matthias Althammer, for being an awesome colleague and friend. For having always an open ear for me, discussing physics with me or simply having a small chat. I wish you and your young family all the best for the future.

Dr. Matthias Opel, for providing a very good atmosphere at the institute. For his commited help on various topics and his way in seeing the bright side of things.

David Franke, for being an excellent discussion partner on topics concerning silicon and donors. The several occasions where we shared our knowledge and could learn from each